Implementation of Anisotropic Diffusivity in a 2D Shallow Water Pollutant Transport Model

Auteur : Borbouse, Charlotte
Promoteur(s) : Dewals, Benjamin
Faculté : Faculté des Sciences appliquées
Diplôme : Master en ingénieur civil physicien, à finalité approfondie
Année académique : 2024-2025
URI/URL : http://hdl.handle.net/2268.2/23201

Université de Liège - Faculté des Sciences Appliquées

Implementation of Anisotropic Diffusivity in a 2D Shallow Water Pollutant Transport Model

---

Master thesis presented by
Borbouse Charlotte
in partial fulfillment of the requirements for the degree of Master of Science in Engineering Physics

---

Thesis supervisors
Professor Dewals Benjamin
University of Liège

Chakraborty Pratik
University of Liège

Jury members
Prof. Archambeau Pierre, Prof. Erpicum Sebastien, Prof. Gilet Tristan

Liège, Academic year 2024-2025

Abstract

This thesis investigates the modelling of pollutant transport in flooded urban environments using a two-dimensional shallow water advection-diffusion framework. The numerical model is based on a finite-volume discretization and incorporates both isotropic and anisotropic diffusion tensors. A particular focus is placed on distinguishing between longitudinal and transverse diffusion, and evaluating their respective influence on the simulated pollutant spreading.

The advection term is discretized using various numerical schemes, including a first-order upwind method and a second-order flux-limited scheme. Their impact on accuracy and numerical diffusion is assessed through benchmark tests involving analytical solutions. The model is then applied to replicate experimental scenarios from the M.U.R.I. platform at INRAE Lyon, using both time-averaged and fully unsteady hydrodynamic fields generated by the Wolf 2D model.

A sensitivity analysis is performed across a wide range of anisotropic diffusion coefficients. Results show that the longitudinal coefficient D_L has a predominant influence on the downstream elongation of the pollutant plume, while the transverse component D_T contributes to lateral diffusion. The spatial structure of the concentration field results from the combined effect of both coefficients, depending on the flow configuration and injection point. Although no universal relationship is observed, the anisotropy ratio D_L/D_T provides a useful metric to compare different configurations. For each test case, a ratio between 2.5 and 3.5 is typically associated with the best agreement with experimental data, reflecting the directional nature of pollutant transport in urban environments.

The study highlights the importance of both anisotropic calibration and the use of time-resolved hydrodynamics for accurately capturing pollutant dynamics in complex urban flows. It also underscores the trade-offs between numerical cost and physical realism, motivating future developments aimed at accelerating simulations and extending validation to additional configurations and injection points.

Keywords: Anisotropic diffusion, advection-diffusion, shallow water equations, pollutant transport, urban flooding, finite-volume method, numerical schemes, M.U.R.I. experiment, Wolf 2D

Acknowledgements

This thesis marks the conclusion of a rich and formative journey. I would like to take this opportunity to sincerely thank the people whose guidance, support, and presence have made this work possible.

First and foremost, I wish to express my deep gratitude to Professor Benjamin Dewals, who supervised this work with clarity, availability, and trust. His advice and constructive feedback helped steer this research in the right direction.

I owe an immense thank you to Pratik Chakraborty. He was always available to answer my questions, review my work, and help me better understand the physical and numerical aspects. I truly appreciated his time, patience, and the interest he showed in my progress.

I would like to extend my thanks to the researchers and developers behind the Wolf 2D code, which served as the hydrodynamic foundation of this work. Their commitment to open, modular, and efficient hydrodynamic modeling has greatly facilitated the coupling with advection-diffusion solvers and enabled the numerical experimentation carried out in this thesis.

A special acknowledgement goes to Benjamin Froquet and Gaël Fontaine for their respective contributions to the implementation of the isotropic advection-diffusion module. Their work provided a solid numerical base on which the present anisotropic developments could be built.

I would also like to acknowledge the team behind the M.U.R.I. experimental platform at INRAE, and particularly Clément Fagour, whose doctoral work provided the experimental datasets used for model calibration and validation. Their meticulous measurements and data availability made it possible to anchor the simulations in a realistic and experimentally observed urban flood scenario.

I would also like to thank Maxime Borbouse, a PhD student in the Aerospace and Mechanical Engineering Department, for carefully reading my thesis and helping me improve its clarity and structure. His feedback was precise and greatly appreciated. A special thanks as well to Tom Cheniaux for his precious help and for lending me his desktop computer, which allowed me to run many of the simulations that would not have been possible otherwise.

Finally, I am deeply thankful to my family and friends. Your constant support, encouragement, and presence, through the good days and the more difficult ones, have helped me stay grounded and focused. This work would not have been the same without your backing.

Contents

Chapter 1

Introduction

1.1 Motivations

Urban floods are complex hydrological phenomena that pose significant threats to infrastructure, ecosystems, and human health. In addition to their physical and economic impact, floodwaters can mobilize a wide variety of pollutants, including heavy metals, hydrocarbons, pesticides, and pathogens, which originate from roads, industrial zones, sewage networks, and built surfaces. Once in motion, these pollutants are transported through urban environments, potentially contaminating rivers, groundwater, and residential areas [Stevens et al., 2010]. Understanding and predicting the transport of such contaminants is therefore essential for effective environmental protection and risk management.

This need has become even more pressing in recent years, as the frequency and severity of flood events increase due to climate change. Long-term observational data confirm this trend: as illustrated in Figure 1.1, the number of heavy rainfall days recorded during summer in Belgium has significantly increased over the past century. This intensification of precipitation, combined with urbanization and soil sealing, has made cities particularly vulnerable to surface flooding.

In July 2021, Belgium experienced some of the most devastating floods in its history. The region of Liège was particularly affected, with significant human, material, and environmental consequences. Figure 1.2 shows the extent of the flooding in urban streets during this event. Beyond the damage caused by water itself, concerns were raised about the spread of pollutants in industrial zones and wastewater overflows, especially in densely constructed and low-lying areas [Dekenne et al., 2022]. These events highlighted the urgent need for reliable tools capable of anticipating not only water depths but also the pathways and concentrations of transported contaminants.

More recently, in May 2024, the region of Valencia in eastern Spain experienced severe flash floods following intense rainfall. These floods caused extensive damage, led to evacuations, and disrupted infrastructure. Figure 1.3 illustrates the extent of the flooding in urban streets. Similarly to the events in Belgium, concerns were again raised regarding the transport of pollutants and public health risks after such extreme events. These successive events, which occur in different parts of Europe, illustrate the increasing frequency and geographical spread of extreme floods, highlighting a wider climatic trend.

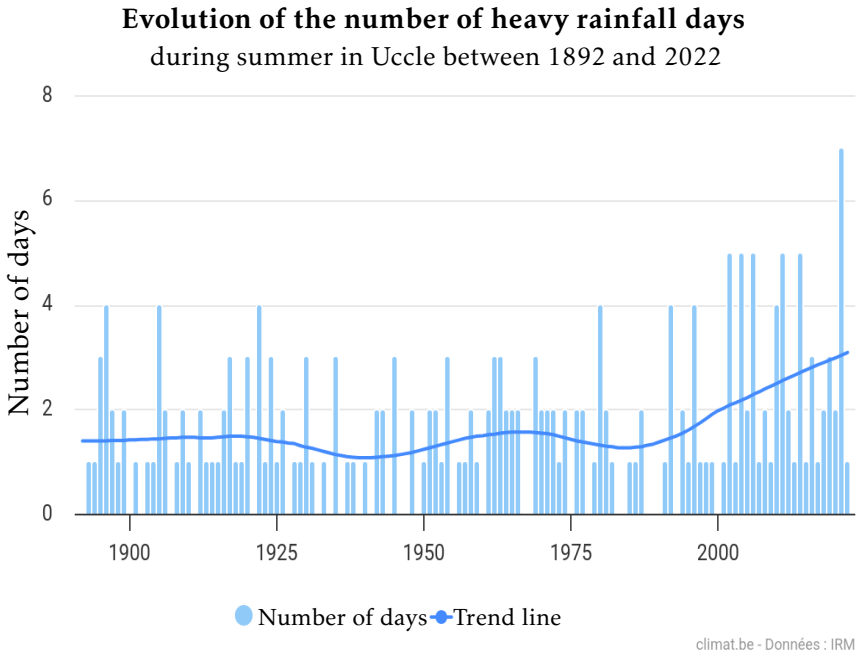

Figure 1.1: Trend in the number of heavy rainfall days during summer in Uccle from 1892 to 2022. The number of extreme rainfall days has increased significantly in recent decades. Image adapted from IRM [2022].

Figure 1.2: Urban flooding in Liège during the July 2021 flood event. This image illustrates the severity of the event and the extent of water intrusion in dense urban areas. Image from Brajkovic et al. [2025].

Numerical models are indispensable tools in this context. They provide a means to simulate complex physical processes, test different scenarios, and support decision making in both emergency situations and long-term planning. In the case of pollutant transport during floods, numerical models typically couple hydrodynamic solvers, such as the 2D shallow water equations, with advection-diffusion equations to predict how contaminants are carried by flow and spread over time. These models can inform mitigation strategies, such as locating pollution

Figure 1.3: Flash flooding in Valencia, Spain, in October 2024. The image shows the rapid inundation of urban streets, illustrating the destructive power of sudden heavy rainfall events. Image from Newsweek [2024].

barriers, designing retention areas, or planning evacuation routes. More generally, they offer a predictive framework to reduce exposure risks, protect ecosystems, and comply with environmental regulations.

However, despite their utility, existing numerical models often rely on simplified assumptions that may limit their accuracy in complex urban settings. One of the most common simplifications is the assumption of isotropic diffusion, where pollutant diffusion is considered equal in all directions. Although this assumption may be valid in some natural flows, it is generally inadequate for urban environments, where the geometry of streets, the presence of obstacles, and local flow structures create directional dependencies in mixing and transport. Experimental studies, including those conducted at INRAE (Lyon) on reduced-scale physical models of flooded urban areas, have clearly shown that pollutant plumes are frequently elongated along flow directions and that transverse mixing can be delayed [Fagour, 2025]. These observations suggest that anisotropic diffusion, where longitudinal and transverse coefficients differ, is a more appropriate representation to model pollutant transport in such environments.

Nevertheless, anisotropic diffusion remains underexplored in many operational and academic pollutant transport models. One reason is the difficulty of calibrating the longitudinal and transverse diffusion coefficients. Another challenge is the numerical implementation itself: standard discretization schemes may not correctly capture the effects of anisotropy [Morales-Hernández et al., 2019; Kim et al., 2023]. As a result, many existing studies continue to use isotropic formulations, potentially misrepresenting the extent and directionality of pollutant spreading and thus underestimating or overestimating environmental risks. Addressing this gap requires both theoretical insight and validation against experimental data, which constitutes the core motivation of the present study.

1.2 Methodology and Overview

The first part of the study consists of a literature review, which provides an overview of existing knowledge on pollutant transport during floods. This includes the main physical mechanisms involved, the influence of urban geometry on flow and mixing, and the current modelling approaches. The review covers theoretical, experimental, and numerical contributions, with a particular emphasis on the treatment of diffusion, and more specifically, the question of anisotropy in urban contexts.

The second part focuses on the theoretical formulation of the problem. A depth-averaged advection-diffusion framework is adopted to describe the transport of contaminants in shallow water flows. Special attention is given to the mathematical representation of anisotropic diffusion, where distinct longitudinal and transverse coefficients are considered, as well as potential cross-diffusion effects. The goal of this section is to provide a clear foundation for the subsequent numerical developments.

The third part is dedicated to the development of a numerical model based on the equations introduced earlier. The solver is implemented within a finite-volume framework on a structured grid, and several numerical schemes are evaluated for the discretization of advective and diffusive fluxes. Benchmark test cases are used to validate the implementation and analyse the sensitivity of the model.

The final stage of the study consists of a detailed analysis of the simulation results. Both qualitative and quantitative assessments are performed to evaluate the ability of the model to reproduce expected diffusion behaviours. In particular, the role of anisotropic diffusion is examined by comparing different scenarios and identifying the impact of directional diffusion on pollutant plume development. The simulation results are systematically compared with experimental data.

Overall, this methodology aims to offer a contribution that goes from theoretical understanding to practical application, while addressing one of the limitations of current models: the lack of rigorous integration of anisotropic diffusion in pollutant transport simulations.

Chapter 2

Literature Review

2.1 Introduction

Pollutant transport has been the subject of extensive research due to its relevance in environmental engineering, water quality management, and risk assessment. A wide range of scenarios has motivated the development of both experimental studies and numerical models to characterize the underlying processes and predict contaminant transport in complex environments.

This chapter provides an overview of the literature on pollutant transport in shallow water flows. The review is organized into three main parts: experimental investigations that provide insight into real-world transport behaviour; numerical modelling strategies based on the advection-diffusion equation; and recent advances in the representation of anisotropic diffusion. Particular attention is given to the limitations of conventional approaches and the specific challenges posed by the modelling of direction-dependent diffusion in urban environments, which motivates the development of improved simulation methods.

2.2 Experimental Studies

Experimental investigations help to understand pollutant transport under real-world flow conditions. Several laboratory and field experiments have been conducted to analyse pollutant transport in flooded urban street networks, rivers, and shallow water systems.

A contribution in this field comes from the experimental work of Mejía-Morales et al. [2023], which investigated the impact of urban block porosity on flood risk and pollutant transport. Conducted at INRAE (Lyon), these experiments focused on flow exchanges between porous urban blocks and adjacent streets during flooding events. The study demonstrated how lateral flow exchanges through openings (such as doors and gates) alter pollutant transport mechanisms, affecting both local flow velocity and dispersion patterns. These findings established an experimental framework for subsequent research on pollutant transport in urban environments.

Building on this work, Fagour [2025] extended these experimental studies by examining pollutant transport in flooded street networks. This study, also conducted at INRAE, reused and refined the urban geometry originally developed by Mejía-Morales et al. [2023], while incorporating additional variables such as pollutant injection locations and different flow regimes. The

experimental setup consisted of controlled pollutant injections in a scaled urban street network subjected to varying hydraulic conditions. The results demonstrated variability in pollutant retention and mixing patterns, emphasizing the role of street configurations and flow anisotropy in pollutant transport.

Additionally, the work of Velickovic et al. [2017] explored different formulations of pollutant transport equations based on laboratory-scale experiments in controlled hydraulic channels. Their findings provided insight into how turbulence, sediment interactions, and anisotropic flow patterns influence diffusion coefficients.

In contrast to these controlled laboratory experiments, Kim et al. [2023] conducted field investigations in natural streams to assess solute retention and storage effects. The study highlighted the influence of transient storage zones and local flow structures on pollutant retention time, showing how turbulence intensity and morphological variability affect transport efficiency in natural environments.

Collectively, these experimental studies provide valuable data for validating pollutant transport models and improving diffusion parameterizations in numerical simulations.

2.3 Numerical Modelling Approaches

The transition from experimental observations to numerical simulations is essential to develop predictive models of pollutant transport. Numerical models typically rely on solving advection-diffusion equations coupled with hydrodynamic solvers to simulate the transport of contaminants under various flow conditions.

Hydrodynamic conditions in urban floods are typically simulated using depth-averaged two-dimensional shallow water equations, which are widely used due to their computational efficiency and ability to capture flow dynamics in complex urban geometries. These models generate time-dependent velocity and water depth fields that can be coupled with advection-diffusion equations to simulate pollutant transport. Several studies have applied such approaches to urban flood scenarios, showing their relevance for modelling overland flow and transport processes [Camnasio et al., 2014; Dewals et al., 2006; Erpicum et al., 2009]. In particular, the work of Dewals et al. [2023] focused on hydrodynamic modelling using 2D shallow water equations to reproduce urban flood dynamics. While their study does not address pollutant transport directly, it provides validation of the hydrodynamic solver, which is essential for coupling with transport models.

While the modelling of advective transport is generally well established, the same cannot be said for diffusion and dispersion processes. There is no universal consensus on how to represent the spatial variability of diffusion in realistic flow conditions, especially when turbulence and complex geometries come into play. In particular, traditional isotropic diffusion models, assuming equal spreading in all directions, often fail to capture the directional nature of dispersion observed in experiments.

Further developments in numerical modelling have focused on overcoming the limitations of isotropic diffusion by incorporating anisotropic diffusion formulations. Studies such as Mignot et al. [2023] have reviewed various formulations of the 2D advection-diffusion equation, highlighting the diversity of approaches for representing the diffusion tensor. This diversity in

formulation reflects the absence of a unified theoretical framework and constitutes a first challenge for modellers.

A second, equally important, challenge lies in the calibration and validation of these formulations. While many models propose alternative expressions for anisotropic diffusion, very few provide proper comparison with experimental data. As emphasized by Mignot et al. [2023], the lack of consensus on diffusivity tensor calibration and the limited availability of benchmark datasets remain major obstacles to improving the reliability of pollutant transport models.

Figure 2.1 presents a synthetic overview of the most common diffusivity tensor formulations found in the literature. The lower panel illustrates the conceptual distinction between isotropic diffusion (equal spreading in all directions) and anisotropic diffusion. The top part summarizes eight representative types of diffusivity tensors, ranging from simple isotropic cases to rotated or empirically-derived anisotropic forms.

Overall, these numerical studies confirm the need for refined diffusion models that go beyond classical and commonplace isotropic assumptions. The integration of anisotropic diffusion tensors, as suggested by Mignot et al. [2023], provides a promising direction for improving the accuracy of pollutant transport simulations. This study builds on these advances by developing an anisotropic advection-diffusion model, which is calibrated and validated using experimental datasets.

2.4 Challenges and Limitations of Existing Models

Despite some advances in the modelling of pollutant transport in shallow water and urban environments, several persistent challenges limit the accuracy and generalizability of current approaches. A primary issue lies in the widespread assumption of isotropic diffusion, which implies uniform spreading of pollutants in all directions. However, experimental evidence from Fagour [2025] has demonstrated that real-world transport is anisotropic, shaped by flow direction, turbulence structures, and obstacle-induced heterogeneity.

A second limitation is the lack of standardization in the selection and calibration of diffusion tensors. As highlighted by Mignot et al. [2023], the literature contains at least seven mathematical formulations of the depth-averaged advection-diffusion equation and eight distinct types of diffusivity tensor parameterizations. These include scalar (isotropic), axis-aligned, rotated, and empirically derived tensors. However, few studies provide rigorous validation of these formulations against experimental data. Reported values of longitudinal and transverse diffusion coefficients vary by up to three orders of magnitude between studies.

These concerns are explained in earlier work such as Pathirana et al. [2011], where diffusion coefficients were assumed rather than calibrated, undermining the predictive accuracy of the models. Similarly, Morales-Hernández et al. [2019] demonstrated that calibration based on local flow shear and anisotropic considerations yields more realistic concentration fields, while uncalibrated models tend to over or under diffuse pollutants. Recent comparative studies further reinforce this view. Fang et al. [2022] showed that simulations using anisotropic diffusion better matched observed transport patterns than those using isotropic diffusion.

Moreover, the need for robust model validation is not consistently addressed. As noted by Mignot et al. [2023], proper model development requires both calibration on controlled data and validation on independent datasets. In practice, many studies skip one or both steps. Fontaine [2023] addressed this gap by calibrating diffusion parameters using data from Fagour [2025], identifying optimal diffusivity values that minimized error in simulated concentration fields. Without such calibration, numerical simulations can produce outputs that deviate significantly from observed pollutant distributions.

Finally, numerical discretization itself poses challenges. Low order schemes such as first-order upwind are prone to excessive numerical diffusion, which can mask or distort physically meaningful concentration gradients. Morales-Hernández et al. [2019] and others have shown that high-resolution schemes or flux-limited methods are necessary to preserve sharp pollutant fronts and maintain mass conservation, especially when modelling anisotropic diffusion.

Taken together, these findings highlight the necessity for replacing isotropic assumptions with physically informed anisotropic diffusion formulations, calibrating diffusion coefficients against experimental datasets rather than assuming generic values, applying structured calibration-validation workflows to ensure model robustness, employing numerical schemes that limit artificial diffusion and preserve key transport features.

2.5 Research Objectives

In response to the challenges outlined above, this study seeks to improve the numerical modelling of pollutant transport by integrating an anisotropic diffusion model within a validated hydrodynamic framework. This approach is guided by the recommendations of Mignot et al. [2023], who calls for a systematic calibration and validation methodology when applying diffusivity tensors in shallow water models.

By leveraging the controlled experimental data from Fagour [2025], this research provides a basis for the calibration of longitudinal and transverse diffusion coefficients. This study specifically aims to:

- Develop and implement a numerical framework capable of representing anisotropic diffusion, allowing for independent control of directional diffusivities.
- Evaluate the performance of different numerical advection schemes, with particular attention to their ability to limit numerical diffusion.
- Compare numerical predictions with experimental measurements from controlled laboratory setups, applying a calibration-validation approach to ensure model reliability.
- Explore the interactions between hydrodynamics, diffusion anisotropy, and numerical discretization, and assess their combined impact on pollutant transport under flood-like conditions.

Number of coefficients		Dimensional diffusivity coefficient(s) (m^2/s)	Nondimensional coefficient(s) (–) describing the ratio of diffusivity to hu_* (Elder approach)	Schmidt number (–)
1	①	$\mathbf{D} = D\,\mathbf{I}$	②[a,b] $\mathbf{D} = k\,\mathbf{R}^T \begin{pmatrix} hu_{*L} & 0 \\ 0 & hu_{*T} \end{pmatrix} \mathbf{R}$	③ $\mathbf{D} = \nu_T / \sigma_c \mathbf{I}$
2	④	$\mathbf{D} = \begin{pmatrix} D_x & 0 \\ 0 & D_y \end{pmatrix}$		
2	⑤[a]	$\mathbf{D} = \mathbf{R}^T \begin{pmatrix} D_L & 0 \\ 0 & D_T \end{pmatrix} \mathbf{R}$	⑥[a] $\mathbf{D} = \mathbf{R}^T \begin{pmatrix} k_L hu_* & 0 \\ 0 & k_T hu_* \end{pmatrix} \mathbf{R}$	
3–4[c]	⑦[a]	$\mathbf{D} = \mathbf{R}^T \begin{pmatrix} D_L & D_{LT} \\ D_{TL} & D_T \end{pmatrix} \mathbf{R}$		
3–4[d]	⑧	$\mathbf{D} = \begin{pmatrix} D_x & D_{xy} \\ D_{yx} & D_y \end{pmatrix}$		

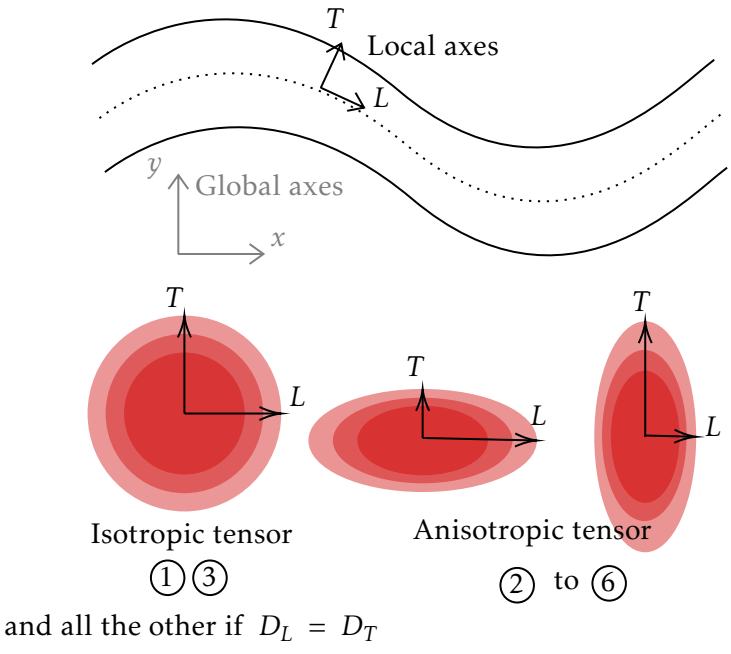

Figure 2.1: Top: Classification of eight representative diffusion tensor configurations. This table is adapted graphically from Mignot et al. [2023] and Fagour [2025]. **Bottom:** Conceptual comparison between isotropic (left) and anisotropic (right) diffusion. Isotropic diffusion assumes $D_L = D_T$, resulting in uniform radial spreading. Anisotropic diffusion allows independent control of longitudinal and transverse diffusion, leading to elongation aligned with the main flow direction.

Chapter 3

Theoretical Background

This chapter presents the theoretical foundations underlying the numerical modelling of hydrodynamics and pollutant transport in shallow water flows. The first part of the chapter outlines the governing equations of two-dimensional shallow water flows, derived from depth-averaging the Navier-Stokes equations. The second part is dedicated to the modelling of pollutant transport using the advection-diffusion equation in a depth-averaged framework. The derivation and interpretation of the different terms in the equation are presented. The section also discusses the treatment of anisotropic diffusion through the use of a tensorial representation and the transformation of the coordinate system to align with the principal flow direction.

Together, these theoretical elements form the basis of the numerical implementation described in Chapter 5, and provide the necessary framework to interpret the results of both idealized test cases and real experimental validations.

3.1 Hydrodynamic Modelling Using 2D Shallow Water Equations

3.1.1 Governing Equations

The hydrodynamics of the system are governed by the two-dimensional shallow water equations (SWE), expressed in conservative form as follows [Dewals et al., 2023]

$$\frac{\partial h}{\partial t} + \frac{\partial (hu)}{\partial x} + \frac{\partial (hv)}{\partial y} = 0, \tag{3.1}$$

$$\frac{\partial (hu)}{\partial t} + \frac{\partial}{\partial x}\left(hu^2 + \frac{1}{2}gh^2\right) + \frac{\partial (huv)}{\partial y} = \frac{\tau_{bx}}{\rho} + \frac{1}{\rho}\left(\frac{\partial h\tau_{xx}}{\partial x} + \frac{\partial h\tau_{xy}}{\partial y}\right), \tag{3.2}$$

$$\frac{\partial (hv)}{\partial t} + \frac{\partial (huv)}{\partial x} + \frac{\partial}{\partial y}\left(hv^2 + \frac{1}{2}gh^2\right) = \frac{\tau_{by}}{\rho} + \frac{1}{\rho}\left(\frac{\partial h\tau_{xy}}{\partial x} + \frac{\partial h\tau_{yy}}{\partial y}\right), \tag{3.3}$$

where h is the water depth, u and v are the depth-averaged velocities in the x and y directions, respectively, g is the gravitational acceleration, τ_{xx}, τ_{yy}, and τ_{xy} are the depth-averaged turbulent stresses comprising both the Reynolds and molecular stresses [Erpicum et al., 2009], and τ_{bx} and τ_{by} are the bed shear stresses.

The bed shear stresses are computed using the Darcy-Weisbach formulation [Dewals et al., 2023]

$$\frac{\tau_{bx}}{\rho} = -f\frac{u\sqrt{u^2+v^2}}{8}, \tag{3.4}$$

$$\frac{\tau_{by}}{\rho} = -f\frac{v\sqrt{u^2+v^2}}{8}, \tag{3.5}$$

where f is the Darcy-Weisbach friction coefficient, estimated using the Colebrook-White formula

$$\frac{1}{\sqrt{f}} = -2\log_{10}\left(\frac{k_s}{14.8h} + \frac{2.51}{Re\sqrt{f}}\right), \tag{3.6}$$

where k_s is the roughness height and Re is the Reynolds number, given by

$$Re = \frac{4h\sqrt{u^2+v^2}}{\nu}, \tag{3.7}$$

with ν being the kinematic viscosity of water.

The turbulence closure models vary between numerical approaches. The Elder model approximates eddy viscosity as [Mejía-Morales et al., 2020]

$$\nu_t = \lambda h u_*, \tag{3.8}$$

where u_* is the friction velocity, and λ is an empirical parameter.

In Wolf 2D, the depth-averaged $k-\varepsilon$ model is used for turbulence closure [Erpicum et al., 2009; Camnasio et al., 2014; Dewals et al., 2023] where k is the turbulent kinetic energy, and ε is the turbulent dissipation rate.

3.1.2 Boundary and Initial Conditions

The computational domain involves three main types of boundaries: sidewalls, inlets, and outlets. Each type requires specific treatment to ensure realistic hydrodynamic conditions [Dewals et al., 2023]:

- **Sidewalls:** The normal component of the specific discharge is set to zero to impose no-flow conditions.
- **Inlets:** The specific discharge in the streamwise direction is prescribed based on measured inflows, while the normal component is set to zero.
- **Outlets:** The outflow discharge is computed based on a weir formulation [Dewals et al., 2023]

  $$Q_0 = LC_D\sqrt{\frac{2g(h-w)^3}{3}}, \tag{3.9}$$

  where L is the weir length, C_D is the discharge coefficient, and w is the weir height.

The initial conditions are defined such that the water depth is set to a value close to experimental measurements [Dewals et al., 2023]. The initial flow velocities are either taken from a previously converged steady-state solution or simply prescribed as zero to represent a calm water start. In Dewals et al. [2023], the authors opted for the latter approach, assuming the flow is initially at rest.

3.2 Advection-Diffusion Equation for Pollutant Transport

3.2.1 Governing Equations

The depth-averaged advection-diffusion equation governs the transport of a solute in shallow water flows. It is derived by integrating the three-dimensional advection-diffusion equation over the water depth [Mignot et al., 2023]

$$\frac{\partial}{\partial t}(hC) + \nabla \cdot (h\mathbf{U}C) + \underbrace{\nabla \cdot [h\langle(\mathbf{u}-\mathbf{U})(c-C)\rangle]}_{T_3} + \underbrace{\nabla \cdot (-h\varepsilon_m\langle\nabla c\rangle)}_{T_1} + \underbrace{\nabla \cdot (h\langle-\mathbf{D}_t\nabla c\rangle)}_{T_2} = S, \tag{3.10}$$

where:

- h is the water depth,
- C is the depth-averaged pollutant concentration,
- $\mathbf{U} = (U, V)^T$ is the depth-averaged velocity vector in the horizontal x-y plane,
- $\mathbf{u} = (u, v)^T$ and c represent the local velocity and pollutant concentration in the horizontal x-y plane,
- ε_m is the molecular diffusivity coefficient [m^2/s],
- $\mathbf{D}_t$ is the turbulent diffusivity tensor [m^2/s],
- S is the depth-integrated source or sink term,
- $\langle\cdot\rangle$ denotes a depth-averaged quantity.

The last three terms in Equation (3.10) represent three key processes responsible for pollutant mixing:

1. Molecular diffusion (T_1 term),
2. Turbulent diffusion (T_2 term),
3. Dispersion caused by vertical non-uniformities in flow velocity and concentration, including velocity shear and secondary currents (T_3 term).

Resorting to a closure assumption similar to Boussinesq's approach in Reynolds-averaged turbulence models, these terms are commonly grouped under a single term, leading to the depth-averaged advection-diffusion equation in conservative form [Mignot et al., 2023]

$$\frac{\partial}{\partial t}(hC) + \nabla \cdot (h\mathbf{U}C - h\mathbf{D}\nabla C) = S, \tag{3.11}$$

where **D** is the diffusivity tensor, a (2×2) matrix that accounts for anisotropic diffusion effects, given by

$$\mathbf{D} = \begin{bmatrix} D_{xx} & D_{xy} \\ D_{yx} & D_{yy} \end{bmatrix}. \tag{3.12}$$

Expanding Equation (3.11) in full form gives

$$\frac{\partial}{\partial t}(hC) + \frac{\partial}{\partial x}(hUC) + \frac{\partial}{\partial y}(hVC) = \frac{\partial}{\partial x}\left[h\left(D_{xx}\frac{\partial C}{\partial x} + D_{xy}\frac{\partial C}{\partial y}\right)\right] + \frac{\partial}{\partial y}\left[h\left(D_{yx}\frac{\partial C}{\partial x} + D_{yy}\frac{\partial C}{\partial y}\right)\right] + S. \tag{3.13}$$

The terms D_{xx} and D_{yy} correspond to gradient-diffusion terms, also known as "Fickian turbulent diffusion" [Fischer et al., 1979], whereas D_{xy} and D_{yx} represent cross-dispersion terms that account for direction-dependent mixing effects [Lee & Kim, 2012].

This equation is conservative since it is directly derived from mass conservation principles, making it suitable for numerical resolution using shock-capturing schemes. However, determining the appropriate values of the diffusivity tensor **D** in real-world applications remains a challenge due to the complexity of turbulence and dispersion mechanisms [Mignot et al., 2023].

3.2.2 Change of Reference Frame

In order to better represent diffusion in the principal directions of flow, the advection-diffusion equation can be rewritten in a local coordinate system (s, n) aligned with the main flow direction (as mentioned by Mignot et al. [2023] and represented in Figure 2.1). Here, s represents the streamwise (longitudinal) direction and n the transverse direction. The diffusion tensor in these coordinates is given by

$$\mathbf{D}_{s,n} = \begin{bmatrix} D_L & 0 \\ 0 & D_T \end{bmatrix}, \tag{3.14}$$

where:

- D_L is the longitudinal diffusion coefficient,
- D_T is the transverse diffusion coefficient.

The transformation from local (s, n) coordinates to global (x, y) coordinates is performed using a rotation matrix **R** such that

$$\mathbf{D}_{x,y} = \mathbf{R}^{-1}\mathbf{D}_{s,n}\mathbf{R}, \tag{3.15}$$

where

$$\mathbf{R} = \begin{bmatrix} \cos\theta & -\sin\theta \\ \sin\theta & \cos\theta \end{bmatrix}, \tag{3.16}$$

with θ being the local flow direction. This transformation aligns the diffusion tensor with the main flow direction, simplifying numerical implementations and improving accuracy in anisotropic environments [Cheng, 1984; Alavian, 1986].

Chapter 4

Experimental Environment

This chapter presents the physical experimental setup and measurement techniques used to investigate solute transport mechanisms within a controlled urban flood model. The experimental campaign was carried out at INRAE (Lyon) using the M.U.R.I. platform, a large-scale physical model, replicating urban street geometries under scaled hydraulic conditions.

The main objectives of the experiments were to characterize flow patterns, assess pollutant retention and transport, and provide benchmark data for validating numerical simulations. Specific attention was given to the influence of urban block porosity, pollutant injection location, and hydrodynamic conditions on solute transport. The results obtained from these controlled experiments form the basis for evaluating the accuracy and robustness of numerical advection-diffusion models, particularly in complex geometries representative of real-world flooding scenarios.

This chapter describes the experimental setup, including the physical layout and boundary conditions. Then, it details the instrumentation and measurement techniques employed to quantify water depth, flow velocities, and pollutant concentration fields. Subsequent sections present the pollutant injection strategies and provide an overview of the accessible experimental datasets used for model validation.

4.1 Experimental Setup

The experimental setup used in this study is based on the large-scale physical model M.U.R.I. ("Modèle Urbain pour l'étude du Risque d'Inondation"), developed at INRAE, Villeurbanne, France. This model, shown in Figure 4.1, is designed to reproduce pollutant transport in an idealized urban street network under controlled hydraulic conditions. The experiments were conducted to evaluate solute transport mechanisms in flooded urban environments, providing benchmark data for validating numerical models.

The platform consists of a network of intersecting streets representing an urban district at a reduced scale. It is a tilting platform measuring 5.4 [m] in length and 3.8 [m] in width, with a horizontal scaling factor of 1:50 and a vertical scaling factor of 1:10, both defined with respect to real-world urban geometries. The setup allows control over water depth, flow velocity, and pollutant injection conditions, enabling a comprehensive analysis of pollutant transport under various flooding scenarios.

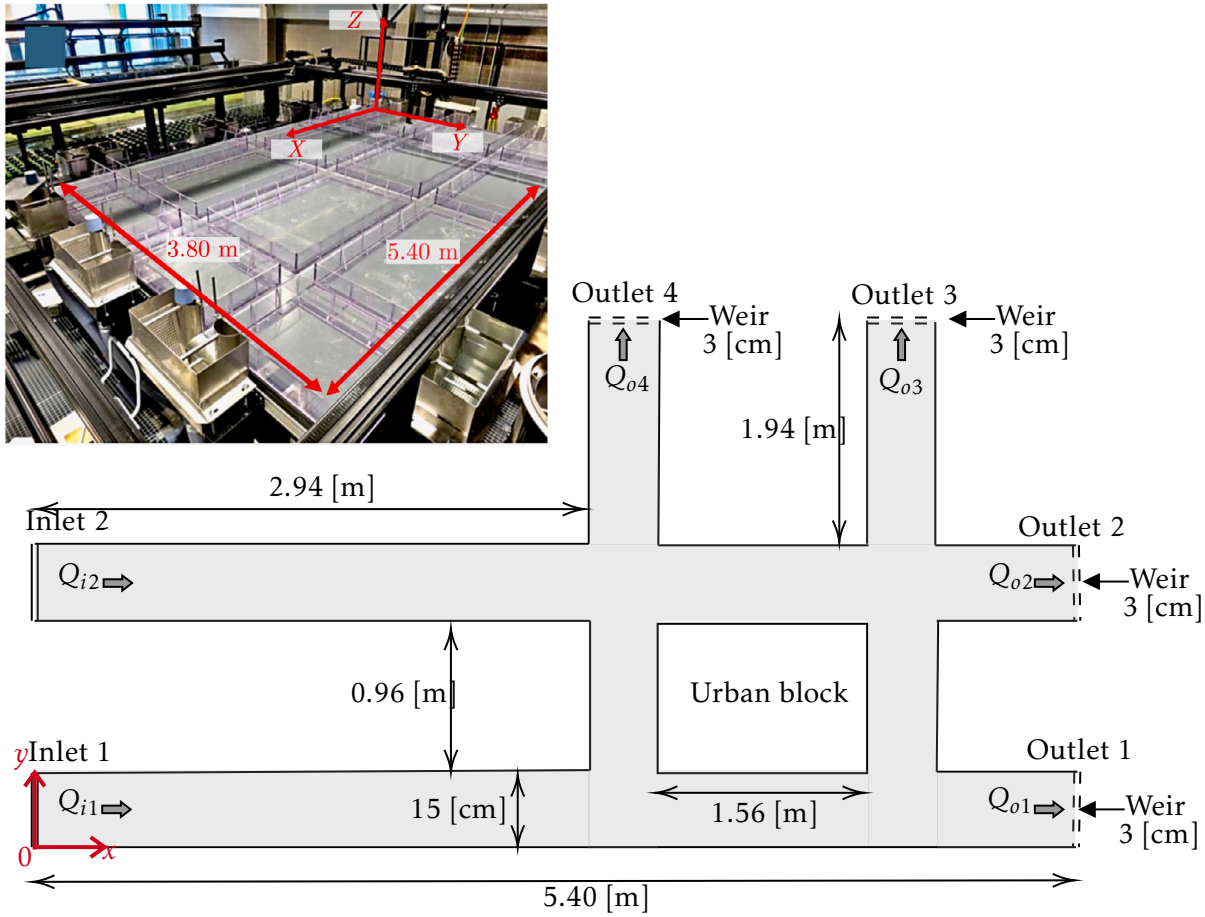

Figure 4.1: Experimental setup of the M.U.R.I. platform used at INRAE for studying pollutant transport in flooded urban environments. The setup consists of a physical model representing an urban district at reduced scale (5.40 [m] × 3.80 [m]), with controlled inflows (Inlet 1 and Inlet 2) and four outlets regulated by weirs. This setup serves as the benchmark for numerical model validation. Representation of the set-up inspired by Fagour [2024].

The experimental configuration includes a simplified flooded street network with intersections and urban blocks, designed to study the influence of street geometry and flow conditions on pollutant transport. Water is introduced into the network through controlled inlet discharges, while outflow conditions are regulated using adjustable tail weirs. The pollutant injection system ensures control locations, allowing for the study of retention and transport dynamics in various flow regimes.

The experimental study also considers the influence of urban block porosity on pollutant transport, simulating real-world urban flood conditions. As shown in Figure 4.2, the experimental setup includes a porous urban block with controlled openings, allowing for water and solute exchange between the inner block and adjacent streets. The urban block is positioned at the intersection of the main flow paths, with multiple configurations of openings to analyse pollutant retention and transport effects:

- Configuration **C0**: The block has **no opening**.
- Configuration **C1**: The block has **two openings**, allowing for minimal exchange with the surrounding flow.

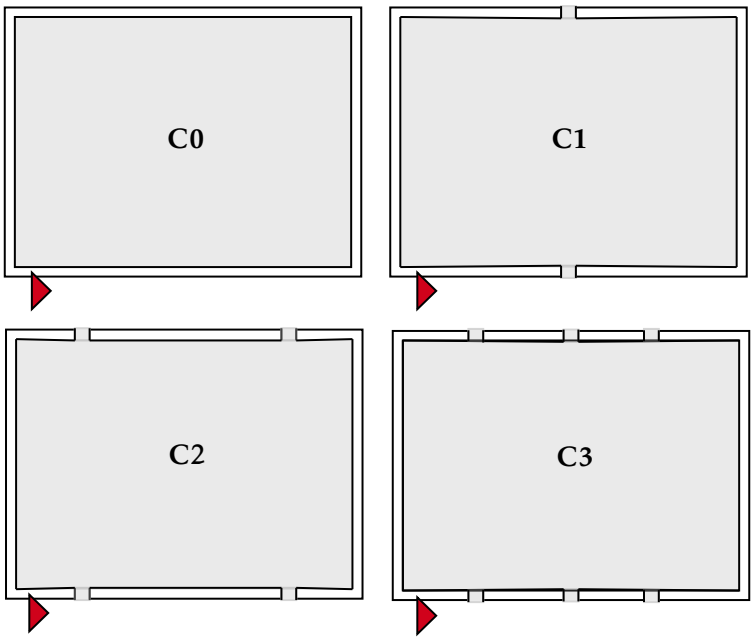

Figure 4.2: Configurations of the studied urban blocks and number of openings. (**C0**) No opening, (**C1**) Two openings, (**C2**) Four openings, (**C3**) Six openings. The red triangles indicate the direction of pollutant release.

- Configuration **C2**: The block has **four openings**, increasing connectivity and potential pollutant dilution.
- Configuration **C3**: The block has **six openings**, maximizing exchange and reducing retention effects.

The pollutant is injected at a fixed point in the right street, at coordinates $X = 3.28$ [m], $Y = 0.14$ [m]. The red markers in Figure 4.2 indicate the injection point and the direction of pollutant release. The injection is designed to simulate localized pollutant spills occurring in real-world urban flooding scenarios.

By varying the number of openings in the urban block, the study investigates the role of block porosity on pollutant transport and retention. Results from this setup will be used to compare experimental findings with numerical simulations, helping to refine diffusion parameterizations in complex urban environments.

4.2 Measurement Techniques

Several measurement techniques were employed to characterize flow hydrodynamics and pollutant transport. Water depth was measured using ultrasonic distance sensors (BAUMER UNDK 20I6914/S35A) with a precision of 0.3 [mm]. These sensors were mounted on a mechanical gantry system, enabling precise water level measurements across the experimental domain.

Flow velocities were captured using acoustic Doppler velocimetry (ADV) and large-scale particle image velocimetry (LSPIV). The ADV system provided high-resolution measurements

of three-dimensional velocity components. The LSPIV technique was used to track surface velocity fields by analysing the motion of floating tracers, with image processing performed using the Fudaa-LSPIV software [Le Coz et al., 2014] developed by EDF and INRAE.

Pollutant concentrations were measured using two complementary techniques: conductimetry and colorimetry. Conductivity sensors (Endress Hauser CLS82D) recorded local solute concentrations at multiple locations within the urban network. In addition, a colorimetric analysis was performed using a high-resolution imaging system, allowing for a spatially resolved estimation of the pollutant distribution.

4.3 Pollutant Injection

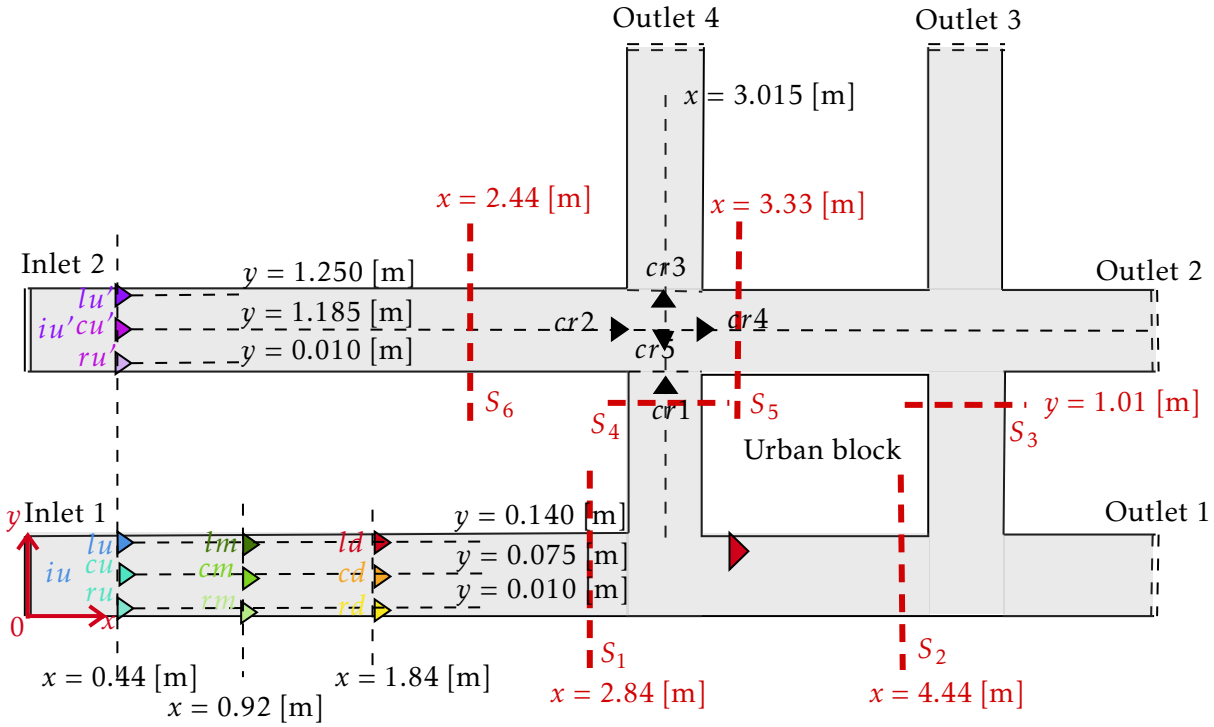

Figure 4.3: Schematic representation of pollutant injection locations within the experimental urban flood network. The injection points are categorized into upstream, midstream, and downstream locations in both the Left and Right Streets, with additional injection sites at key intersections (*cr1* - *cr5*). The triangles indicate the direction of pollutant release relative to the flow. The coordinate system is referenced to the global domain (x, y). This diagram is inspired by Fagour [2025].

The pollutant was introduced into the experimental setup using a controlled injection system. The following injection configurations were tested:

- A localized injection at a single point, simulating a spill in a flooded street.
- A homogeneous release across the water column to investigate vertical mixing effects.
- A time-limited injection scenario to analyse pollutant over time.

The experimental setup includes nineteen pollutant injection points distributed across the flooded urban street network as shown in Figure 4.3. These locations are categorized as follows, based on their longitudinal x and transverse y positioning [Fagour, 2025]:

- **Right street injections**:
  - **Upstream injections** (*iu*, *lu*, *cu*, *ru*): located near the entrance of the Right Street.
  - **Middle injections** (*lm*, *cm*, *rm*): placed further along the Right street, at an intermediate position.
  - **Downstream injections** (*ld*, *cd*, *rd*): positioned further downstream in the Right Street, before reaching the main intersection.
- **Left Street injections** (*iu'*, *lu'*, *cu'*, *ru'*): located near the entrance of the Left Street.
- **Intersection injections** (*cr1*, *cr2*, *cr3*, *cr4*, *cr5*): placed at different locations within the central intersection, where flow interactions and pollutant mixing are expected to be significant.

Each pollutant injection is pointwise and vertically uniform along the water depth, ensuring homogeneous pollutant release across the water column. The injection system used a dye tracer with a known concentration, allowing precise monitoring of pollutant transport. The effect of injection location and timing on pollutant transport was analysed using concentration measurements at various monitoring sections within the network. The red dashed lines in Figure 4.3 denote the monitoring sections S_1 to S_6, which serve as reference locations for comparing pollutant transport patterns.

4.4 Accessible Experimental Data for Urban Blocks

This section presents the experimental data collected by Fagour [2024] regarding pollutant transport in flooded urban blocks. The experimental setup was designed to investigate pollutant retention and transport under controlled flow conditions:

- **Flow Inlet Conditions**:
  - Inlet 1: $Q_{i1} = 4.5$ [L/s].
  - Inlet 2: $Q_{i2} = 2.0$ [L/s].
- **Pollutant Injection**:
  - A uniform release was ensured along the water column.
  - The injected pollutant was a red dye with a concentration of $C_{\text{rejet}} = 0.625$ [g/L].
  - The injection flow rate was $Q_{\text{rejet}} = 35.5$ [L/h].
- **Measurement Duration**:
  - Two injection scenarios were considered:
    - *Long-duration injection*: $t_{\text{rejet}} \geq 2500$ [s], ensuring pollutant accumulation and reaching a steady-state concentration.
    - *Limited-duration injection*: injection was stopped before reaching steady state, allowing for an analysis of pollutant depletion over time.

The experimental study focused on several key parameters:

- **Hydrodynamics**:
  - Time-averaged velocity fields at various sections.
  - Water depth measurements at multiple locations.
  - Flow exchange dynamics between urban streets and the porous block.
- **Pollutant Transport**:
  - Pollutant concentration measurements at different locations inside the urban block and at street outlets.
  - Analysis of pollutant retention and mixing efficiency at various sections.

In summary, the experimental environment provides a robust and well-documented framework for investigating solute transport under realistic urban flooding conditions. The carefully designed measurement protocols, pollutant injection strategies, and multiple urban block configurations offer a comprehensive dataset. These experimental results serve as a reference for validating the numerical models developed in this study, particularly in assessing their ability to reproduce pollutant retention, transport, and mass exchange in complex urban geometries.

Chapter 5

Numerical Environment

5.1 Introduction

This chapter presents the numerical framework used to solve the governing equations describing flow hydrodynamics and pollutant transport. The focus is on the discretization of the 2D shallow water equations (SWE) and the advection-diffusion equation using Finite Volume Method (FVM) for spatial discretization and Explicit Euler scheme for time integration.

The hydrodynamic flow fields are provided by the Wolf 2D model [Erpicum et al., 2009], which serves as input for the pollutant transport simulation. The velocity and water depth fields are computed by solving the 2D shallow water equations, detailed in Section 3.1, using a FVM with a second-order type scheme for flux calculations and an explicit time-stepping approach [Dewals et al., 2023]. The numerical methodology used in Wolf 2D, including the discretization of the hydrodynamic equations and the treatment of boundary conditions, is detailed in Erpicum et al. [2009]. The advection-diffusion equation is then solved on a Cartesian grid that follows the same discretization strategy as the shallow water equations to ensure consistency between the hydrodynamic and pollutant transport models.

5.2 Spatial Discretization with Finite Volume Method

The Finite Volume Method (FVM) is employed for spatial discretization to ensure consistency between the input hydrodynamic results and the advection-diffusion equations, maintaining coherence in mass, momentum, and pollutant concentration conservation.

5.2.1 Discretized Computational Domain

The computational domain is divided into a structured Cartesian grid consisting of control volumes (cells) indexed by (i, j). Each cell has dimensions $(\Delta x \times \Delta y)$ with $\Delta x = \Delta y$, and variables are stored at cell centers, while fluxes are computed at cell interfaces. A schematic representation of the discretized domain is shown in Figure 5.1.

Applying the FVM [Nakayama, 2018] to a control volume V centered at (i, j), Equation (3.13) is integrated

$$\frac{\partial}{\partial t}\int_V (hC)dV + \int_V \nabla\cdot(h\mathbf{U}C)dV - \int_V \nabla\cdot(h\mathbf{D}\nabla C)dV = \int_V S dV. \tag{5.1}$$

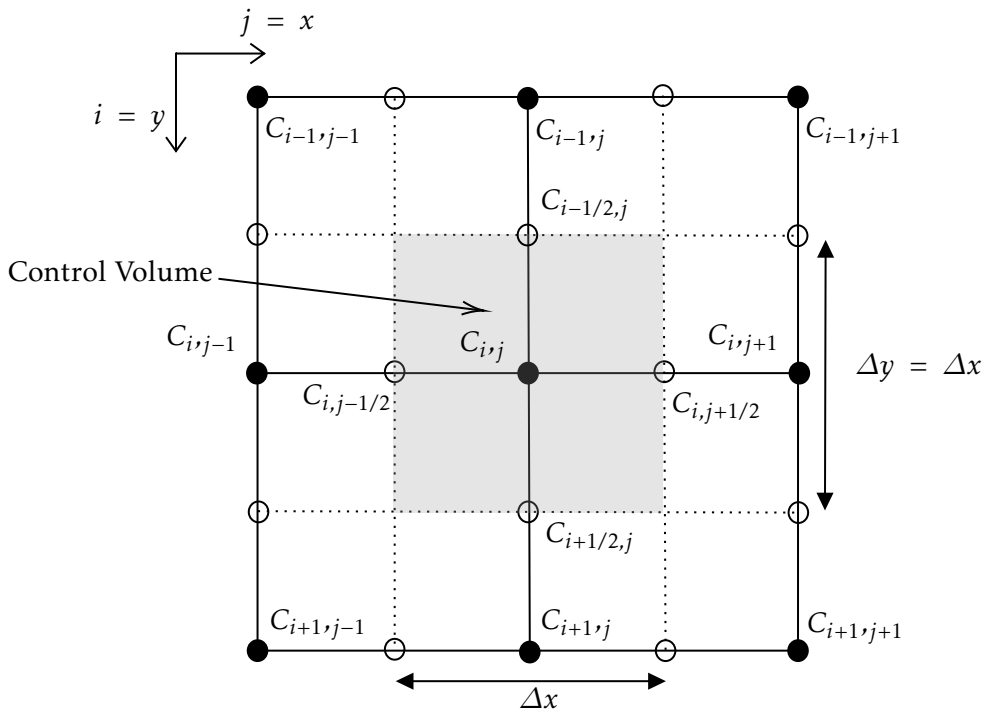

Figure 5.1: Illustration of the discretized computational domain with control volumes and flux locations, adapted from Nakayama [2018].

Using the divergence theorem (Gauss) [Kalinski, 2018], some volume integrals are converted into surface integrals

$$\int_V \frac{\partial}{\partial t}(hC)dV + \oint_S (h\mathbf{U}C - h\mathbf{D}\nabla C)\cdot d\mathbf{S} = \int_V S\,dV. \tag{5.2}$$

Approximating over the control volume $V = \Delta x \times \Delta y$, it gives

$$\begin{aligned}
&\frac{\partial}{\partial t}(hC)_{i,j}\Delta x\Delta y + \Delta y\left[(hUC)_{i,j+1/2} - (hUC)_{i,j-1/2}\right] + \Delta x\left[(hVC)_{i+1/2,j} - (hVC)_{i-1/2,j}\right] \\
&\quad - \Delta y\left[\left(hD_{xx}\frac{\partial C}{\partial x}\right)_{i,j+1/2} - \left(hD_{xx}\frac{\partial C}{\partial x}\right)_{i,j-1/2}\right] - \Delta x\left[\left(hD_{yy}\frac{\partial C}{\partial y}\right)_{i+1/2,j} - \left(hD_{yy}\frac{\partial C}{\partial y}\right)_{i-1/2,j}\right] \\
&\quad - \Delta y\left[\left(hD_{xy}\frac{\partial C}{\partial y}\right)_{i,j+1/2} - \left(hD_{xy}\frac{\partial C}{\partial y}\right)_{i,j-1/2}\right] - \Delta x\left[\left(hD_{yx}\frac{\partial C}{\partial x}\right)_{i+1/2,j} - \left(hD_{yx}\frac{\partial C}{\partial x}\right)_{i-1/2,j}\right] \\
&\quad = S_{i,j}\Delta x\Delta y.
\end{aligned}$$

5.2.2 Discretization of Advective Terms

In this work, several discretization schemes are implemented and compared, ranging from the classical first-order upwind scheme to more advanced second-order methods. Each scheme offers a balance between numerical diffusion, accuracy, and stability. In addition, the fluxes are evaluated at the cell interfaces using various finite volume approximations described in Ferziger & Perić [2002].

First-Order Upwind Scheme

The upwind scheme uses the value from the upstream cell as detailed in Ferziger & Perić [2002]. The two terms for advective part in $x-$direction are approximated as

$$(hUC)_{i,j+1/2} \approx \begin{cases} (hUC)_{i,j} & \text{if } U \geq 0, \\ (hUC)_{i,j+1} & \text{if } U < 0, \end{cases} \tag{5.3}$$

$$(hUC)_{i,j-1/2} \approx \begin{cases} (hUC)_{i,j-1} & \text{if } U \geq 0, \\ (hUC)_{i,j} & \text{if } U < 0, \end{cases} \tag{5.4}$$

and give

$$(hUC)_{i,j+1/2} - (hUC)_{i,j-1/2} \approx \begin{cases} (hUC)_{i,j} - (hUC)_{i,j-1} & \text{if } U \geq 0, \\ (hUC)_{i,j+1} - (hUC)_{i,j} & \text{if } U < 0. \end{cases} \tag{5.5}$$

The two terms for advective part in $y-$direction are approximated as

$$(hVC)_{i+1/2,j} \approx \begin{cases} (hVC)_{i,j} & \text{if } V \geq 0, \\ (hVC)_{i+1,j} & \text{if } V < 0, \end{cases} \tag{5.6}$$

$$(hVC)_{i-1/2,j} \approx \begin{cases} (hVC)_{i-1,j} & \text{if } V \geq 0, \\ (hVC)_{i,j} & \text{if } V < 0, \end{cases} \tag{5.7}$$

and give

$$(hVC)_{i+1/2,j} - (hVC)_{i-1/2,j} \approx \begin{cases} (hVC)_{i,j} - (hUC)_{i-1,j} & \text{if } V \geq 0, \\ (hVC)_{i+1,j} - (hVC)_{i,j} & \text{if } V < 0. \end{cases} \tag{5.8}$$

This scheme is stable and robust but introduces numerical diffusion.

Second-Order Upwind Scheme

A second-order upwind scheme can be used. This method uses a biased stencil depending on the sign of the velocity, relying on two upstream cells to approximate the quantity hC at the interface. This version may thus generate non-physical oscillations in non-smooth regions as detailed in Ferziger & Perić [2002] and CFD Direct [2025].

In the x-direction it gives

$$(hUC)_{i,j+1/2} = \begin{cases} \frac{3}{2}(hUC)_{i,j} - \frac{1}{2}(hUC)_{i,j-1} & \text{if } U \geq 0, \\ \frac{3}{2}(hUC)_{i,j+1} - \frac{1}{2}(hUC)_{i,j+2} & \text{if } U < 0, \end{cases} \tag{5.9}$$

and similarly for the interface at $j - 1/2$

$$(hUC)_{i,j-1/2} = \begin{cases} \frac{3}{2}(hUC)_{i,j-1} - \frac{1}{2}(hUC)_{i,j-2} & \text{if } U \geq 0, \\ \frac{3}{2}(hUC)_{i,j} - \frac{1}{2}(hUC)_{i,j+1} & \text{if } U < 0. \end{cases} \tag{5.10}$$

A similar procedure is used for the y-direction. The interface values are

$$(hVC)_{i+1/2,j} = \begin{cases} \frac{3}{2}(hVC)_{i,j} - \frac{1}{2}(hVC)_{i-1,j} & \text{if } V \geq 0, \\ \frac{3}{2}(hVC)_{i+1,j} - \frac{1}{2}(hVC)_{i+2,j} & \text{if } V < 0, \end{cases} \tag{5.11}$$

$$(hVC)_{i-1/2,j} = \begin{cases} \frac{3}{2}(hVC)_{i-1,j} - \frac{1}{2}(hVC)_{i-2,j} & \text{if } V \geq 0, \\ \frac{3}{2}(hVC)_{i,j} - \frac{1}{2}(hVC)_{i+1,j} & \text{if } V < 0. \end{cases} \tag{5.12}$$

Second-Order Central Scheme

The central difference scheme offers a simple and symmetric second-order approximation of the advective fluxes. It computes the value of the advected quantity at the interface using an average between the left and right cells as explained in Ferziger & Perić [2002].

For the x-direction, the flux at the interface is approximated as

$$(hUC)_{i,j+1/2} = \frac{1}{2}\Big[(hUC)_{i,j} + (hUC)_{i,j+1}\Big], \tag{5.13}$$

and similarly

$$(hUC)_{i,j-1/2} = \frac{1}{2}\Big[(hUC)_{i,j} + (hUC)_{i,j-1}\Big]. \tag{5.14}$$

Thus, the divergence of the flux is

$$(hUC)_{i,j+1/2} - (hUC)_{i,j-1/2} = \frac{1}{2}\Big[(hUC)_{i,j+1} - (hUC)_{i,j-1}\Big]. \tag{5.15}$$

The same formulation applies in the y-direction

$$(hVC)_{i+1/2,j} = \frac{1}{2}\Big[(hVC)_{i,j} + (hVC)_{i+1,j}\Big], \tag{5.16}$$

$$(hVC)_{i-1/2,j} = \frac{1}{2}\Big[(hVC)_{i,j} + (hVC)_{i-1,j}\Big]. \tag{5.17}$$

Second-Order Scheme Alternative

In the x-direction, the flux at the right face $j + 1/2$ is discretized as

$$(hUC)_{i,j+1/2} \approx \begin{cases} (hUC)_{i,j} + \frac{1}{4}\Big[(hUC)_{i,j+1} - (hUC)_{i,j-1}\Big] & \text{if } U \geq 0, \\ (hUC)_{i,j+1} + \frac{1}{4}\Big[(hUC)_{i,j} - (hUC)_{i,j+2}\Big] & \text{if } U < 0, \end{cases} \tag{5.18}$$

and similarly, the left face $j - 1/2$ is approximated by

$$(hUC)_{i,j-1/2} \approx \begin{cases} (hUC)_{i,j-1} + \frac{1}{4}\Big[(hUC)_{i,j} - (hUC)_{i,j-2}\Big] & \text{if } U \geq 0, \\ (hUC)_{i,j} + \frac{1}{4}\Big[(hUC)_{i,j-1} - (hUC)_{i,j+1}\Big] & \text{if } U < 0. \end{cases} \tag{5.19}$$

The same logic applies in the y-direction. The face $i - 1/2$ and face $i + 1/2$ fluxes are given by

$$(hVC)_{i+1/2,j} \approx \begin{cases} (hVC)_{i,j} + \frac{1}{4}\Big[(hVC)_{i+1,j} - (hVC)_{i-1,j}\Big] & \text{if } V \geq 0, \\ (hVC)_{i+1,j} + \frac{1}{4}\Big[(hVC)_{i,j} - (hVC)_{i+2,j}\Big] & \text{if } V < 0, \end{cases} \tag{5.20}$$

$$(hVC)_{i-1/2,j} \approx \begin{cases} (hVC)_{i-1,j} + \frac{1}{4}\Big[(hVC)_{i,j} - (hVC)_{i-2,j}\Big] & \text{if } V \geq 0, \\ (hVC)_{i,j} + \frac{1}{4}\Big[(hVC)_{i-1,j} - (hVC)_{i+1,j}\Big] & \text{if } V < 0. \end{cases} \tag{5.21}$$

Limited Second-Order Upwind Scheme

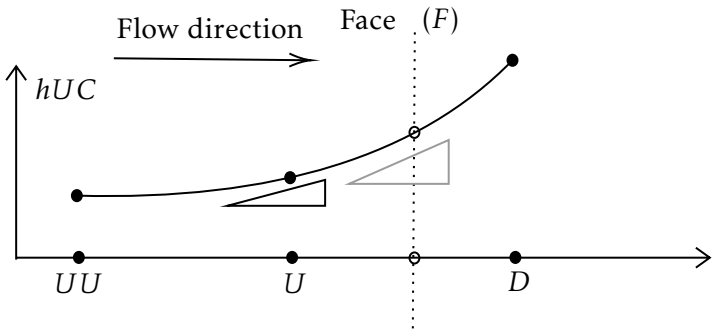

Figure 5.2: Stencil used in the limited second-order upwind scheme. The face value $(hUC)_F$ is reconstructed using the upwind value U and a linear extrapolation involving the upstream values UU and U. The black triangle on the left illustrates the variation of the quantity between the distant upstream cell UU and the downwind cell D, while the gray triangle shows the variation between the immediate upstream U and D. These variations are combined in a specific expression r used to control the limiter coefficient $\beta(r)$, which governs the interpolation. Representation adapted from CFD Direct [2025].

In order to reduce the numerical diffusion of the first-order upwind scheme, a limited second-order upwind scheme can be used. This approach blends the robustness of the upwind method with the accuracy of a second-order linear scheme by applying a flux limiter as explained in CFD Direct [2025].

The flux at a face $(hUC)_F$ is interpolated using a combination between the first-order upwind value and the second-order extrapolated value. The general form is

$$(hUC)_F = (1-\beta)(hUC)_U + \beta(hUC)_L, \tag{5.22}$$

where:

- $(hUC)_U$ is the value at the upwind cell,
- $(hUC)_L$ is the linear extrapolated value using the two upstream points,
- $\beta \in [0,2]$ is a flux limiter.

The extrapolated value $(hUC)_L$ is typically constructed using a central difference

$$(hUC)_L = \frac{(hUC)_U + (hUC)_D}{2}, \tag{5.23}$$

where $(hUC)_D$ denotes the value at the downwind cell.

The limiter coefficient $\beta(r)$ is computed from a nonlinear expression involving variations of the advected quantity between several neighbouring cells as shown in Figure 5.2. It is defined as

$$r = \max\left[2\frac{(hUC)_D - (hUC)_{UU}}{2((hUC)_D - (hUC)_U)} - 1, 0\right], \tag{5.24}$$

where$(hUC)_{UU}$ is the value at the second upstream cell.

To compute the coefficient $\beta(r)$, various flux limiter functions based on the Total Variation Diminishing (TVD) principle can be employed. These limiters are designed to combine the accuracy of higher-order schemes with the stability of first-order methods by preventing spurious oscillations near steep gradients. In this work, several limiters are evaluated, including Minmod, limited linear, van Leer, Superbee, and van Albada, following the formulations presented in CFD Direct [2025] and LeVeque [2002]. Each of these schemes has specific characteristics in terms of numerical diffusion, preservation of symmetry, and smoothness of the reconstructed profile. The limiter selected for the final simulations is specified in a subsequent section.

5.2.3 Discretization of Diffusive Terms

The diffusive terms are approximated using midpoint method as detailed in Riflet [2023]. For the sake of simplicity, the gradient terms are discretized using directly the gradient of the conservative unknown hC. The influence of this simplification remains limited as long as gradient in water depth are also limited, which is the case in all scenarios considered in this thesis.

Discretization Along x-Direction

The two first terms for diffusive part in x-direction are approximated as

$$\left(\frac{h\partial C}{\partial x}\right)_{i,j+1/2} \approx \frac{(hC)_{i,j+1} - (hC)_{i,j}}{\Delta x}, \tag{5.25}$$

$$\left(\frac{h\partial C}{\partial x}\right)_{i,j-1/2} \approx \frac{(hC)_{i,j} - (hC)_{i,j-1}}{\Delta x}, \tag{5.26}$$

and give

$$\left(D_{xx}\frac{h\partial C}{\partial x}\right)_{i,j+1/2} - \left(D_{xx}\frac{h\partial C}{\partial x}\right)_{i,j-1/2} \approx \left[D_{xx,i,j+1/2}\frac{(hC)_{i,j+1} - (hC)_{i,j}}{\Delta x} - D_{xx,i,j-1/2}\frac{(hC)_{i,j} - (hC)_{i,j-1}}{\Delta x}\right]. \tag{5.27}$$

Discretization Along y-Direction

Following the same methodology as for x–direction, it gives

$$\left(D_{yy}\frac{h\partial C}{\partial y}\right)_{i+1/2,j} - \left(D_{yy}\frac{h\partial C}{\partial y}\right)_{i-1/2,j} \approx \left[D_{yy,i+1/2,j}\frac{(hC)_{i+1,j} - (hC)_{i,j}}{\Delta y} - D_{yy,i-1/2,j}\frac{(hC)_{i,j} - (hC)_{i-1,j}}{\Delta y}\right]. \tag{5.28}$$

Discretization Along xy-Direction

In the presence of anisotropic diffusion, cross-diffusion terms must be considered. These terms account for directional mixing effects and are discretized following the same methodology as for the simple x, y diffusion terms

$$\left(\frac{h\partial C}{\partial x}\right)_{i-1/2,j} \approx \frac{(hC)_{i-1/2,j+1} - (hC)_{i-1/2,j-1}}{2\Delta x}, \tag{5.29}$$

$$\left(\frac{h\partial C}{\partial x}\right)_{i+1/2,j} \approx \frac{(hC)_{i+1/2,j+1} - (hC)_{i+1/2,j-1}}{2\Delta x}, \tag{5.30}$$

and

$$\left(D_{xy}\frac{h\partial C}{\partial x}\right)_{i+1/2,j} - \left(D_{xy}\frac{h\partial C}{\partial x}\right)_{i-1/2,j} \approx \frac{1}{2\Delta x}\Big[D_{xy,i+1/2,j}\Big((hC)_{i+1/2,j+1} - (hC)_{i+1/2,j-1}\Big) \tag{5.31}$$

$$-D_{xy,i-1/2,j}\Big((hC)_{i-1/2,j+1} - (hC)_{i-1/2,j-1}\Big)\Big]. \tag{5.32}$$

However, the terms in the numerator of this equation are not known, a central method approximation is needed

$$(hC)_{i-1/2,j+1} \approx \frac{(hC)_{i-1,j+1} + (hC)_{i,j+1}}{2}, \tag{5.33}$$

$$(hC)_{i-1/2,j-1} \approx \frac{(hC)_{i-1,j-1} + (hC)_{i,j-1}}{2}, \tag{5.34}$$

$$(hC)_{i+1/2,j+1} \approx \frac{(hC)_{i+1,j+1} + (hC)_{i,j+1}}{2}, \tag{5.35}$$

$$(hC)_{i+1/2,j-1} \approx \frac{(hC)_{i+1,j-1} + (hC)_{i,j-1}}{2}. \tag{5.36}$$

Discretization Along yx-Direction

Similarly to the xy-direction, the anisotropic diffusion in the yx-direction must be discretized to account for cross-diffusion effects. These terms are approximated using the same methodology as for the standard diffusion terms

$$\left(\frac{h\partial C}{\partial y}\right)_{i,j-1/2} \approx \frac{(hC)_{i+1,j-1/2} - (hC)_{i-1,j-1/2}}{2\Delta y}, \tag{5.37}$$

$$\left(\frac{h\partial C}{\partial y}\right)_{i,j+1/2} \approx \frac{(hC)_{i+1,j+1/2} - (hC)_{i-1,j+1/2}}{2\Delta y}, \tag{5.38}$$

which leads to the discrete approximation of the diffusion term

$$\left(D_{yx}\frac{h\partial C}{\partial y}\right)_{i,j+1/2} - \left(D_{yx}\frac{h\partial C}{\partial y}\right)_{i,j-1/2} \approx \frac{1}{2\Delta y}\Big[D_{yx,i,j+1/2}\Big((hC)_{i+1,j+1/2} - (hC)_{i-1,j+1/2}\Big) \tag{5.39}$$

$$-D_{yx,i,j-1/2}\Big((hC)_{i+1,j-1/2} - (hC)_{i-1,j-1/2}\Big)\Big]. \tag{5.40}$$

However, the values at the numerator are unknown, requiring further approximations

$$(hC)_{i+1,j-1/2} \approx \frac{(hC)_{i+1,j-1} + (hC)_{i+1,j}}{2}, \tag{5.41}$$

$$(hC)_{i-1,j-1/2} \approx \frac{(hC)_{i-1,j-1} + (hC)_{i-1,j}}{2}, \tag{5.42}$$

$$(hC)_{i+1,j+1/2} \approx \frac{(hC)_{i+1,j+1} + (hC)_{i+1,j}}{2}, \tag{5.43}$$

$$(hC)_{i-1,j+1/2} \approx \frac{(hC)_{i-1,j+1} + (hC)_{i-1,j}}{2}. \tag{5.44}$$

Finally, by considering all the cross diffusive terms, it gives

$$-\Delta x\left[\left(D_{xy}\frac{h\partial C}{\partial y}\right)_{i,j+1/2}-\left(D_{xy}\frac{h\partial C}{\partial y}\right)_{i,j-1/2}\right]-\Delta y\left[\left(D_{yx}\frac{h\partial C}{\partial x}\right)_{i+1/2,j}-\left(D_{yx}\frac{h\partial C}{\partial x}\right)_{i-1/2,j}\right]= \tag{5.45}$$

$$-\frac{\Delta x}{4\Delta y}\left[D_{xy,i,j+1/2}(hC)_{i+1,j+1}-D_{xy,i,j+1/2}(hC)_{i-1,j+1}-D_{xy,i,j-1/2}(hC)_{i+1,j-1}+D_{xy,i,j-1/2}(hC)_{i-1,j-1}\right] \tag{5.46}$$

$$-\frac{\Delta y}{4\Delta x}\left[D_{yx,i+1/2,j}(hC)_{i+1,j+1}-D_{yx,i+1/2,j}(hC)_{i+1,j-1}-D_{yx,i-1/2,j}(hC)_{i-1,j+1}+D_{yx,i-1/2,j}(hC)_{i-1,j-1}\right]. \tag{5.47}$$

These formulations ensure an accurate representation of diffusion in both isotropic and anisotropic environments.

5.2.4 Boundary Conditions

To ensure pollutant evacuation at the outlet and prevent accumulation within the network, advective terms are applied. No specific condition is imposed at the inlet. However, if a mixed pollutant is introduced, it can be incorporated as a source term.

The formulation of the pollutant transport at the outlet follows a zero-gradient boundary condition. This ensures that the pollutant concentration at the outlet remains equal to the last computed value inside the domain, preventing artificial reflections and preserving the natural advective transport

$$\begin{cases}\left.\dfrac{\partial(hUC)}{\partial x}\right|_{\text{outlet}}=0, & \text{if the outlet is along the } y\text{-direction,}\\ \left.\dfrac{\partial(hVC)}{\partial y}\right|_{\text{outlet}}=0, & \text{if the outlet is along the } x\text{-direction.}\end{cases} \tag{5.48}$$

At the inlet, no explicit concentration condition is imposed unless a pollutant source is introduced. In such a case, the pollutant is treated as a source term, directly influencing the local concentration through

$$S_{i,j}^{n}=Q_pC_p, \tag{5.49}$$

where:

- Q_p represents the pollutant injection rate,
- C_p is the concentration of the injected pollutant.

This ensures that the inflow of pollutants is incorporated into the numerical scheme, while regions without explicit sources remain governed by the natural evolution of the flow field.

5.3 Time Discretization

The temporal discretization of the advection-diffusion equation is performed using an explicit Euler scheme, as presented in the fully discretized formulation of Equation (5.58). In this study, a first-order explicit Euler scheme is used to advance the concentration field based only on information available at the current time step.

5.3.1 Explicit Euler Method

The explicit Euler method is a first-order time-stepping scheme that approximates the time derivative using a forward difference [Ferziger & Perić, 2002; LeVeque, 2002]

$$\frac{(hC)_{i,j}^{n+1} - (hC)_{i,j}^{n}}{\Delta t} = \mathcal{L}((hC)_{i,j}^{n}), \tag{5.50}$$

where $\mathcal{L}((hC))$ represents the discrete spatial operator applied to hC, including advection and diffusion terms. The explicit Euler update is then given by

$$(hC)_{i,j}^{n+1} = (hC)_{i,j}^{n} + \Delta t\, \mathcal{L}((hC)_{i,j}^{n}). \tag{5.51}$$

5.3.2 Numerical Stability Condition

While computationally efficient, the explicit scheme is subject to stability constraints to ensure numerical accuracy and prevent divergence. The Courant-Friedrichs-Lewy (CFL) condition [Courant et al., 1928] governs the stability of the advection term, while an analogous constraint applies to the diffusion term.

The CFL condition, initially proposed by Courant, Friedrichs, and Lewy [Courant et al., 1928], ensures that the numerical advection term remains stable by limiting the time step Δt according to the maximum velocity magnitude in the domain. The Courant number Co is defined as

$$Co = \max_{i,j}\left(\frac{\sqrt{(U)_{i,j}^{2} + (V)_{i,j}^{2}}}{\Delta x}\right)\Delta t. \tag{5.52}$$

For numerical stability, the CFL condition imposes

$$Co \leq 1 \quad \Rightarrow \quad \Delta t \leq \frac{\Delta x}{\max_{i,j}\sqrt{(U)_{i,j}^{2} + (V)_{i,j}^{2}}}. \tag{5.53}$$

A commonly used choice to balance stability and minimize numerical diffusion is $Co = 0.5$.

In the presence of anisotropic diffusion, an additional stability constraint must be satisfied to ensure that numerical diffusion remains stable. The stability of numerical diffusion is governed by the Péclet number Pe, which accounts for the anisotropic diffusion effects. Following the approach presented in Liu [2019] and Fang et al. [2022], the Péclet number is defined as

$$Pe = \max_{i,j}\left\{\frac{\left|(D_{xx} + D_{xy})n_x + (D_{xy} + D_{yy})n_y\right|}{\Delta x^2}\right\}\Delta t, \tag{5.54}$$

where $\mathbf{n} = (n_x, n_y)$ is the normal unit vector at the grid point (i, j). To maintain numerical stability, the condition $Pe \leq 1$ must be enforced, leading to

$$\Delta t \leq \frac{\Delta x^2}{\max_{i,j}\left|(D_{xx} + D_{xy})n_x + (D_{xy} + D_{yy})n_y\right|}. \tag{5.55}$$

To ensure stability under the most conservative scenario, the direction vector components n_x and n_y are chosen to maximize the contribution of all tensor terms. Therefore, $n_x = n_y = 1$, corresponding to the worst-case alignment where all diffusion terms add constructively.

Finally, both advection and diffusion constraints must be satisfied simultaneously. The final stability criterion, as proposed in Liu [2019] and Fang et al. [2022], is given by

$$Co + Pe \leq 1. \tag{5.56}$$

To ensure sufficient time step refinement, one can define a constant $\alpha \leq 1$ such that the sum of the Courant and Péclet numbers remains bounded

$$Co + Pe \leq \alpha, \tag{5.57}$$

where α is set to 0.5 in this study to guarantee numerical accuracy.

5.4 Fully Discretized Advection-Diffusion Equation

The numerical resolution of the pollutant transport problem is based on the depth-averaged advection-diffusion equation, previously introduced in Equation (3.13). Spatial discretizations have been presented in the previous sections for both advection and diffusion, using first and second order upwind schemes for the former and centered schemes for the latter.

All simulations in this work employ explicit Euler time integration, where the update from time step n to $n+1$ follows

$$\frac{(hC)_{i,j}^{n+1} - (hC)_{i,j}^{n}}{\Delta t} + \frac{1}{\Delta x} F_{i,j}^{n} + \frac{1}{\Delta y} G_{i,j}^{n} = D_W^n + D_S^n + D_E^n + D_N^n + S_{i,j}^n, \tag{5.58}$$

where:

- $F_{i,j}^n$, $G_{i,j}^n$: advective fluxes in x- and y-directions at time t^n, depend on the numerical schemes that is used,
- $D_E^n, D_W^n, D_N^n, D_S^n$: directional diffusive contributions centered on cell (i,j) at time t^n,
- $S_{i,j}^n$: source term at time t^n.

The grouped diffusive fluxes are defined as follows:

$$D_E^n = \frac{D_{x,i,j+1/2}^n}{2\Delta x^2}\left[(hC)_{i,j+1}^n - (hC)_{i,j}^n\right] - \frac{D_{xy,i-1/2,j}^n}{4\Delta x\Delta y}\left[(hC)_{i-1,j+1}^n - (hC)_{i-1,j-1}^n\right] - \frac{D_{xy,i,j}^n}{4\Delta x\Delta y}\left[(hC)_{i,j+1}^n - (hC)_{i,j-1}^n\right], \tag{5.59}$$

$$D_W^n = \frac{D_{x,i,j-1/2}^n}{2\Delta x^2}\left[(hC)_{i,j-1}^n - (hC)_{i,j}^n\right] + \frac{D_{xy,i+1/2,j}^n}{4\Delta x\Delta y}\left[(hC)_{i+1,j+1}^n - (hC)_{i+1,j-1}^n\right] + \frac{D_{xy,i,j}^n}{4\Delta x\Delta y}\left[(hC)_{i,j+1}^n - (hC)_{i,j-1}^n\right], \tag{5.60}$$

$$D_N^n = \frac{D_{y,i+1/2,j}^n}{2\Delta y^2}\left[(hC)_{i+1,j}^n - (hC)_{i,j}^n\right] + \frac{D_{yx,i,j+1/2}^n}{4\Delta x\Delta y}\left[(hC)_{i+1,j+1}^n - (hC)_{i-1,j+1}^n\right] + \frac{D_{yx,i,j}^n}{4\Delta x\Delta y}\left[(hC)_{i+1,j}^n - (hC)_{i-1,j}^n\right], \tag{5.61}$$

$$D_S^n = \frac{D_{y,i-1/2,j}^n}{2\Delta y^2}\left[(hC)_{i-1,j}^n - (hC)_{i,j}^n\right] - \frac{D_{yx,i,j-1/2}^n}{4\Delta x\Delta y}\left[(hC)_{i+1,j-1}^n - (hC)_{i-1,j-1}^n\right] - \frac{D_{yx,i,j}^n}{4\Delta x\Delta y}\left[(hC)_{i+1,j}^n - (hC)_{i-1,j}^n\right]. \tag{5.62}$$

5.5 Numerical Implementation

This section describes the numerical implementation of the pollutant transport model in a steady and unsteady framework. The model solves the two-dimensional depth-averaged advection-diffusion equation using a FVM. The numerical solver is implemented in Python [2022].

5.5.1 Code Structure

The numerical model follows a structured workflow to solve the two-dimensional advection-diffusion equation using the FVM with an explicit Euler time-stepping scheme as detailed in previous sections. The overall code workflow is illustrated in Figure 5.3 and consists of the following steps:

1. **Reading input data**: The model reads hydrodynamic data (specific discharges hU, hV and water depth h) from the Wolf 2D model outputs and sets computational parameters.

2. **Grid and variable initialization**: The computational domain is discretized using a structured Cartesian grid, with pollutant concentration variables hC assigned to each cell.

3. **Numerical operators setup**: Advection is discretized using different schemes with optional flux limiting, while diffusion uses centered differences.

4. **Sparse matrix assembly**: A sparse matrix formulation is used to store and solve the system efficiently.

5. **Time integration loop**: The explicit Euler method iterates over time, updating hC in each step.

6. **Result storage and visualization**: Simulation outputs are stored at predefined time steps and visualized through concentration maps and animations.

A distinction between the steady and unsteady cases lies in the treatment of hydrodynamic inputs and the frequency of matrix assembly. In the steady-state configuration, the discharge and water depth fields extracted from Wolf 2D are time-averaged over the entire simulation duration, and a single advection-diffusion matrix is constructed and applied uniformly at each time step. In contrast, the unsteady configuration relies on time-resolved hydrodynamic data, requiring a new matrix to be assembled at each hydrodynamic time frame to reflect the instantaneous flow field. This bifurcation is visually summarized in Figure 5.3. A more detailed explanation of how the hydrodynamic fields are processed and coupled with the transport solver is provided in the following sections.

5.5.2 Sparse Matrix Formulation

The pollutant transport model is implemented using a sparse matrix formulation to efficiently solve the advection-diffusion equation. This approach reduces memory usage and computational cost, particularly for large-scale simulations. The governing equation, resulting in a system of equations, can be expressed in matrix form. The sparse matrix $\mathbf{A}$ is assembled by iterating over all valid computational cells and filling in the appropriate coefficients for advection and diffusion.

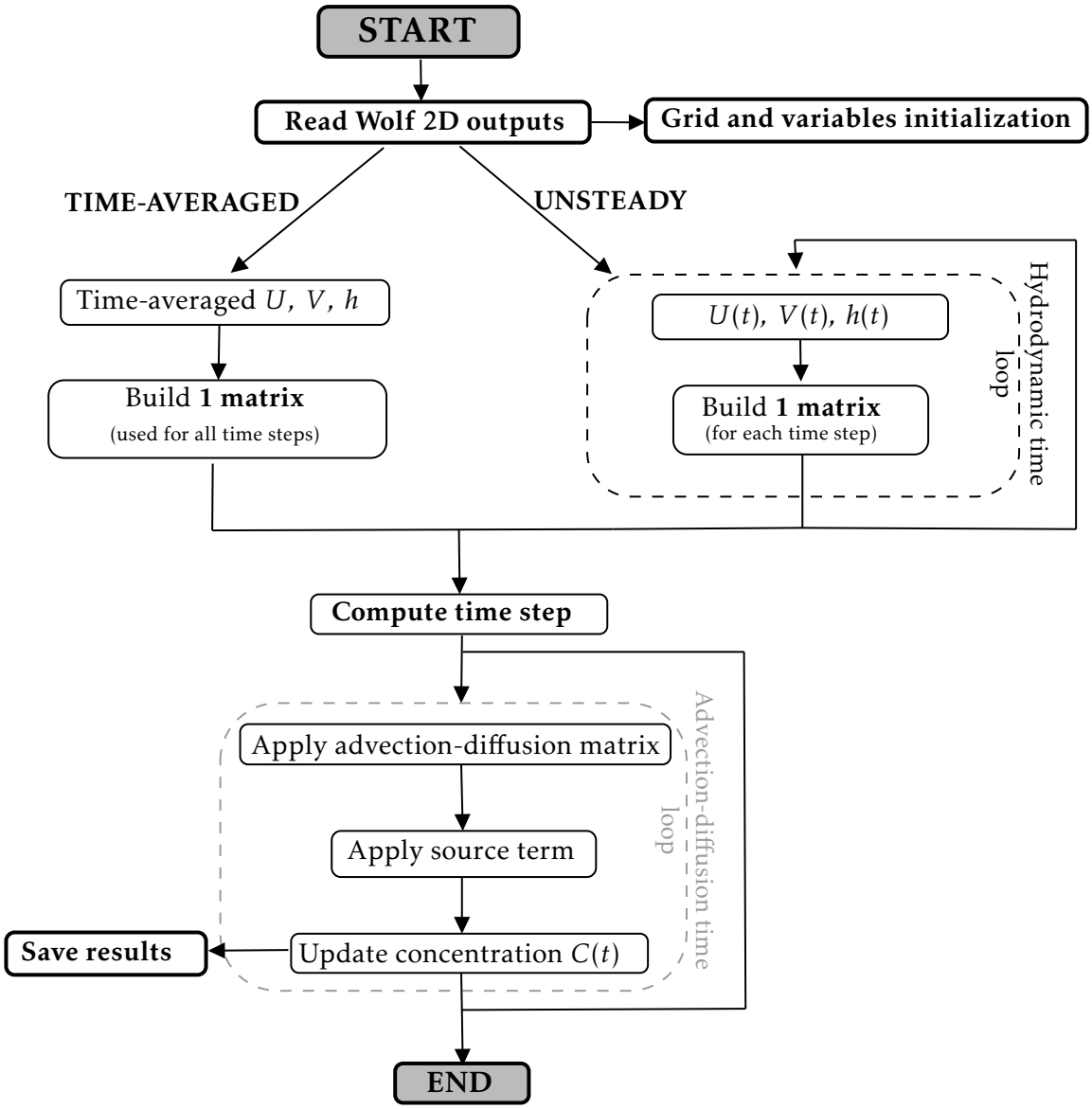

Figure 5.3: Flowchart illustrating the simulation workflow for solving the two-dimensional advection-diffusion equation. The procedure begins with reading hydrodynamic outputs from the Wolf 2D model and proceeds with a bifurcation between steady (time-averaged) and unsteady configurations. For the time-averaged case, a single advection-diffusion matrix is constructed and reused throughout the simulation. In the unsteady case, a new matrix is built at each hydrodynamic time step. In both cases, the pollutant concentration field is updated over time using an explicit Euler scheme with matrix-vector operations, source term addition, and periodic result storage.

The explicit Euler scheme updates the pollutant concentration at each cell using

$$(hC)^{n+1} = (hC)^n + \Delta t\,(\mathbf{A}(hC)^n + \mathbf{b}), \tag{5.63}$$

where:

- **A** is the sparse coefficient matrix, containing advection and diffusion terms,

- hC is the vector of unknown pollutant mass per unit area at each computational cell, resulting from the product of water depth h and depth-averaged concentration C,
- **b** represents source terms and external forcing.

The matrix **A** assembly is organized direction by direction, by systematically looping over all internal cells and computing flux interactions with their neighbours as showed in Figure 5.4. For each direction, the stencil is applied from two perspectives once from the current cell, and once from one of its neighbour ensuring both conservation and symmetry. The following logic is used:

- **East-West direction (x-axis):** For a given cell (i, j), the horizontal flux across the vertical face between $(i, j-1)$ and (i, j) is computed. The resulting contributions, both diffusive and advective, are distributed into the matrix rows corresponding to each cell. Depending on the numerical scheme, the stencil may involve not only these two adjacent cells but also additional upstream or diagonal neighbours.
- **North-South direction (y-axis):** Similarly, the vertical flux across the horizontal face between cells $(i-1, j)$ and (i, j) is computed. The resulting contributions are assembled into the matrix rows of both cells. As in the horizontal case, the stencil may involve additional neighbouring cells depending on the numerical scheme, such as second-order reconstructions or anisotropic cross-diffusion.
- **Cross-diffusion (diagonal fluxes):** For anisotropic diffusion, diagonal interactions are included. These are handled in two steps:
  1. The stencil is centered at the current cell (i, j), to compute South and West cross-fluxes.
  2. The stencil is shifted to the western neighbour $(i, j-1)$, to compute North and East cross-fluxes.

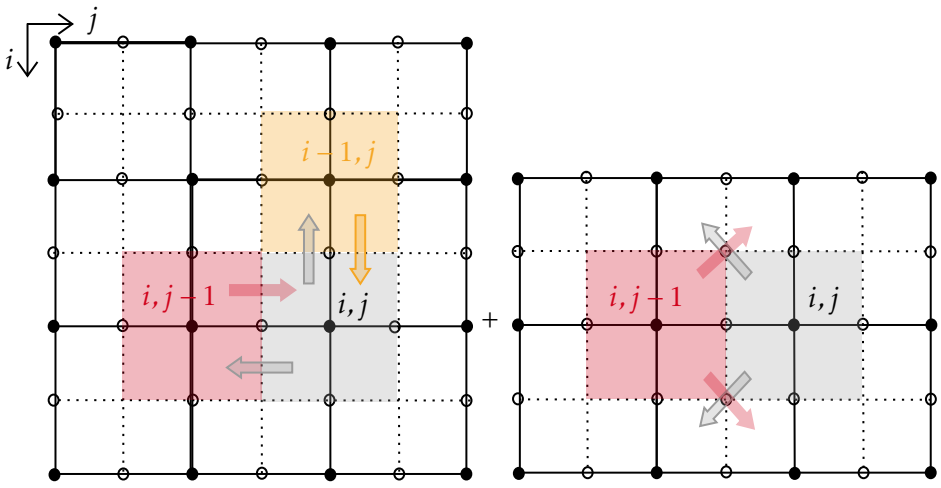

Figure 5.4: Visualization of the diffusion matrix assembly for cell (i, j), including both directional and anisotropic cross-diffusion. The stencil is applied at (i, j) and shifted to $(i, j-1)$ to compute all flux contributions as described in the diffusion part of the assembly procedure.

The global matrix is sparse, with each row corresponding to a computational cell and containing non-zero entries only for that cell and a limited number of neighbours, as determined by the numerical discretization scheme. To further accelerate performance, the matrix assembly routine is fully JIT-compiled using the `@njit` decorator from the `Numba` library [Lam et al., 2015]. This reduces the overhead of Python loops during the stencil evaluation. Once assembled, the CSR matrix is converted to a PyTorch sparse tensor format [Paszke et al., 2019], enabling GPU acceleration or efficient sparse matrix operations on CPU.

5.5.3 Time-Stepping and Hydrodynamic Updates

The pollutant transport model uses an explicit Euler time integration scheme to solve the advection-diffusion equation. However, the hydrodynamic inputs, such as discharge and water depth fields, are only available at discrete time intervals from the Wolf 2D simulation. To resolve pollutant transport more finely within each hydrodynamic frame, a smaller computational time step is imposed based on the Courant-Friedrichs-Lewy (CFL) condition, as described in Section 5.3.1.

The simulation is structured around two nested time loops:

- **Outer loop:** Advances through hydrodynamic frames, updating the velocity and depth fields at fixed time intervals.
- **Inner loop:** Performs advection-diffusion updates at finer time steps within each hydrodynamic interval.

At each computational time step, the model checks whether the current time t still lies within the bounds of the active hydrodynamic frame. If this is no longer the case, the hydrodynamic fields are updated to the next frame. Since the computational time steps do not exactly align with the frame boundaries, the switch to the next hydrodynamic state may occur just after the defined frame time. This nested approach ensures that pollutant transport is resolved at a sufficiently high temporal resolution, while remaining synchronized with the coarser hydrodynamic inputs. A schematic overview of this time-stepping strategy is shown in Figure 5.5.

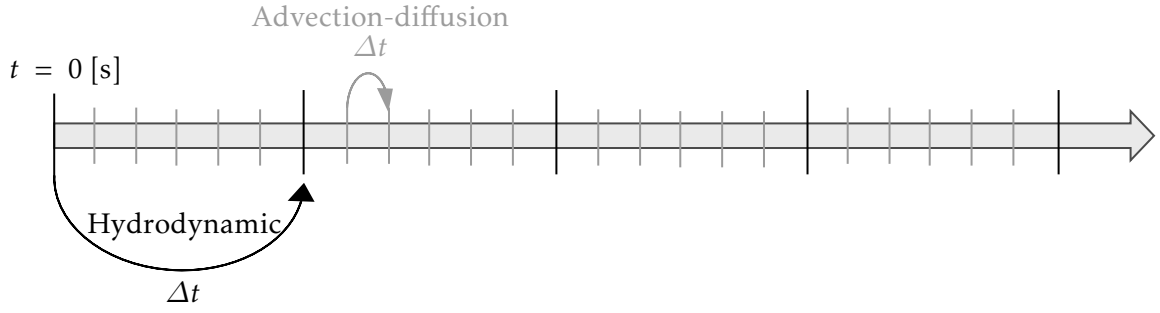

Figure 5.5: Schematic representation of the time-stepping procedure. The hydrodynamic fields are updated at fixed intervals, while the advection-diffusion solver advances with smaller time steps to ensure numerical stability and accuracy. In this idealized case, the update frequencies are synchronized such that the pollutant transport time steps align exactly with the hydrodynamic output intervals.

5.6 Hydrodynamic and Frame Treatment

Two distinct modelling strategies are employed depending on whether the hydrodynamic forcing is treated as steady or unsteady. These strategies directly affect the way advection-diffusion operators are constructed and used during the simulation.

5.6.1 Steady Hydrodynamics

In the steady case, the hydrodynamic fields are averaged over the entire duration of the Wolf simulation. This results in a single velocity and depth field that is used throughout the pollutant transport simulation. This approach reduces computational cost, as only one advection-diffusion matrix needs to be assembled and reused at every time step.

5.6.2 Unsteady Hydrodynamics

In contrast, the unsteady case uses the full time-resolved output from Wolf 2D, where each frame corresponds to a specific snapshot of the velocity and depth fields. A new sparse matrix must be assembled for each of these frames, and the simulation alternates between them as it evolves in time.

The number of sparse matrices to be constructed grows proportionally with the number of hydrodynamic frames. A large number of frames increases memory usage, as each frame requires storing a large sparse matrix. It also raises the computational cost, since solving multiple sparse linear systems remains expensive, even when using optimized solvers. To mitigate this, the periodicity of the velocity field is exploited: the smallest representative sequence is identified and repeated over time.

Frame Selection

The hydrodynamic velocity field $u(x, y, t)$ used in the advection-diffusion simulation is extracted from the Wolf 2D model at predefined spatial locations. For the present study, the focus is on the configuration **C1**, where the velocity is sampled at a specific observation point located in the middle of the block, in front of one of the openings. This location is chosen to capture the characteristic oscillatory behavior of the flow field driven by periodic forcing.

The goal is to identify the dominant period of oscillation in the velocity signal $u(t)$ at this point and use it to extract a representative periodic sequence of hydrodynamic frames. This representative segment will then be repeated during the pollutant transport simulation to reduce computational cost, while maintaining fidelity to the underlying flow dynamics. A schematic representation of the velocity capture process for the three configurations is provided in Figure 5.6, illustrating the spatial location of the sampled velocity for each case. In the present study, only block **C1** is used.

To identify the periodic behavior of the velocity, Welch method [Welch, 1967] is used to estimate the power spectral density (PSD) of $u(t)$. The PSD allows us to identify the dominant frequency component f_d of the velocity fluctuations, corresponding to the most prominent oscillation in the system. The characteristic period T_d is then estimated as

$$T_d = \frac{1}{f_d}. \tag{5.64}$$

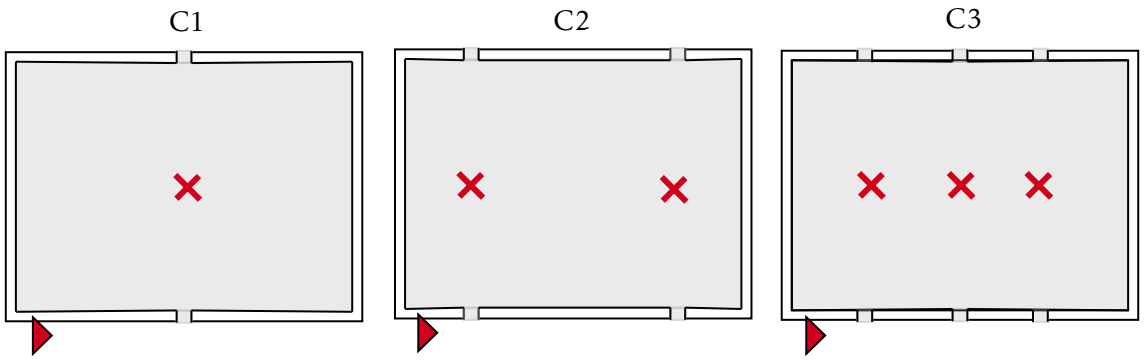

Figure 5.6: Schematic representation of velocity capture in the hydrodynamic model for the three grid configurations. The velocity $u(x, y, t)$ is sampled at predefined locations in front of the openings to extract representative time-dependent signals $u(t)$, which are then analysed for periodicity.

This initial estimate provides an approximation of the periodicity but may be affected by noise or variations in the velocity signal.

To refine the period estimation, the temporal structure of the signal is analysed by detecting the peaks of $u(t)$. The function `scipy.signal.find_peaks` is used to identify local maxima, with a constraint on the minimum distance between peaks to avoid detecting spurious fluctuations. This minimum distance is imposed as 90% of the period T_d previously estimated via Welch method, ensuring that closely spaced local oscillations are filtered out. The time intervals T_i between successive peaks (t_{i+1}, t_i) define the instantaneous periods

$$T_i = t_{i+1} - t_i. \tag{5.65}$$

The median value of the detected periods is then used to obtain a more accurate estimate of the actual best period

$$T_{\text{best}} = \text{median}(T_i). \tag{5.66}$$

This refined period ensures that the extracted sequence captures the true oscillatory behavior of the velocity field.

The final selection of the frame count is determined by considering the largest detected period among all the opening configurations. The number of frames per period is then computed as

$$N_{\text{frames}} = \frac{T_{\text{best}}}{\Delta t}, \tag{5.67}$$

where Δt [s] is the time step of the velocity data.

Once the best period T_{best} is determined, a sliding search is performed to select the optimal sequence of N_{frames} consecutive frames that best represents one full oscillation. For this, several candidate sub-sequences of length T_{best} are extracted at different positions along the signal. Each candidate is repeated periodically to reconstruct the full signal over the simulation duration, and the resulting reconstructed signal is compared to the original using a mean squared error criterion. The sub-sequence that minimizes this error is then retained as the optimal periodic pattern. The reconstruction error is quantified using the relative mean squared

error

$$\text{Error}_{\text{rel}} = \frac{\sum_{i=1}^{N}(u^{\text{orig}}(t_i) - u^{\text{rec}}(t_i))^2}{\sum_{i=1}^{N}(u^{\text{orig}}(t_i))^2} \times 100, \tag{5.68}$$

where $u^{\text{orig}}(t_i)$ is the original velocity signal and $u^{\text{rec}}(t_i)$ is the reconstructed one. The segment that minimizes this error is selected as the best representative period.

Configuration C1: Frame Selection

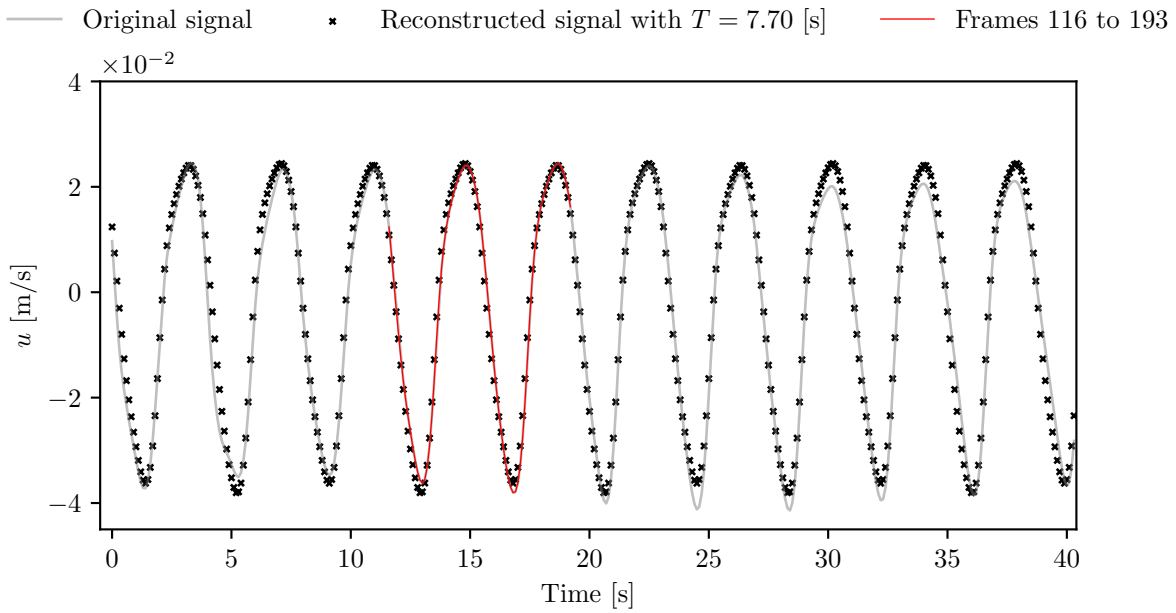

Figure 5.7: Comparison of the original and reconstructed velocity signal at the observation point for configuration **C1**. The original signal (grey line) is obtained from the Wolf 2D output, while the reconstructed signal (black crosses) is generated by repeating the optimal segment of duration $T = 7.70$[s]. The red curve highlights the portion of the original signal that was selected for reconstruction. This reconstruction assumes an ideal scenario where the velocity period is perfectly periodic and matches the selected frame interval. The low reconstruction error (1.61 [%]) confirms the effectiveness of the periodic frame reduction approach.

For the **C1** configuration, the velocity measurement at its designated observation point is analysed for a simulation of 40.4 [s] and 405 frames, yielding the following results

$$T_{\text{best},1} = 7.70 \text{ [s]}. \tag{5.69}$$

Thus, the number of frames per period is

$$N_{\text{frames},1} = \frac{T_{\text{best},1}}{\Delta t} = 77, \tag{5.70}$$

considering a sampling frequency of $f_s = 10$ [Hz] with $\Delta t = 0.1$ [s]. Figure 5.7 shows the comparison between the original and reconstructed velocity signal.

The reconstruction yields a best period of $T_{\text{best},1} = 7.70\,[\text{s}]$, corresponding to 77 frames at a sampling frequency of 10 [Hz]. The optimal sequence used for reconstruction starts at frame 116 and ends at frame 193, following a shift-based minimization of the reconstruction error. The resulting relative error is only 1.61[%], indicating that the extracted segment reproduces the overall oscillatory structure of the signal with good fidelity. This confirms that the velocity field can be effectively approximated using a limited number of frames, without significant loss of temporal accuracy. This reconstructed unsteady hydrodynamic forcing is therefore used consistently throughout all the unsteady simulations presented in Chapter 7.

Chapter 6

Numerical Validation

This chapter presents a series of test cases designed to assess the accuracy, robustness, and numerical behaviour of the implemented advection-diffusion solver. The selected test cases include comparisons with analytical solutions, directional advection tests, and simulations involving anisotropic diffusion with cross-terms. Each scenario is used to isolate and verify specific components of the numerical implementation, such as the advection discretization and the diffusion tensor treatment.

6.1 Solute Transport Simulation

To validate the implemented code and numerical discretization, a reference test case from Fang et al. [2022] is reproduced. The chosen case corresponds to a pollutant release in a 2D rectangular domain under uniform flow conditions. The configuration is particularly suitable for comparison with the analytical solution of the 2D advection-diffusion equation. The goal is to simulate a pollutant injection and compare the numerical solution with the analytical expression at a fixed time, using the same velocity field and physical diffusion parameters. This comparison enables both a verification of the numerical implementation and an initial evaluation of the errors induced by the numerical scheme.

The computational domain is a rectangle of size $800\,[\mathrm{m}] \times 200\,[\mathrm{m}]$, with wall boundaries on the north and south, an inflow on the west, and an outflow on the east. The bed is flat and horizontal, and bottom friction is neglected. The flow is steady, with a uniform depth $h = 1.0\,[\mathrm{m}]$, and a constant horizontal velocity in the x-direction $u = 1.0\,[\mathrm{m/s}]$ ($v = 0.0\,[\mathrm{m/s}]$).

A Gaussian-shaped pollutant is initially introduced at the location $(x_0, y_0) = (0, 100)\,[\mathrm{m}]$, with a total mass $C_0 = 233.06\,[\mathrm{kg}]$. The analytical solution for the depth-averaged concentration $C(t, x, y)$ at time t is given by

$$C(t,x,y) = \frac{C_0/h}{4\pi t\sqrt{D_{xx}D_{yy}}} \exp\left(-\frac{(x-x_0-ut)^2}{4D_{xx}t} - \frac{(y-y_0)^2}{4D_{yy}t}\right), \tag{6.1}$$

where the diffusion coefficients are set to $D_{xx} = 1.02\,[\mathrm{m^2/s}]$ and $D_{yy} = 0.094\,[\mathrm{m^2/s}]$, resulting in an anisotropic spreading of the pollutant (without cross diffusion).

In the simulation, the initial condition at $t = 0$ [s] is directly the analytical solution given in Equation (6.1) evaluated at $t = 60\,[\mathrm{s}]$. The simulation runs for $600\,[\mathrm{s}]$, using a time step Δt that satisfies the CFL and Péclet constraints given in Equation (5.57). The simulations are first

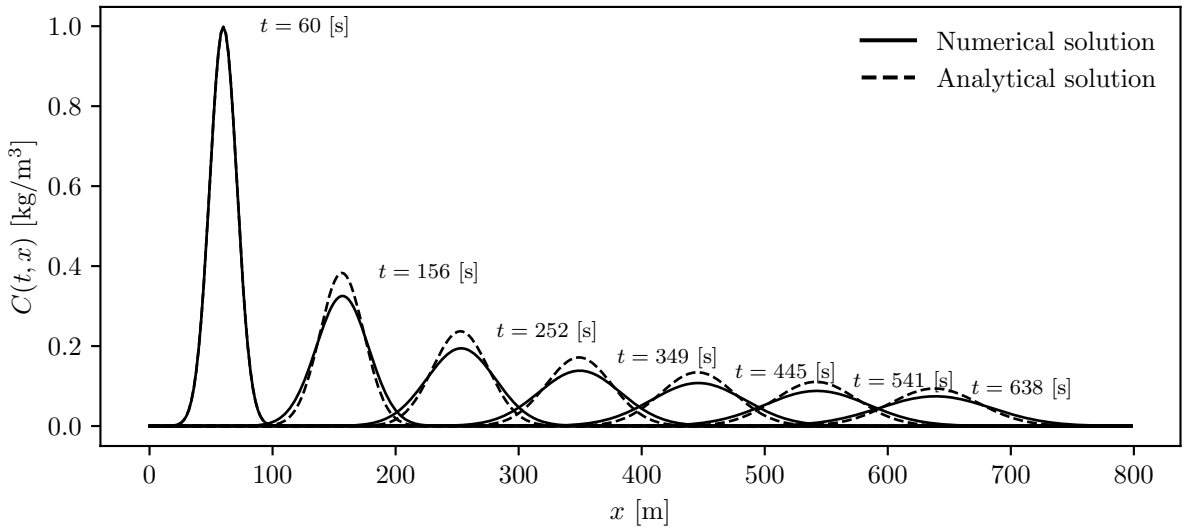

Figure 6.1: Comparison between the numerical (solid lines) and analytical (dashed lines) solutions of the pollutant concentration along the x-axis at different times. The profiles are extracted at $y = 100\,[\mathrm{m}]$, corresponding to the injection location. The simulation is performed with a spatial resolution of $\Delta x = \Delta y = 2\,[\mathrm{m}]$, using a first-order upwind advection scheme. The initial condition corresponds to the analytical solution at $t = 60\,[\mathrm{s}]$.

conducted with an arbitrarily spatial discretization of $\Delta x = \Delta y = 2\,[\mathrm{m}]$. Figure 6.1 shows the evolution of the numerical and analytical solutions at successive time steps, using the first-order upwind scheme as detailed in Section 5.2.2. The profiles are extracted at $y = 100\,[\mathrm{m}]$, corresponding to the injection location. Initially, the numerical profile matches the analytical one. However, as time progresses, the numerical solution becomes increasingly spread, revealing the presence of numerical diffusion.

To quantify this effect, a convergence study is conducted by varying the spatial resolution $\Delta x = \Delta y$ from 5 [m] to 1 [m]. The temporal step Δt is fixed according to the condition explained in Equation (5.57) for each grid. The root-mean-square error (RMSE) is computed at a fixed time $t = 500$ [s], which corresponds to a sufficiently advanced stage of the simulation where the pollutant has significantly spread but remains within the computational domain. This choice ensures a clear comparison between the analytical and numerical solutions, as it allows the differences induced by numerical diffusion to be clearly observed. The root-mean-square error (RMSE) is computed as

$$\mathrm{RMSE}(t) = \sqrt{\frac{1}{N}\sum_{i=1}^{N}\left[C_i^{\mathrm{num}}(t) - C_i^{\mathrm{ana}}(t)\right]^2}, \tag{6.2}$$

where N is the number of points along x at $y = 100$ [m].

In addition to the first-order upwind scheme, four other advection discretization methods introduced in Section 5.2.2 are tested: the second-order upwind scheme and another alternative second-order scheme, the central differencing scheme, and the limited second-order upwind scheme with Minmod limiter. The motivation behind testing multiple methods lies in the need to identify the most appropriate trade-off between numerical accuracy and stability.

In a log-log plot of the numerical error versus the spatial resolution Δx, the slope of each curve provides an estimate of the convergence order of the scheme. For a numerical method of order p, the error is expected to scale as $\mathcal{O}(\Delta x^p)$ as explained by CFD Direct [2025] and LeVeque [2002]. Therefore, a first-order scheme such as the upwind method should exhibit a slope close to 1, while second-order methods (*e.g.* central differencing or second-order upwind) are expected to produce slopes close to 2. In practice, deviations from the theoretical slopes may arise due to oscillations, boundary effects, or insufficient temporal resolution, but the general trend remains a strong indicator of the method spatial accuracy.

Figure 6.2 shows the evolution of the RMSE error between the numerical and analytical solutions at a fixed time $t = 500\,[\mathrm{s}]$, as a function of the grid spacing Δx, in log-log scale. The five numerical schemes exhibit distinct behaviours in terms of accuracy and convergence. The central differencing and second-order upwind schemes exhibit slopes around $1.8 - 1.85$, in good agreement with the theoretical second-order behaviour. The limited scheme, which combines a high-order base scheme with a non-linear flux limiter, results in a convergence rate between first and second order (slope ≈ 1.24). This is consistent with the role of the limiter: it prevents non-physical oscillations near steep gradients, while still allowing for higher-order accuracy in smooth regions. Finally, the classical first-order upwind method shows the lowest slope (≈ 0.59), confirming its limited accuracy and the strong effect of numerical diffusion. For the alternative second-order scheme, only one point could be retained due to its instability at coarser resolutions, preventing any meaningful slope estimation.

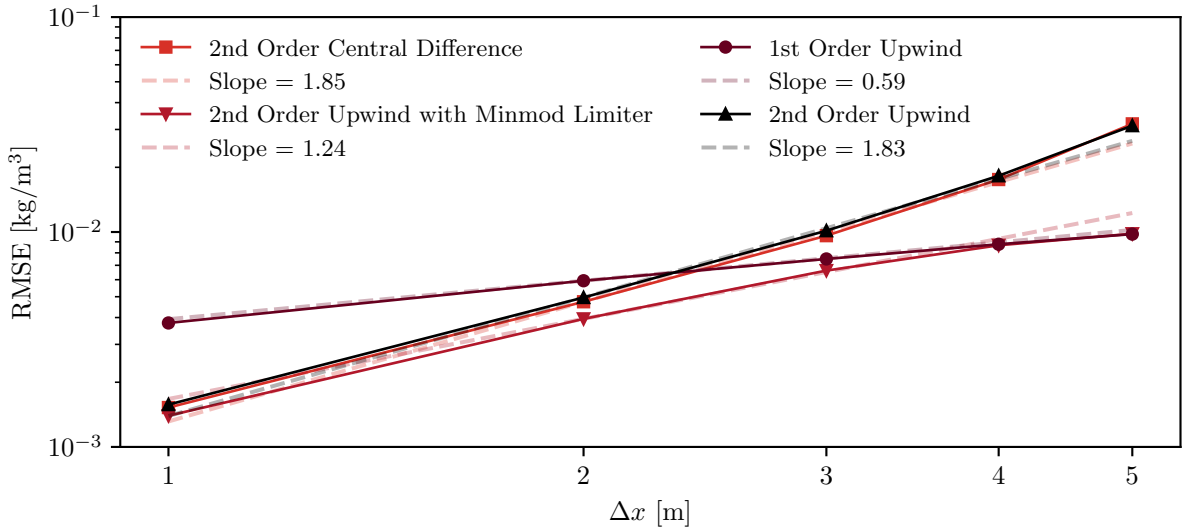

Figure 6.2: RMSE between numerical and analytical concentrations along x at $y = 100\,[\mathrm{m}]$ and $t = 500\,[\mathrm{s}]$, for various values of Δx. Each curve corresponds to a different advection scheme. Dashed lines represent the fitted convergence slopes.

As described in Section 5.2.2, the use of a limited advection scheme requires the definition of a flux limiter function $\beta(r)$, which controls the interpolation between high and low order fluxes depending on the local smoothness of the solution. The smoothness indicator r is defined in Equation (5.2.2). The choice of this limiter function of r has an impact on the balance between numerical accuracy and stability.

Limiter	**RMSE** $\times 10^3$ [kg/m^3]	**Relative error** [%]
Minmod	1.397	4.384
Superbee	1.681	5.274
van Leer	1.535	4.815
van Albada	1.528	4.796
Limited linear	1.525	4.786
Linear (no limiter)	3.775	11.844

Table 6.1: RMSE and relative error at $t = 500\,[\mathrm{s}]$ for different flux limiters, using $\Delta x = 1\,[\mathrm{m}]$.

To determine the most appropriate limiter for the current test case, several classical expressions of $\beta(r)$ are tested and compared. These include the Minmod, Superbee, van Leer, van Albada, and a linear reconstruction without limiting. Based on CFD Direct [2025] and LeVeque [2002], the different limiter functions $\beta(r)$ are defined as follows:

- Minmod limiter:
$$\beta_{\text{Minmod}}(r) = \min(r, 1), \tag{6.3}$$
- Limited linear limiter:
$$\beta_{\text{linear}}(r) = \min(2r, 1), \tag{6.4}$$
- Superbee limiter:
$$\beta_{\text{Superbee}}(r) = \max[0, \min(2r, 1), \min(r, 2)], \tag{6.5}$$
- van Leer limiter:
$$\beta_{\text{van Leer}}(r) = \frac{r + |r|}{1 + |r|}, \tag{6.6}$$
- van Albada limiter:
$$\beta_{\text{van Albada}}(r) = \frac{r^2 + r}{r^2 + 1}, \tag{6.7}$$
- Linear (no limiter):
$$\beta_{\text{linear}}(r) = 1. \tag{6.8}$$

All simulations are conducted using the same configuration and numerical setup, with a spatial resolution of $\Delta x = 1\,[\mathrm{m}]$. The RMSE error is computed at $t = 500\,[\mathrm{s}]$ to quantify the deviation from the analytical reference solution. In addition to the absolute RMSE values, a relative error is computed by normalizing the RMSE by the L^2-norm of the analytical solution, defined as $\|C^{\text{ana}}\|_2 = \sqrt{\frac{1}{N}\sum_i (C_i^{\text{ana}})^2}$. This provides a dimensionless metric to assess the relative magnitude of the error, expressed as a percentage.

The resulting errors for each limiter are presented in Table 6.1, showing that the Minmod limiter gives the lowest error. This confirms that, the Minmod limiter offers the best compromise between suppressing non-physical oscillations and maintaining acceptable accuracy.

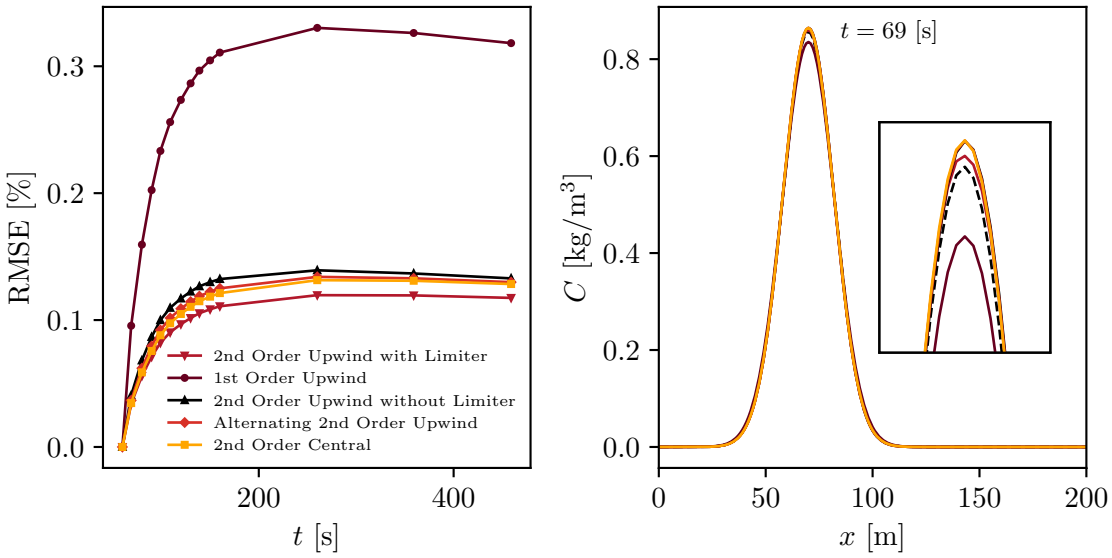

Figure 6.3: Left: RMSE between the numerical and analytical solutions over time for the five tested advection schemes. **Right**: Comparison of the numerical (coloured) and analytical (black dashed) concentration profiles along $y = 100$ [m] and $t = 69$ [s] with $\Delta x = 1$. The inset highlights the concentration peak resolution. The limited scheme with Minmod limiter provides the best compromise between numerical diffusion and stability.

To further motivate the choice of the scheme, Figure 6.3 compares the accuracy of the five tested advection schemes in terms of RMSE evolution over time (left panel) and profiles of the numerical vs analytical solution at $t = 69$ [s] (right panel). The plot confirms the improved agreement of the limited scheme with the analytical reference, especially in the region of the concentration peak. The inset on the right highlights the improved resolution of the Gaussian shape for the limited scheme compared to the more diffusive alternatives.

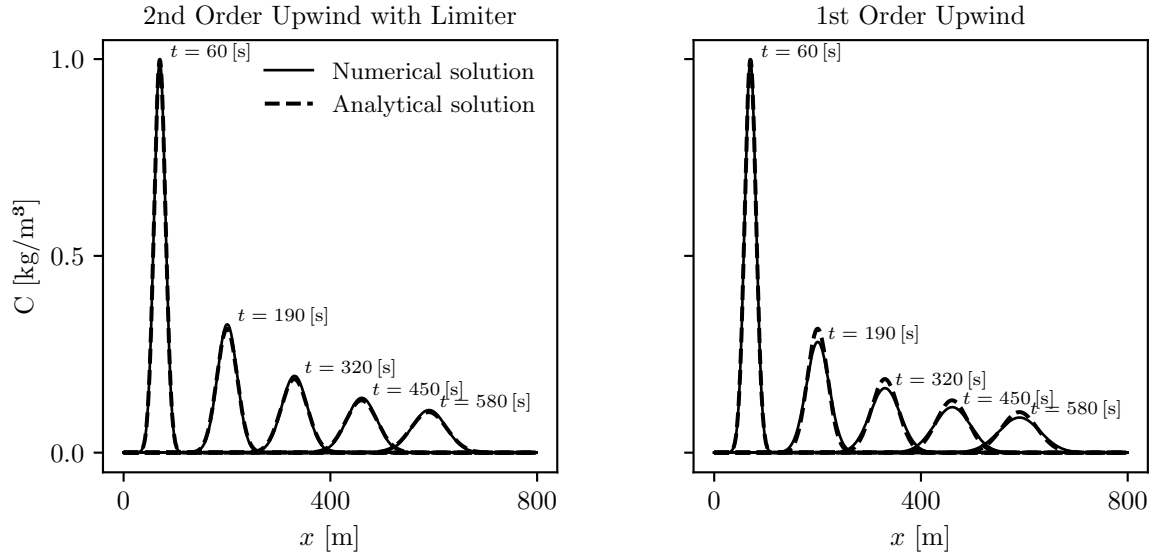

Figure 6.4: Concentration profile along x at $y = 100$ [m] and different times, using the corrected scheme with the Minmod limiter and $\Delta x = 2$ [m].

Finally, to visually assess the impact of the flux limiter correction, Figure 6.4 compares the numerical concentration profiles obtained using the classical first-order upwind scheme and the second-order upwind scheme corrected with the Minmod limiter. Both simulations are conducted with a resolution of $\Delta x = 2\,[\mathrm{m}]$, and the results are extracted at different times along the centreline $y = 100\,[\mathrm{m}]$. The corrected scheme provides a more accurate match with the analytical solution, exhibiting reduced numerical diffusion while avoiding oscillations. This confirms the effectiveness of the Minmod limiter in improving the solution quality for advection-dominated problems, while maintaining numerical stability.

To quantify the additional computational cost and accuracy improvement introduced by the flux limiter, simulations are performed for both the classical upwind and limited (Minmod) schemes at various spatial resolutions $\Delta x = 1, 2, 3, 4\,[\mathrm{m}]$. For each configuration, the total simulation time required to reach $t = 600\,[\mathrm{s}]$ is recorded, and the relative L^2 error with respect to the analytical Gaussian solution is computed.

Figure 6.5 presents a comparison between the simulation times and the numerical errors for both schemes. The left panel shows the computational time, which increases for finer resolutions, with the Minmod-limited scheme being significantly slower than the classical upwind scheme. On average, the limited scheme is found to be 3.45 times more expensive, due to the additional operations required to compute the non-linear flux correction at each time step.

The right panel illustrates the relative L^2 error, measured at $t = 500\,[\mathrm{s}]$, consistent with the analysis previously discussed in Figure 6.2, which compared all implemented advection schemes. Here, the focus is only on the upwind and Minmod schemes to highlight the accuracy vs. cost trade-off. These results confirm that the limited scheme achieves higher accuracy with mesh refinement, at the price of increased computational cost.

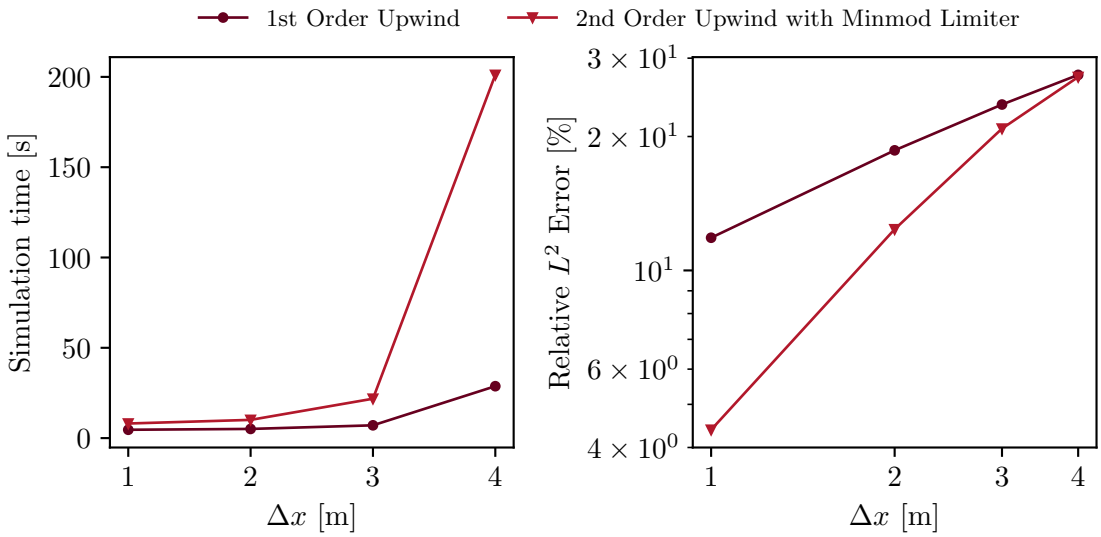

Figure 6.5: Comparison between the upwind and Minmod-limited schemes for different spatial resolutions Δx. **Left**: simulation time required to reach $t = 600\,[\mathrm{s}]$. **Right**: relative L^2 error with respect to the analytical solution.

6.2 Directional Advection Verification

To further verify the robustness of the implemented scheme, the same test configuration as in the previous validation case is reused. The computational grid, initial pollutant concentration, diffusion coefficients, and time discretization remain unchanged. The only modification lies in the velocity field, which is varied in direction. Specifically, the velocity field is varied in both x and y directions with $u = \pm 1$[m/s] and $v = \pm 1$[m/s], while keeping the diffusion anisotropic and the spatial resolution fixed at $\Delta x = \Delta y = 1$[m]. The corrected scheme using the Minmod flux limiter is used in all simulations.

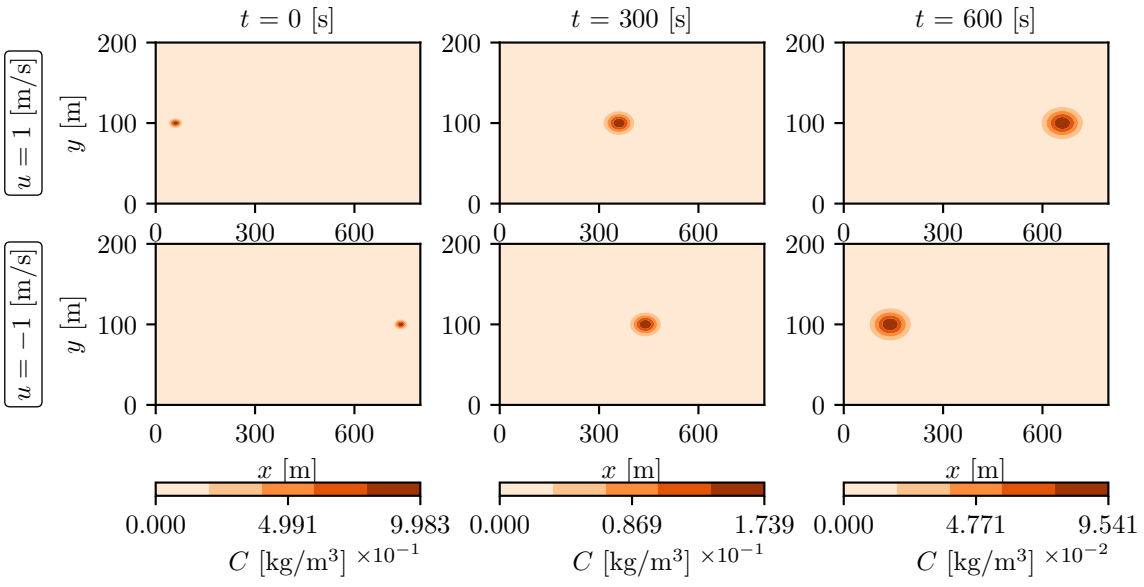

Figure 6.6: Time evolution of the solute cloud using the corrected scheme (Minmod limiter) with horizontal advection: $u = \pm 1$[m/s], $v = 0$ [m/s]. The concentration is shown at $t = 0$, 300 and 600 [s].

Figure 6.6 shows the evolution of the solute cloud for positive and negative advection in the x-direction ($u = \pm 1$[m/s]), at three different times. The initial condition is the same Gaussian-shaped pollutant used in the previous validation case. As expected, the concentration cloud is symmetrically advected along the x-axis depending on the sign of u.

Similarly, the vertical transport is assessed in Figure 6.7, with $v = \pm 1$[m/s] and $u = 0$ [m/s]. As expected, the pollutant moves in the vertical direction depending on the sign of v, while keeping the symmetric diffusion around the centre of the cloud. The simulation confirms the consistency and isotropy of the corrected scheme with respect to the advection direction.

To quantitatively assess the directional consistency of the scheme, the solution obtained for the case $u = 1$ [m/s], $v = 0$ [m/s] is rotated by 90 [°] and compared to the corresponding simulation with $v = 1$ [m/s], $u = 0$ [m/s]. The two concentration fields are evaluated at $t = 100$ [s], and the difference between them is analysed after transposition. A maximum absolute error of approximately 5.96×10^{-8} [kg/m^3] is observed. This discrepancy, although not at the

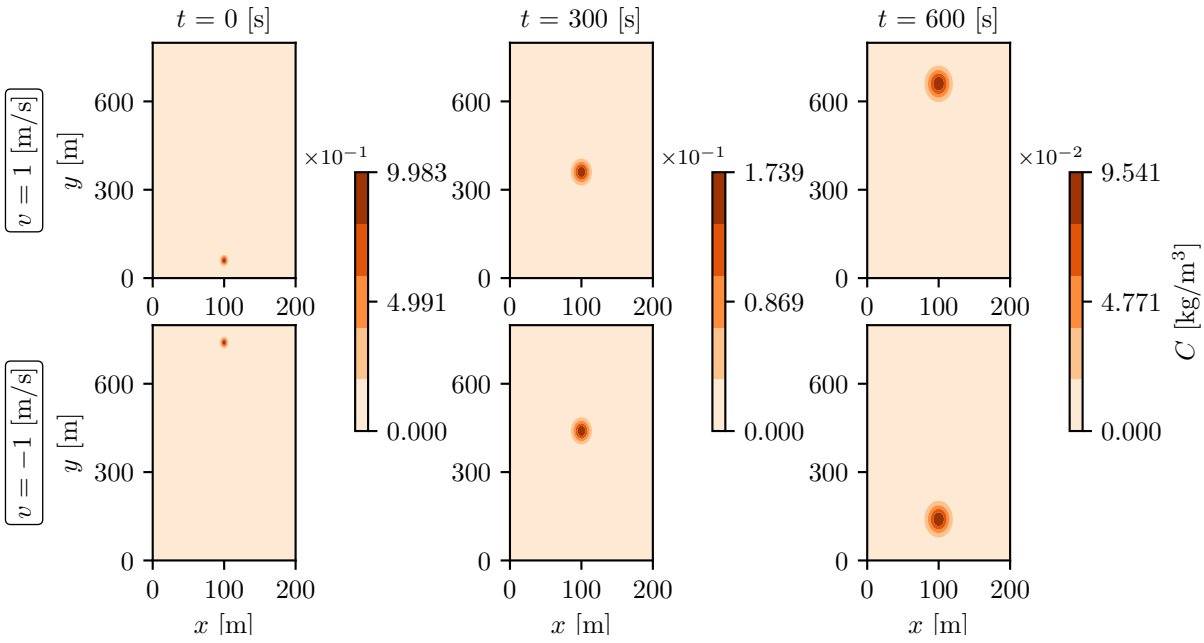

Figure 6.7: Time evolution of the solute cloud using the corrected scheme (Minmod limiter) with vertical advection: $v = \pm 1$[m/s], $u = 0$ [m/s]. The concentration is shown at $t = 0$, 300, and 600 [s].

level of machine precision, remains several orders of magnitude below the peak concentration values. It confirms that the numerical solver preserves directional symmetry with a high degree of accuracy.

6.3 Effect of Anisotropic Diffusion with Cross-terms

In order to validate the correct implementation of the anisotropic diffusion tensor, a set of simulations are performed in the absence of advection, focusing exclusively on the effect of diffusion, including cross-terms D_{xy} and D_{yx}. The goal is to assess whether the numerical model reproduces the expected physical behaviour in terms of spreading direction, symmetry, and orientation of the diffusion front.

The numerical simulation is carried out in a square domain of size $100 \times 100\,[\mathrm{m}^2]$, discretized using a uniform Cartesian grid with spatial resolution $\Delta x = \Delta y = 1\,[\mathrm{m}]$. The initial condition consists of a narrow Gaussian pulse centred at $(x_0, y_0) = (50, 50)$ [m], representing a localized injection. The total injected mass is controlled by a source discharge value of $Q_s = 1\,[\mathrm{m}^3/\mathrm{s}]$, an initial concentration of $C_s = 1\,[\mathrm{kg/m}^3]$, and the water depth is assumed constant at $h = 1\,[\mathrm{m}]$. The simulation is performed under purely diffusive conditions by imposing a zero velocity field. The total simulation time is set to $100\,[\mathrm{s}]$, with a time step automatically adapted based on Equation (5.57). The diffusion coefficients are varied across cases.

Figure 6.8 presents the evolution of the pollutant concentration at three different time steps, corresponding respectively to 10%, 50%, and 100% of the total simulation time. This allows a clear visualization of the transient diffusion behaviour from the early stages to the final transport. Each row corresponds to a different configuration of the diffusion tensor. The first

row illustrates the reference case of isotropic diffusion with $D_{xx} = D_{yy} = 1.0$ and $D_{xy} = 0.0$. The second and third rows correspond to anisotropic diffusion without cross-terms: first with $D_{xx} = 4.0$, $D_{yy} = 1.0$, and then with the axes swapped, *i.e.*, $D_{xx} = 1.0$, $D_{yy} = 4.0$. The last two rows represent anisotropic diffusion with non-zero cross-diffusion terms: $D_{xx} = D_{yy} = 1.0$ with $D_{xy} = -0.1$ and $D_{xy} = +0.1$, respectively.

The observed orientations and shapes of the isoconcentration contours can be justified mathematically by analysing the structure of the diffusion tensor $\mathbf{D}$. In the isotropic case, the diffusion tensor is a multiple of the identity matrix

$$D_{xx} = D_{yy} = 1.0, \quad D_{xy} = 0.0, \tag{6.9}$$

which leads to uniform diffusion in all directions. The resulting isoconcentration contours are circular and centred at the release location.

In the anisotropic configurations without cross-diffusion, the tensor remains diagonal but the components differ. For instance, when

$$D_{xx} = 4.0, \quad D_{yy} = 1.0, \tag{6.10}$$

the diffusion is enhanced along the x-axis, resulting in ellipsoidal spreading oriented horizontally. Conversely, if

$$D_{xx} = 1.0, \quad D_{yy} = 4.0, \tag{6.11}$$

the spread occurs more rapidly along the y-axis, producing vertical elongation of the contours.

When cross-diffusion terms are introduced, with

$$D_{xx} = D_{yy} = 1.0, \quad D_{xy} \neq 0.0, \tag{6.12}$$

the diffusion tensor becomes non-diagonal and must be diagonalized to identify the principal axes of diffusion as explained by Strang [1993]. Since the tensor is symmetric, it admits an orthonormal basis of eigenvectors. The diagonalization of the symmetric matrix $\mathbf{D}$ is given by

$$\mathbf{D} = \mathbf{Q}\,\boldsymbol{\Lambda}\,\mathbf{Q}^{\top}, \tag{6.13}$$

where $\boldsymbol{\Lambda}$ is the diagonal matrix of eigenvalues

$$\boldsymbol{\Lambda} = \begin{bmatrix} \lambda_1 & 0 \\ 0 & \lambda_2 \end{bmatrix}, \tag{6.14}$$

and the matrix $\mathbf{Q} \in \mathbb{R}^{2\times 2}$ is orthogonal (*i.e.*, $\mathbf{Q}^{\top} = \mathbf{Q}^{-1}$) and contains the eigenvectors of $\mathbf{D}$ as columns. In two dimensions, this matrix $\mathbf{Q}$ can be interpreted as a rotation matrix

$$\mathbf{Q} = \begin{bmatrix} \cos\theta & -\sin\theta \\ \sin\theta & \cos\theta \end{bmatrix}, \tag{6.15}$$

where θ is the angle between the Cartesian x-axis and the principal diffusion direction (*i.e.*, the direction of the first eigenvector).

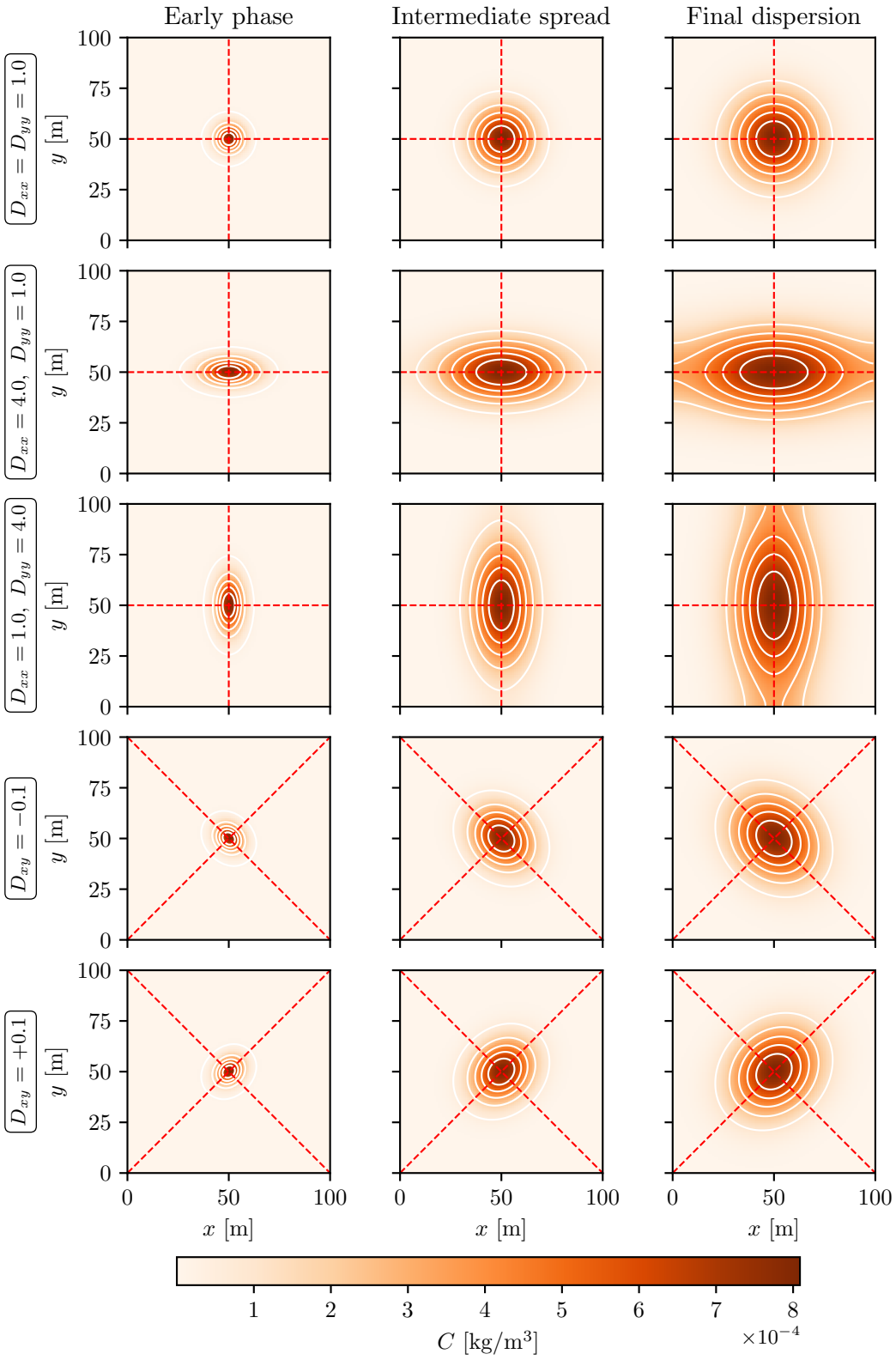

Figure 6.8: Concentration snapshots at three time steps for isotropic diffusion, anisotropic diffusion without cross-terms, and anisotropic diffusion with cross-terms.

To determine this angle θ, the condition that diagonalizes $\mathbf{D}$ is considered. Setting the off-diagonal elements of $\mathbf{Q}^\top \mathbf{D}\mathbf{Q}$ to zero leads to the classical identity

$$\tan(2\theta) = \frac{2D_{xy}}{D_{yy} - D_{xx}}, \tag{6.16}$$

which gives the orientation of the principal axes relative to the original Cartesian frame. In our specific case, since $D_{xx} = D_{yy}$, the denominator vanishes, yielding

$$\tan(2\theta) \to \pm\infty \quad \Rightarrow \quad 2\theta \to \pm\frac{\pi}{2} \quad \Rightarrow \quad \theta \to \pm\frac{\pi}{4}. \tag{6.17}$$

Thus, when $D_{xy} = +0.1$, the diffusion is preferentially oriented along the $+45°$ axis (northeast-southwest direction), whereas for $D_{xy} = -0.1$, it aligns with the $-45°$ axis (northwest-southeast direction). This theoretical analysis is consistent with the observed rotation and elongation of the pollutant concentration contours in Figure 6.8, and highlights the key role of the eigen-structure of the diffusion tensor in shaping anisotropic transport behaviour.

Chapter 7

Results and Discussion

This chapter presents and analyses the results obtained from the numerical simulations of pollutant transport in flooded urban environments. The simulations are based on the experimental configurations described in Chapter 4, and rely on the numerical framework introduced in Chapter 5.

The objectives of this chapter are fourfold. First, to assess the influence of the numerical discretization scheme on the accuracy and stability of the simulated concentration fields. Second, to investigate the role of anisotropic diffusion by varying the longitudinal and transverse coefficients of the diffusion tensor. Third, to analyse the impact of hydrodynamic variability by comparing steady and unsteady flow conditions on pollutant transport. Fourth, to validate the hydrodynamic fields used in both steady and unsteady configurations by comparing their capacity to reproduce key experimental features. Throughout the chapter, numerical results are compared to experimental data provided at INRAE, in particular those from the M.U.R.I. experimental platform described in Fagour [2025].

In all the simulations involving anisotropic diffusion, the formulation adopted for the longitudinal and transverse diffusion coefficients (D_L, D_T) is based on the theoretical framework presented in Section 3.2.2. This formulation is derived from the work Mignot et al. [2023], which relates the components of the diffusion tensor as explained in Figure 2.1.

7.1 Effect of the Numerical Scheme

Before investigating the influence of physical parameters such as anisotropic diffusion or hydrodynamic variability, it is interesting to evaluate how the choice of numerical discretization for the advection term affects the predicted pollutant concentration fields. The simulations presented in this section are based on the **C1** configuration introduced in Chapter 4 and shown in Figure 4.2. This configuration consists of two clear-water inlets and one pollutant injection point. It is characterized by moderate mixing and long residence time, as explained by Fagour [2025]. The velocity fields used in the advection-diffusion simulations are provided by the Wolf 2D shallow-water model [Erpicum et al., 2009], following the methodology detailed in Section 5.6.2.

All simulations are conducted over a total time of $T = 3000\,[\mathrm{s}]$, using time steps adapted to satisfy the CFL condition discussed in Section 5.3.1. The computational mesh and domain are consistent with the hydrodynamic model. An isotropic diffusion tensor is used throughout this

section, with

$$D_L = D_T = 1.6 \times 10^{-4}\,[\mathrm{m}^2/\mathrm{s}], \tag{7.1}$$

following the calibration proposed by Fontaine [2023].

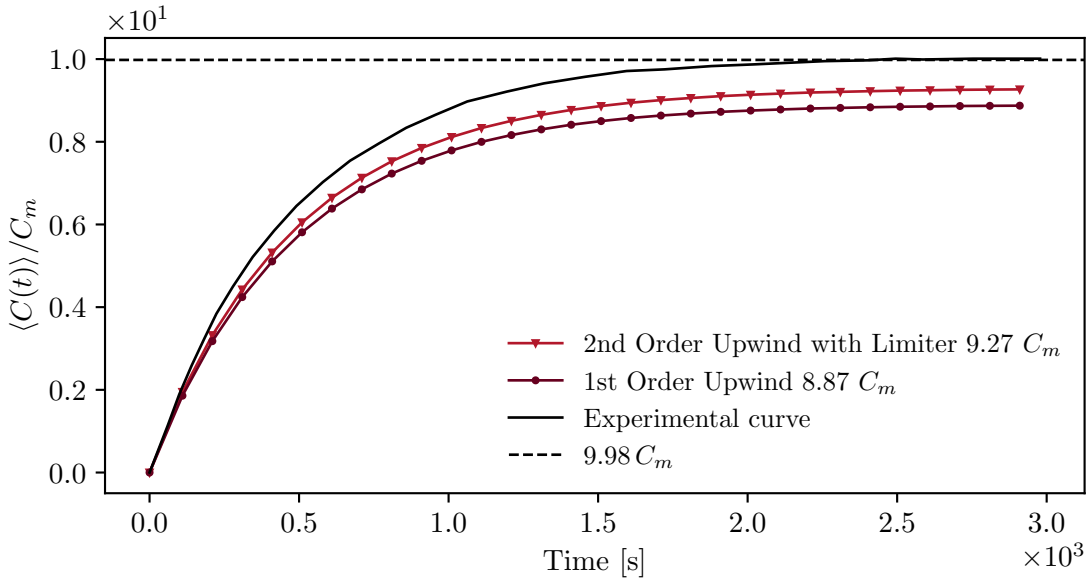

Figure 7.1: Time evolution of the normalized average concentration $\langle C(t)\rangle/C_m$ in the urban block (configuration **C1**) for two numerical schemes: the first-order upwind scheme and the second-order limited scheme with Minmod limiter. The dashed black line indicates the experimental plateau $9.98\,C_m$, while the black curve corresponds to experimental data. The final simulated values reach $9.27\,C_m$ with the limiter and $8.87\,C_m$ with the upwind scheme.

The pollutant is injected with a concentration $C_{\text{injection}} = 0.625\,[\mathrm{kg/m}^3]$ and a discharge $Q_{\text{injection}} = 35.5\,[\mathrm{L/h}]$. The perfectly mixed concentration C_m is defined, following Fagour [2025], as

$$C_m = \frac{C_{\text{injection}}\,Q_{\text{injection}}}{Q_{\text{injection}} + Q_{i1} + Q_{i2}}, \tag{7.2}$$

where $Q_{i1} + Q_{i2} = 6.5\,[\mathrm{L/s}]$ represents the total inflow from the clear-water channels.

According to the experimental results of Fagour [2024], the mean concentration measured in the urban block after reaching quasi-steady conditions is approximately

$$\langle C_s \rangle \approx 9.98\,C_m. \tag{7.3}$$

This value serves as a reference to assess the accuracy of the numerical predictions.

To support this analysis, Figure 7.1 provides a visual comparison of the pollutant transport dynamics obtained with the upwind and limiter schemes, in parallel with the experimental observations. It shows the temporal evolution of the normalized average concentration in the urban block. This figure is not intended to re-evaluate the choice of advection scheme already justified in Section 6.1 but rather to qualitatively visualize how the choice of numerical scheme affects both the rate and spatial extent of pollutant accumulation within the domain.

Although the differences observed between the numerical curves and the experimental data are partly attributable to numerical diffusion, particularly for the upwind scheme, they also reflect the complexity of pollutant transport through the urban geometry. In such a configuration, the pollutant follows intricate pathways shaped by street layouts, obstacles, and flow recirculation zones, making it difficult to attribute discrepancies to the numerical scheme alone. Nonetheless, this initial comparison provides a useful qualitative benchmark. It serves as a foundation for the next section, where the physical diffusion parameters D_L and D_T will be varied to evaluate their influence on the concentration dynamics and assess whether improved agreement with the experimental data can be achieved through parameter calibration.

7.2 Effect of Anisotropic Diffusion

This section aims to evaluate the impact of the anisotropic diffusion tensor on the predicted pollutant concentrations and to calibrate appropriate values for the longitudinal and transverse diffusion coefficients, D_L and D_T. The goal is to assess whether tuning these physical parameters can improve the agreement between the numerical predictions and experimental data in the urban configuration **C1** discussed in Section 7.1.

Given the high computational cost of the limited second-order scheme with Minmod limiter as explained in Figure 6.5, the parameter sweep is first conducted using the classical first-order upwind scheme. Although more diffusive, this scheme offers faster computations, enabling a broad exploration of the (D_L, D_T) space. It is assumed that the general trends observed, such as the location of the optimal region, will remain valid for the limiter scheme. This upwind based analysis thus serves as a computationally efficient first step to guide the calibration of the anisotropic diffusion tensor.

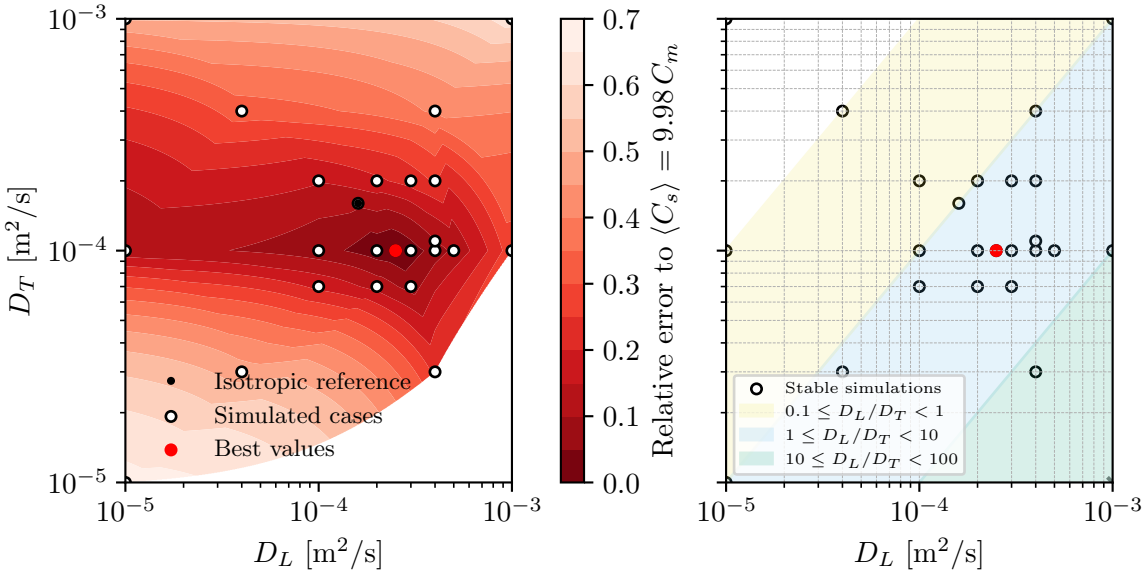

Figure 7.2: Comparison of simulation results in the (D_L, D_T) parameter space using the upwind advection scheme. **Left**: interpolated relative error [%] between the simulated and experimental concentrations. **Right**: stability map showing completed (white circles). Diagonal bands indicate anisotropy ratios D_L/D_T in logarithmic scale.

For each pair (D_L, D_T), an advection-diffusion simulation is carried out using the same unsteady hydrodynamic fields and pollutant injection parameters as defined in Section 7.1. The simulation runs until a final time of $t = 3000\,[\mathrm{s}]$, and the resulting concentration field is spatially averaged over the urban block. The mean concentration is then normalized by the theoretical perfectly mixed value C_m, and the relative error is computed with respect to the experimental reference plateau $\langle C_s \rangle = 9.98\, C_m$, as reported by Fagour [2025].

Figure 7.2 presents the results of the parametric study. The left panel shows an interpolated map of the relative error [%] between the simulated and experimental concentrations as a function of the diffusion coefficients. Each white circle represents a completed simulation, and darker colours indicate lower errors. The isotropic reference case ($D_L = D_T = 1.6 \times 10^{-4}\,[\mathrm{m}^2/\mathrm{s}]$) is marked, along with the configuration yielding the minimal error.

The right panel displays the same simulation set in the (D_L, D_T) space. Successful simulations are shown as white circles. Shaded diagonal bands highlight regions corresponding to different anisotropy regimes: yellow for $0.1 \leq D_L/D_T < 1$, blue for $1 \leq D_L/D_T < 10$, and green for $10 \leq D_L/D_T < 100$. These regions provide a visual guide to the nature of the anisotropy in each configuration.

The results confirm that the predicted concentration is sensitive to both diffusion coefficients. Among the simulated cases, the lowest relative error, approximately 0.52 [%], is obtained for

$$D_L = 2.5 \times 10^{-4}\,[\mathrm{m}^2/\mathrm{s}], \quad D_T = 1 \times 10^{-4}\,[\mathrm{m}^2/\mathrm{s}], \tag{7.4}$$

corresponding to an anisotropy ratio of $D_L/D_T = 2.5$.

To further assess the quality of the simulations under unsteady flow conditions, the time evolution of the numerically predicted concentration is compared against the experimental reference curve from the measurements reported by Fagour [2024]. Figure 7.1 presents the experimental dataset used for comparison with the numerical results. The comparison is made over the entire simulation duration using the Nash-Sutcliffe Efficiency (NSE) coefficient, an indicator for evaluating the accuracy of time-dependent numerical predictions [Permetrics, 2025].

The NSE is defined as

$$\mathrm{NSE} = 1 - \frac{\sum_{t=1}^{T} \left(C_{\mathrm{exp}}(t) - C_{\mathrm{num}}(t) \right)^2}{\sum_{t=1}^{T} \left(C_{\mathrm{exp}}(t) - \overline{C}_{\mathrm{exp}} \right)^2}, \tag{7.5}$$

where $C_{\mathrm{exp}}(t)$ and $C_{\mathrm{num}}(t)$ denote the experimental and numerical concentrations at time t, respectively, and $\overline{C}_{\mathrm{exp}}$ is the time-averaged experimental concentration. An NSE of 1 indicates a perfect match, while values greater than 0.5 generally reflect good predictive skill. Values between 0 and 0.5 indicate limited predictive ability, and negative values suggest that the model performs worse than simply using the mean of the observations.

The numerical simulations are carried out over a duration of 3000 [s]. Concentration outputs are stored every 10 [s]. For each combination of anisotropic diffusion coefficients (D_L, D_T), the simulated concentration time series is compared to the experimental time points, and the NSE is computed following Equation (7.5).

Figure 7.3 illustrates the quality of the time-evolving numerical predictions for configuration **C1** under unsteady conditions using the upwind advection scheme. Figure 7.3a compares the best simulated concentration curve with the experimental data, while Figure 7.3b shows a colour map of the NSE scores obtained for different combinations of longitudinal and transverse diffusion coefficients. This visualization highlights the parameter region leading to optimal agreement in terms of temporal evolution, thereby complementing the previous spatial error analysis.

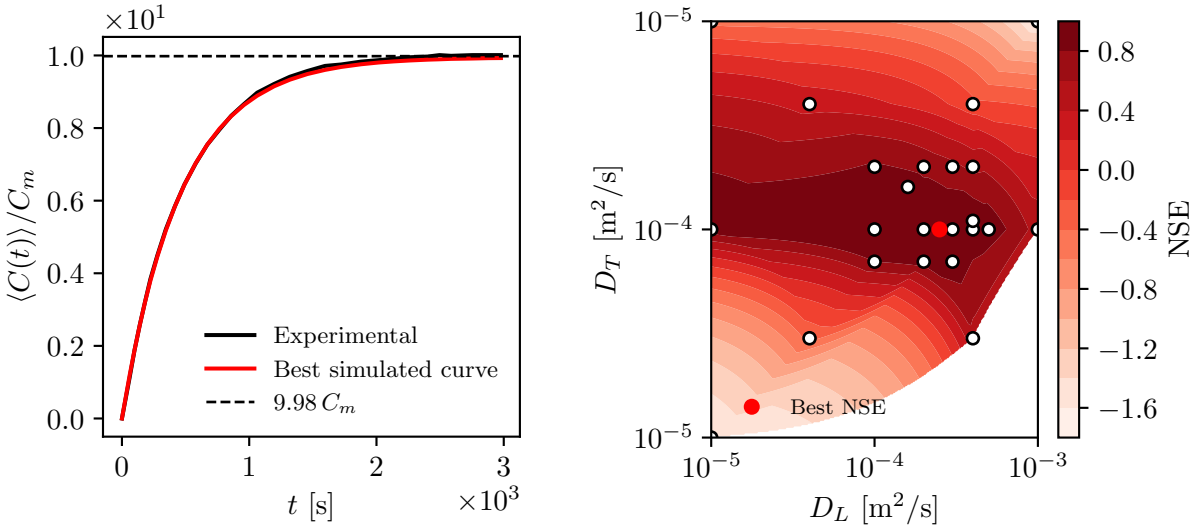

(a) Simulated vs experimental concentration curve.

(b) NSE scores over the (D_L, D_T) space.

Figure 7.3: Comparison between the numerical and experimental results for configuration **C1** under unsteady conditions with upwind advection scheme.

Several configurations achieve high NSE scores above 0.9, indicating good agreement with the experimental time series. However, when either D_L or D_T deviates significantly from the optimal range, particularly for overly large or overly small values, the model performance drops sharply, with NSE values falling below 0.5 or even becoming negative. These results confirm the importance of adequately tuning the diffusion tensor to realistically simulate pollutant dispersion in unsteady urban flood flows.

Interestingly, the best-performing configuration identified through this temporal analysis, namely $D_L = 2.5 \times 10^{-4}\,[\mathrm{m}^2/\mathrm{s}]$ and $D_T = 1.0 \times 10^{-4}\,[\mathrm{m}^2/\mathrm{s}]$, is consistent with the optimal point previously obtained in Equation (7.4). This pair yields an anisotropy ratio $D_L/D_T = 2.5$. This value lies within the range typically reported in the literature. For instance, Cheng [1984] and Lee & Seo [2007] suggest values around 10 for open-channel flows, while Lee & Kim [2012] and Alavian [1986] report ratios between 1 and 10 depending on flow conditions. The review by Mignot et al. [2023] further supports a range from 0.1 to 100 for urban and shallow water applications. The fact that the optimal ratio observed here falls within this established interval reinforces the credibility of the anisotropic diffusion model used in this study.

The results of this section provide a basis for refining the diffusion tensor under more accurate advection schemes. The next section investigates whether the improved limiter scheme,

combined with the diffusion values identified here, can reproduce the experimental reference with higher fidelity.

7.3 Anisotropic Diffusion Calibration

Following the identification of optimal diffusion coefficients D_L and D_T in the unsteady configuration **C1** using the upwind scheme at Equation (7.4), the next objective is to assess the robustness and generality of this calibration. The key idea is to verify whether the same anisotropic ratio D_L/D_T, or the same values, lead to similarly accurate results in other numerical conditions and experimental setups.

The initial analysis in Section 7.2 revealed that the minimal error is obtained for values of D_L and D_T lying within a specific region of the parameter space. It is now assumed that this region is relevant regardless of the numerical scheme or hydrodynamic mode used. Therefore, the goal of the present section is:

1. To test whether this optimal zone remains valid for other numerical conditions, particularly when using a second-order flux-limited advection scheme.
2. To determine whether these coefficients remain optimal under different flow regimes: *unsteady flow* and *steady flow* based on time-averaged hydrodynamics.

To perform this evaluation, simulations are conducted for a set of D_L and D_T values around the previously identified optimal region. These simulations are carried out for different configurations. To cover the various scenarios, four combinations of hydrodynamic conditions and configurations can theoretically be considered: each of the two urban layouts (**C0** and **C1**) can be simulated under either *steady* (time-averaged) or *unsteady* (fully transient) flow conditions. Among these four possible cases, three are included in this analysis as detailed in Table 7.1: configuration **C1** is tested under both steady and unsteady conditions, while configuration **C0** is examined under steady conditions only.

The unsteady simulation for **C0** is not included here, as this configuration exhibits a nearly time-invariant hydrodynamic regime in the Wolf 2D reference simulations. The velocity field in **C0** remains essentially steady throughout the transient simulation period. As a result, performing an additional unsteady simulation would not provide significant new insights and would be computationally redundant.

Configuration	**Steady flow**	**Unsteady flow**
C0	✓	—
C1	✓	✓

Table 7.1: Summary of the validation strategy. The diffusion calibration is tested across three of the four possible combinations of flow condition and configuration.

7.3.1 Calibration under Unsteady Flow Conditions

The objective of this section is not to reassess the entire parameter space, but rather to refine the search for the optimal anisotropic diffusion coefficients in the vicinity of the region previously identified using the upwind advection scheme. This strategy reduces computational cost

by focusing on a promising subset of parameters. The analysis is now carried out under unsteady flow conditions for configuration **C1**, using the more accurate second-order flux-limited scheme with the Minmod limiter, in order to find the minimum error location with higher numerical precision.

The analysis follows the same methodology as in Section 7.2, where a sweep of the anisotropic diffusion tensor is performed. Here, the focus is on the parameter sweep around the previously identified optimal region, corresponding to longitudinal and transverse coefficients on the order of 10^{-4} as detailed in Equation (7.4).

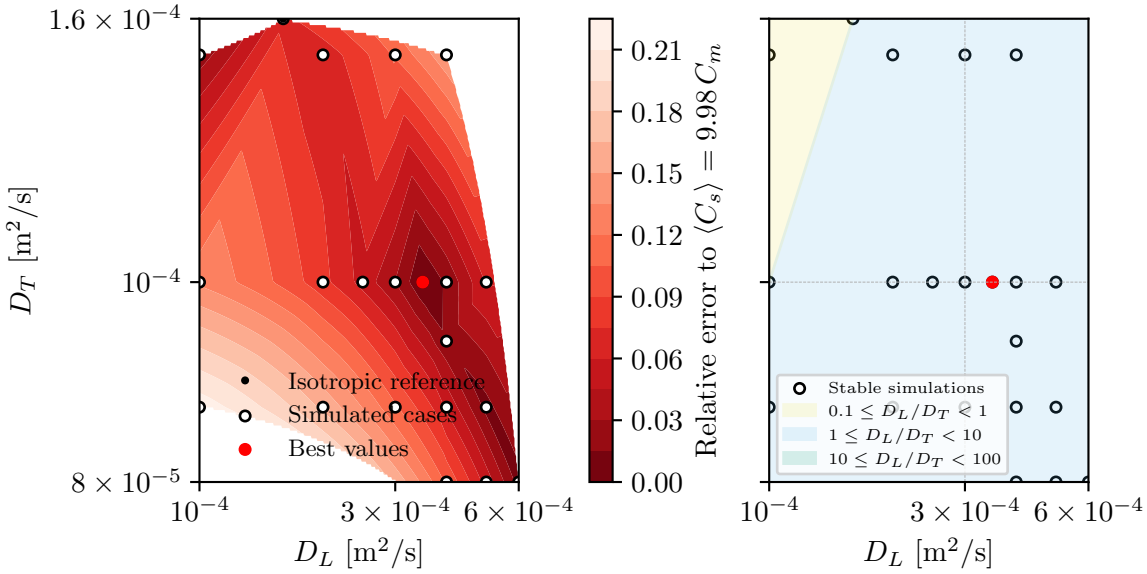

Figure 7.4: Left: Map of the relative concentration error [%] as a function of longitudinal and transverse diffusion coefficients D_L and D_T, respectively, for configuration **C1** under unsteady flow. The results are obtained using the second-order flux-limited scheme. The darker region indicates lower error and identifies the optimal anisotropic diffusion configuration. **Right**: Stability map showing completed (white circles) simulations. Diagonal bands indicate anisotropy ratios D_L/D_T in logarithmic scale.

Figure 7.4 presents the spatial distribution of the relative concentration error obtained for each combination of D_L and D_T under unsteady flow conditions using the flux-limited scheme. The results confirm the existence of a minimum error within the same anisotropy region as previously identified. The lowest error is achieved for

$$D_L = 3.5 \times 10^{-4}\,[\mathrm{m}^2/\mathrm{s}] \quad \text{and} \quad D_T = 1.0 \times 10^{-4}\,[\mathrm{m}^2/\mathrm{s}], \tag{7.6}$$

corresponding to an anisotropy ratio $D_L/D_T = 3.5$, and yielding a relative deviation from the reference concentration of approximately 0.01 [%]. This value is consistent with the optimal ratio previously identified using the first order upwind scheme. Although the precise values may vary slightly due to the increased accuracy of the limiter approach, the overall optimal region remains unchanged. This reinforces the robustness of the anisotropic calibration procedure across different numerical schemes.

For each combination of anisotropic diffusion coefficients (D_L, D_T), the simulated concentration time series is compared to the experimental data, and the NSE is computed according to

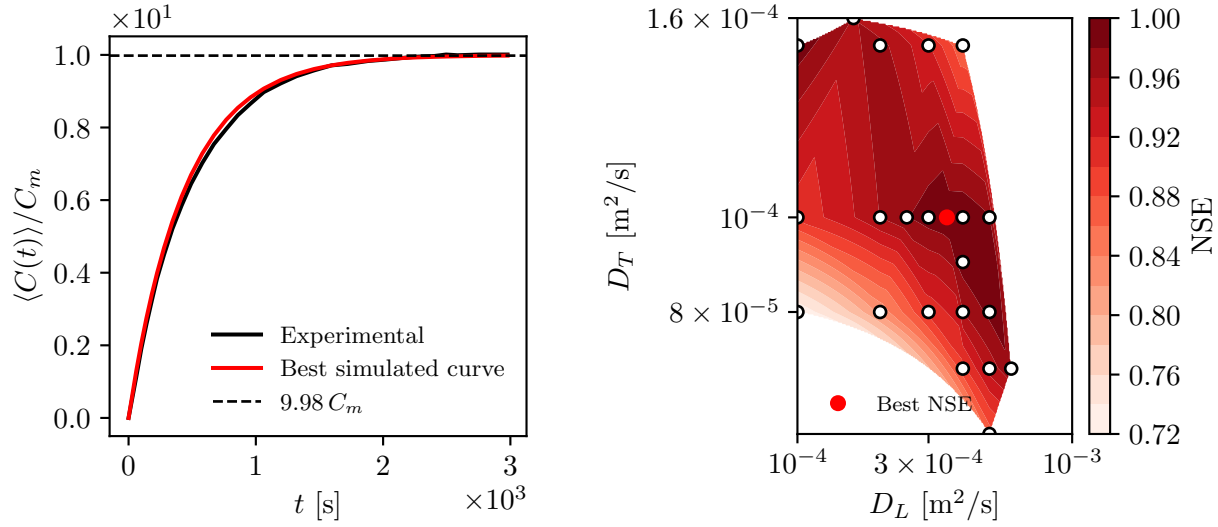

(a) Simulated vs experimental concentration curve.

(b) NSE scores over the (D_L, D_T) space.

Figure 7.5: Comparison between the numerical and experimental results for configuration **C1** under unsteady conditions using the flux-limited second order scheme.

Equation (7.5). The resulting scores help identify the best-performing configurations in terms of temporal agreement with the observed concentration. Figure 7.5 presents the results obtained under unsteady flow conditions using the flux-limited scheme. Figure 7.5a shows the best simulated curve compared to the experiment. Figure 7.5b displays a heatmap of NSE values across the (D_L, D_T) parameter space.

Notably, the highest NSE score is obtained for the same diffusion coefficients identified previously via the convergence error analysis in Equation (7.6) confirming the consistency between both evaluation criteria. This reinforces the robustness of the anisotropic calibration, as both spatial and temporal performance metrics converge toward the same optimal configuration.

Interestingly, the optimal anisotropy ratio of $D_L/D_T = 3.5$ obtained using the second-order limited scheme is slightly higher than the one previously identified using the first-order upwind method in Equation (7.4). This discrepancy is expected and can be attributed to the higher level of numerical diffusion inherently present in the upwind scheme. In that case, part of the physical transport is artificially compensated by the scheme numerical diffusion, leading to an underestimated need for longitudinal diffusion. In contrast, the flux-limited scheme reduces numerical diffusion, thereby requiring a more realistic and higher value of D_L to accurately model the anisotropic transport.

It is possible to examine the spatial and temporal evolution of the pollutant plume under unsteady conditions. Figure 7.6 illustrates the normalized concentration field and associated velocity vectors at various times during the simulation, using the calibrated anisotropic diffusion coefficients $D_L = 3.5 \times 10^{-4}\,[\mathrm{m}^2/\mathrm{s}]$ and $D_T = 1.0 \times 10^{-4}\,[\mathrm{m}^2/\mathrm{s}]$. The snapshots reveal how the pollutant is progressively transported and diffused throughout the urban layout.

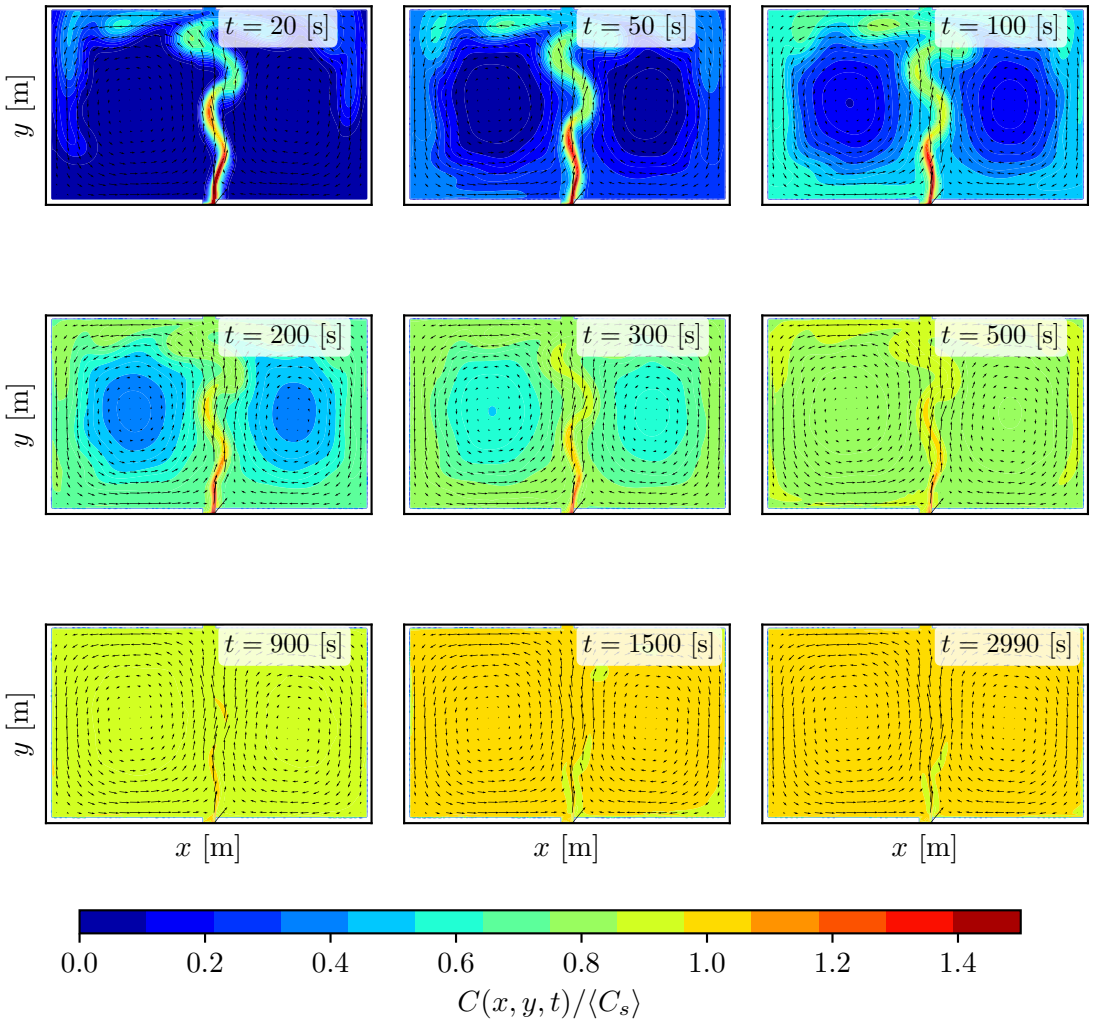

Figure 7.6: Spatio-temporal evolution of the pollutant plume in configuration **C1** under unsteady flow conditions. Each panel shows the normalized concentration field $C/\langle C_s \rangle$ at time t, with local flow velocity vectors overlaid as black arrows. The arrow lengths indicate the relative magnitude of the velocity field, and highlight the preferential transport directions. The simulation uses the optimal anisotropic diffusion coefficients $D_L = 3.5 \times 10^{-4}\,[\mathrm{m}^2/\mathrm{s}]$ and $D_T = 1.0 \times 10^{-4}\,[\mathrm{m}^2/\mathrm{s}]$.

All simulated concentration fields are normalized by the average inflow concentration $\langle C_s \rangle$ to allow consistent comparisons across different configurations. This choice reflects the assumption that the inflow concentration corresponds to the established steady-state value of the pollutant at the inlet. Such an assumption is physically justified and experimentally verified in Fagour [2025], where the following relation is confirmed

$$\langle C_s \rangle = \frac{\sum_i Q_i C_i}{Q_{\mathrm{tot}}}, \tag{7.7}$$

where Q_i and C_i respectively denote the volumetric inflow rate and pollutant concentration at inlet i, and $Q_{\mathrm{tot}} = \sum_i Q_i$ is the total inflow discharge, such that $\langle C_s \rangle$ represents the discharge-weighted average concentration at the domain entry.

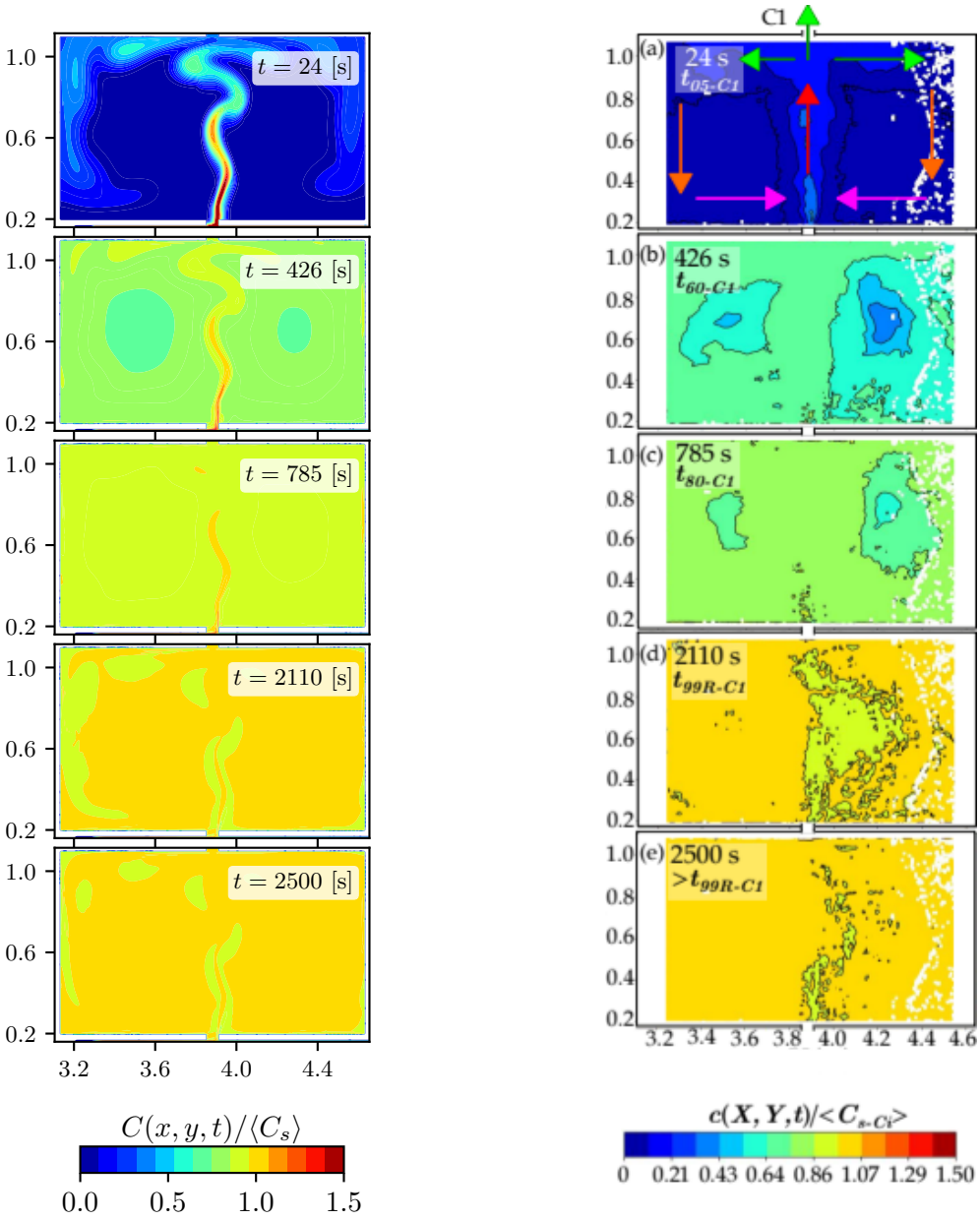

(a) Simulated pollutant concentration field ($C\langle C_s\rangle$) using the best anisotropic diffusion coefficients ($D_L = 3.5\times10^{-4}, D_T = 1.0\times10^{-4}$).

(b) Experimental concentration field for configuration **C1**.

Figure 7.7: Visual comparison between the simulated and experimental pollutant concentration fields for configuration **C1** under unsteady flow conditions.

Beyond the overall transport dynamics, specific flow structures can be identified in the concentration and velocity fields. In particular, zones of recirculation emerge clearly in several snapshots of Figure 7.6. These regions, typically located behind obstacles and along the lateral cavities of the domain, are characterized by low-magnitude velocity vectors forming closed or circular patterns.

Interestingly, the pollutant plume appears to initially bypass these recirculation zones, remaining mostly confined to the main advective paths during the early stages of the simulation. This behaviour is physically consistent with the experimental observations reported by Fagour [2025]. As the simulation progresses, the distinction between advective pathways and recirculation zones becomes less pronounced. The pollutant gradually diffuses into the side cavities, leading to a more homogenized concentration field over time. This temporal smoothing is visible in the later frames of Figure 7.6, where the pollutant distribution becomes less contrasted and the influence of initial recirculation structures diminishes.

Figure 7.7 provides a side-by-side comparison of the simulated and experimental concentration fields for configuration **C1**. Both maps exhibit consistent spatial patterns, with peak concentrations observed in similar regions. This qualitative agreement reinforces the validity of the anisotropic parameter calibration and confirms that the model successfully captures the dominant transport dynamics observed in the experiment.

7.3.2 Calibration under Steady Flow Conditions

As introduced in Table 7.1, this section focuses on the simulation of pollutant transport under steady hydrodynamic conditions. The velocity fields used in the simulations are obtained by time-averaging the outputs of the Wolf 2D model, as described in Section 5.6.1. This approach allows us to simplify the hydrodynamic forcing while preserving the main spatial structures of the flow.

The goal is twofold: first, to assess whether a steady representation of the flow can reasonably reproduce the observed pollutant dynamics in urban configurations; and second, to determine the optimal set of anisotropic diffusion coefficients (D_L, D_T) that best match experimental measurements under these simplified hydrodynamic conditions. Two configurations are considered in this context: configuration **C0**, which is inherently steady, and configuration **C1**, which is originally unsteady but here approximated using a time-averaged velocity field.

Configuration C0

The objective of this section is to validate the numerical simulation under steady hydrodynamic conditions (configuration **C0**) by comparing the model results to the experimental measurements described in Chapter 4. Specifically, the comparison focuses on the mass discharge of pollutant across key sections of the domain.

The experimental study conducted on the M.U.R.I. platform provides detailed measurements of pollutant concentrations and flow rates at five internal cross-sections within the urban geometry, as well as at the four outlet boundaries of the domain. These measurement locations are illustrated in Figure 4.3. For each of these nine locations (S_1, S_2, S_3, S_4, S_5, and the four outlets O_1, O_2, O_3, O_4), the experimental discharge of pollutant is obtained by multiplying the measured velocity and concentration profiles. The corresponding numerical discharges are computed from the steady-state concentration field extracted at the end of the simulation, using the time-averaged hydrodynamic field. In this configuration, the pollutant is continuously injected at the upstream-left location, denoted as cu in the experimental setup (see Figure 4.3).

Before comparing simulated concentrations to experimental discharge measurements, it is essential to ensure that the pollutant transport simulation has reached a quasi-steady state. In

the case of configuration **C0**, where the hydrodynamic field is steady (time-averaged), the simulation is run over a sufficiently long period to allow the pollutant to fully propagate through the domain and reach the outlet zones.

To justify the choice of simulation time, the concentration is monitored at all outlets throughout the simulation. In particular, both the individual concentrations $C_{\text{outlet},k}(t)$ at each outlet $k = 1,\dots,4$, and the overall mean outlet concentration $C_{\text{mix, outlet}}(t)$, defined as

$$C_{\text{mix, outlet}}(t) = \frac{1}{N_{\text{out}}} \sum_{(i,j)\in\text{outlets}} C_{i,j}(t), \tag{7.8}$$

are tracked over time to evaluate convergence.

Figure 7.8 displays the time evolution of these outlet concentrations under steady hydrodynamic conditions. Each coloured curve corresponds to one outlet, while the dashed black line shows the mean outlet concentration. A plateau is reached for all outlet curves after approximately $t = 120\,[\text{s}]$, indicating that the system has reached a quasi-steady state. Convergence is considered achieved when the temporal variation of the mean outlet concentration becomes lower than 1 [%] over a defined time window.

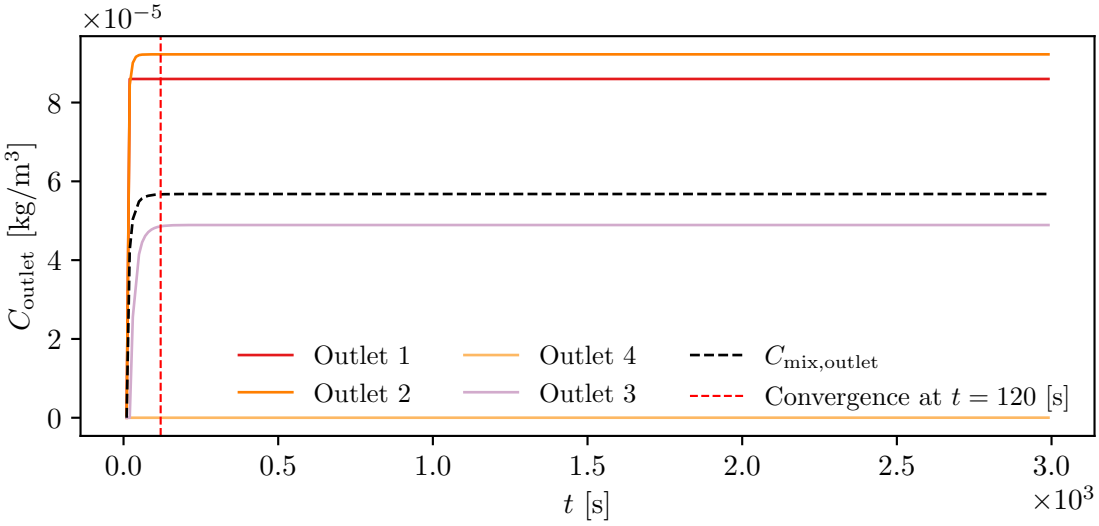

Figure 7.8: Time evolution of the outlet concentrations $C_{\text{outlet},k}(t)$ for configuration **C0** under steady hydrodynamic conditions. The mean outlet concentration $C_{\text{mix,outlet}}$ is shown as a dashed black line. A quasi-steady state is reached after approximately 120 [s].

Based on this analysis, a final simulation time of $T = 150\,[\text{s}]$ is selected to ensure that the pollutant transport has stabilized before performing any comparison with experimental measurements. Monitoring all outlet segments individually also provides insight into the temporal dynamics and potential spatial variability of pollutant release at the domain boundary.

After justifying the total simulation time required to reach a quasi-steady state, the methodology proceeds with the calibration of the anisotropic diffusion tensor under steady hydrodynamic conditions. The longitudinal and transverse diffusion coefficients D_L and D_T are varied

across a range of values consistent with the anisotropy ratios previously investigated in the unsteady case.

For each pair (D_L, D_T), a simulation is conducted using the time-averaged velocity field corresponding to configuration **C0**. Once the simulation reaches $T = 150\,[\mathrm{s}]$, the resulting concentration field is post-processed to compute the pollutant mass discharges across the five internal cross-sections and the four outlet segments.

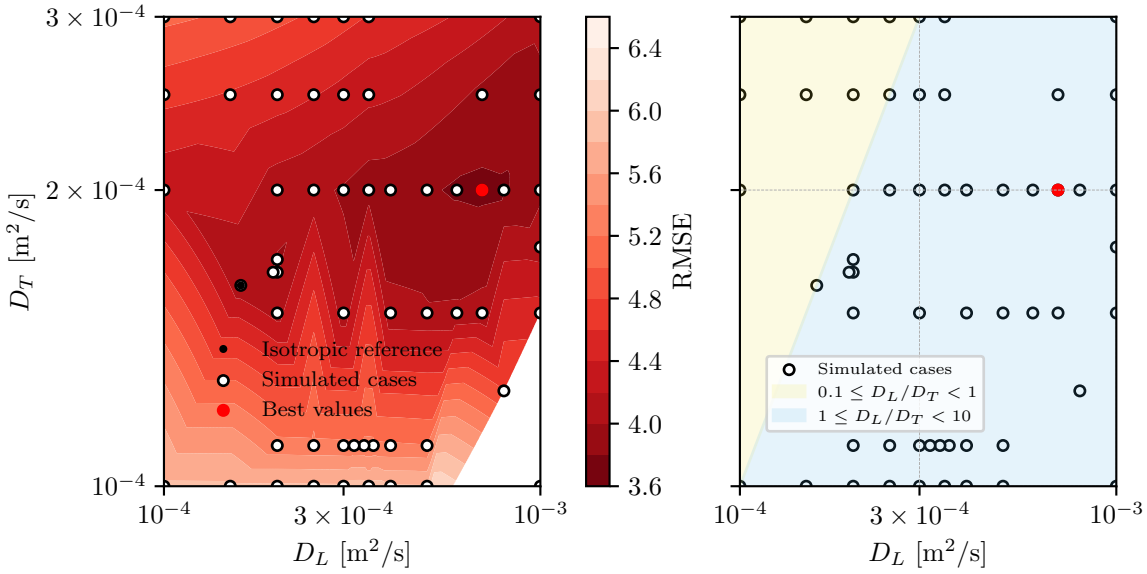

Figure 7.9: Left: Interpolated RMSE map for configuration **C0** under steady hydrodynamic conditions. Each point corresponds to a tested pair (D_L, D_T), with the colour indicating the RMSE compared to experimental discharges. The red dot marks the best-performing configuration, and the black dot denotes the isotropic reference. **Right**: Distribution of tested configurations across anisotropy ratio regimes.

To quantitatively evaluate the match between simulated and experimental discharges, a RMSE is computed across the nine available measurement sections. For each location, the simulated mass discharge is expressed as a percentage of the total incoming pollutant flux. The RMSE is then defined as follows

$$\mathrm{RMSE} = \sqrt{\frac{1}{N}\sum_{k=1}^{N}\left(Q_{m,\mathrm{sim}}^{(k)} - Q_{m,\mathrm{exp}}^{(k)}\right)^2}, \tag{7.9}$$

where $N = 9$ is the number of measurement sections, $Q_{m,\mathrm{sim}}^{(k)}$ and $Q_{m,\mathrm{exp}}^{(k)}$ are respectively the simulated and experimental pollutant mass discharges at section k, both expressed in percentage of the total inflow discharge.

Using this metric, a sweep is performed by varying the longitudinal and transverse diffusion coefficients D_L and D_T. For each pair, the RMSE is computed and plotted over a logarithmic parameter space. Figure 7.9 shows the resulting RMSE map, interpolated over the tested configurations.

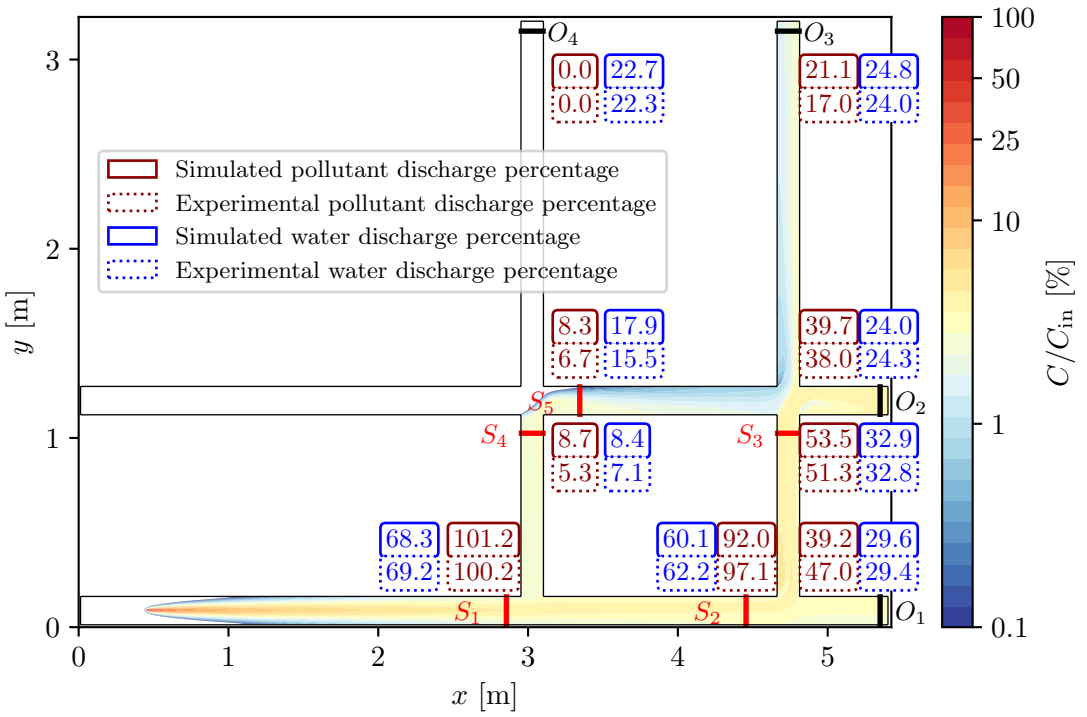

Figure 7.10: Final pollutant concentration field normalized by the injection value ($C/C_{\text{in}} \times 100$) for configuration **C0**, under steady hydrodynamic conditions using the optimal diffusion coefficients $D_L = 7.0 \times 10^{-4}[\text{m}^2/\text{s}]$ and $D_T = 2 \times 10^{-4}[\text{m}^2/\text{s}]$. Red labels indicate the simulated (solid) and experimental (dashed) pollutant mass discharge percentages. Blue labels show the corresponding water discharge percentages.

The optimal values for **C0** under steady flow conditions are found to be

$$D_L = 7.0 \times 10^{-4}\,[\text{m}^2/\text{s}], \quad D_T = 2.0 \times 10^{-4}\,[\text{m}^2/\text{s}], \tag{7.10}$$

yielding a RMSE of approximately 3.8 [%] across the nine measurement sections. This corresponds to an anisotropy ratio of $D_L/D_T = 3.5$ which falls within the same intermediate anisotropy class ($1 \leq D_L/D_T < 10$) identified in the previous unsteady configuration analysis. This further supports the idea that, regardless of the flow regime, an anisotropic diffusion model with a moderate longitudinal-to-transverse ratio provides consistent and robust results across different transport scenarios.

To conclude this analysis, Figures 7.10 and 7.11 provide a visual summary of the pollutant transport and discharge results for the best-performing diffusion configuration identified under steady flow conditions. Figure 7.10 shows the final pollutant concentration field, normalized by the inlet value, along with simulated and experimental discharge percentages for both water (in blue) and pollutant (in red) at each outlet and section. Figure 7.11 complements this view by presenting the absolute errors, in percentage points, between the simulated and measured pollutant discharges, thus quantifying the local discrepancies across the domain.

Overall, the absolute errors between simulated and experimental pollutant discharges remain reasonably low, with most values falling below 5 [%]. The highest discrepancy, observed

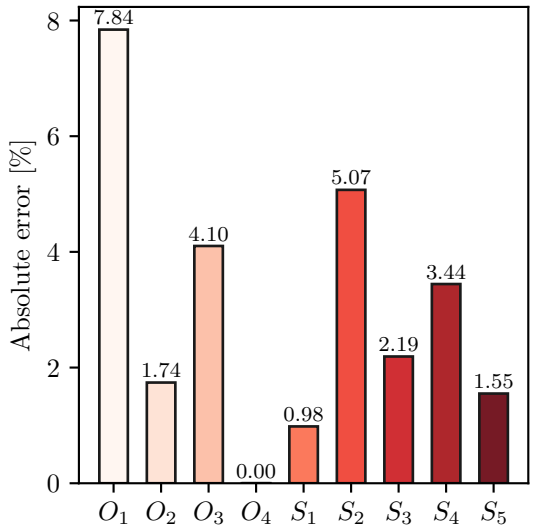

Figure 7.11: Absolute error (in percentage points) between simulated and experimental pollutant discharges at each outlet and section for the best-performing diffusion pair $D_L = 7.0 \times 10^{-4}[\mathrm{m}^2/\mathrm{s}]$, $D_T = 2.0 \times 10^{-4}[\mathrm{m}^2/\mathrm{s}]$.

at outlet O_1, reaches 7.84 [%], while several other sections show errors under 2 [%]. Such a level of agreement confirms the ability of the model to reproduce the spatial distribution of pollutant transport with good accuracy under steady-state hydrodynamic conditions.

Configuration C1

In this section, the objective is to evaluate whether the pollutant dynamics observed in configuration **C1** under unsteady flow conditions can be reasonably reproduced using a simplified steady representation of the hydrodynamics. To isolate the effect of the velocity field while avoiding additional complexity related to diffusion calibration, the simulations are performed using a basic isotropic diffusion tensor, defined as, $D_L = D_T = 1.6 \times 10^{-4}\,[\mathrm{m}^2/\mathrm{s}]$ which corresponds to the reference value previously used in Section 7.1.

A time-averaged velocity field is extracted from the Wolf 2D simulation of configuration **C1** and used as a stationary input to the advection-diffusion model. A simulation is then performed over a total duration of 3000 [s], consistent with the unsteady case, in order to observe how the pollutant spreads and gradually homogenizes within the domain. The resulting transport patterns are compared to those obtained under fully unsteady hydrodynamic conditions, using the same isotropic diffusion coefficients.

Figure 7.12 shows the evolution of the pollutant plume using the time-averaged velocity field. While the pollutant is gradually transported and accumulates within the domain, the resulting concentration field appears significantly smoother and more symmetric than in the unsteady case. The complex temporal structures induced by velocity oscillations are entirely absent. As a result, the plume evolution lacks the fluctuating behaviour observed under unsteady flow conditions. Moreover, the pollutant does not fully homogenize within the domain, indicating that certain mixing mechanisms associated with transient hydrodynamics are not captured in this steady approximation.

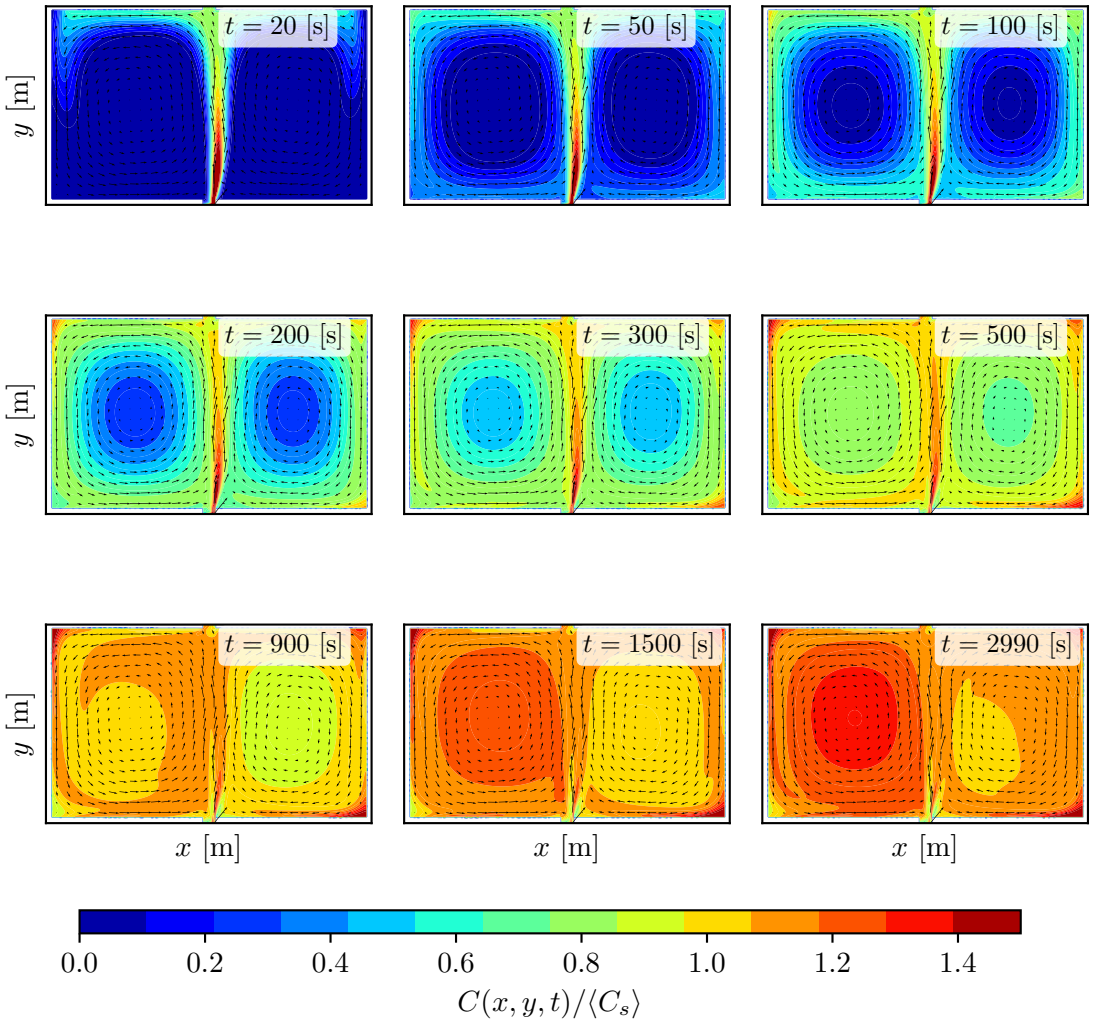

Figure 7.12: Spatio-temporal evolution of the pollutant concentration in configuration **C1** under steady hydrodynamic conditions. The velocity field used is the time-averaged result from the unsteady Wolf 2D simulation. The concentration is normalized by the reference plateau value $\langle C_s \rangle$, and local flow vectors are overlaid.

As shown in Figure 7.13, the simulation using a time-averaged (steady) velocity field fails to reproduce key transport dynamics observed under unsteady conditions. First, the concentration field in the steady case evolves without any temporal oscillations, in contrast to the unsteady simulation where the plume exhibits visible fluctuations and asymmetries over time. Second, the pollutant spreads more rapidly in the steady case, reaching a broad coverage of the domain much earlier. However, this faster propagation does not lead to a homogeneous distribution; instead, the steady simulation yields a final concentration field that is both uneven and significantly overestimated in magnitude. In contrast, the unsteady simulation produces more realistic concentration levels and spatial structures, closely matching the experimental observations. These differences highlight that the steady approximation not only fails to capture transient effects, but also misrepresents the overall mixing and accumulation process within the domain.

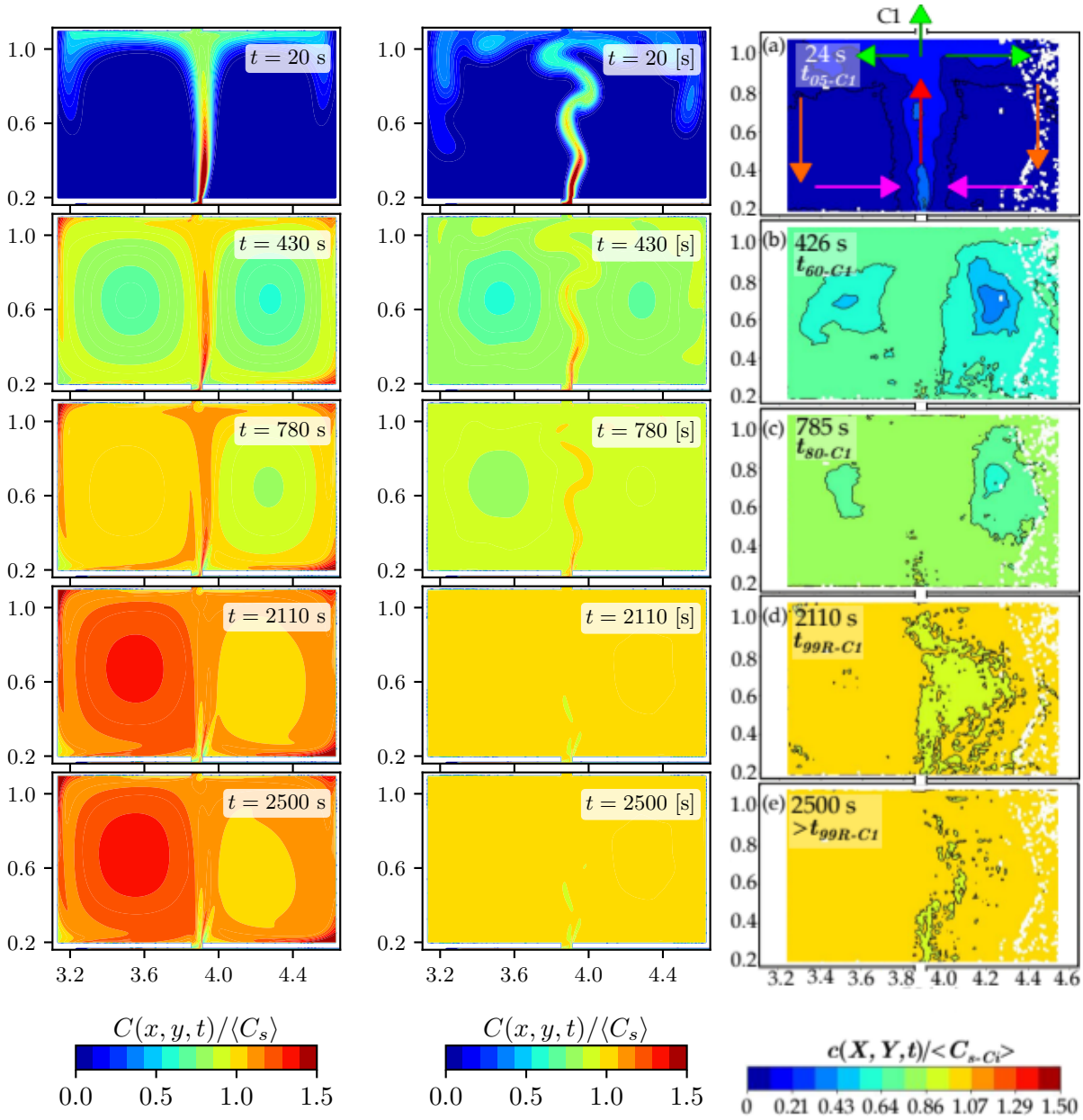

(a) C1 steady: isotropic, time-averaged velocity.

(b) C1 unsteady: isotropic, time-resolved velocity.

(c) C1: Experimental concentration field.

Figure 7.13: Comparison of final pollutant concentration fields in configuration **C1**. All numerical simulations use the same isotropic diffusion coefficients. **Left**: simulation with steady, time-averaged velocity field. **Middle**: simulation with unsteady, time-resolved velocity. **Right**: experimental reference map.

To further support this observation, Figure 7.14 presents the time evolution of the average pollutant concentration in the block for the steady simulation. The numerical result is compared to the experimental dataset as well as the reference plateau concentration $9.98\,C_m$. While the simulation follows a similar initial trend, the early-phase dynamics are not perfectly aligned with the experimental curve, and the growth rate is slightly underestimated from the beginning. More importantly, the simulation continues to rise after $t = 3000\,[\mathrm{s}]$, suggesting that

convergence has not been fully achieved by the end of the simulation. This is consistent with the spatial distribution observed in the final concentration maps, where the steady simulation still exhibits localized high concentrations and lacks the homogenization seen in the unsteady and experimental cases. These discrepancies confirm that the absence of temporal fluctuations in the velocity field leads to an overly efficient and unrealistic accumulation of pollutant.

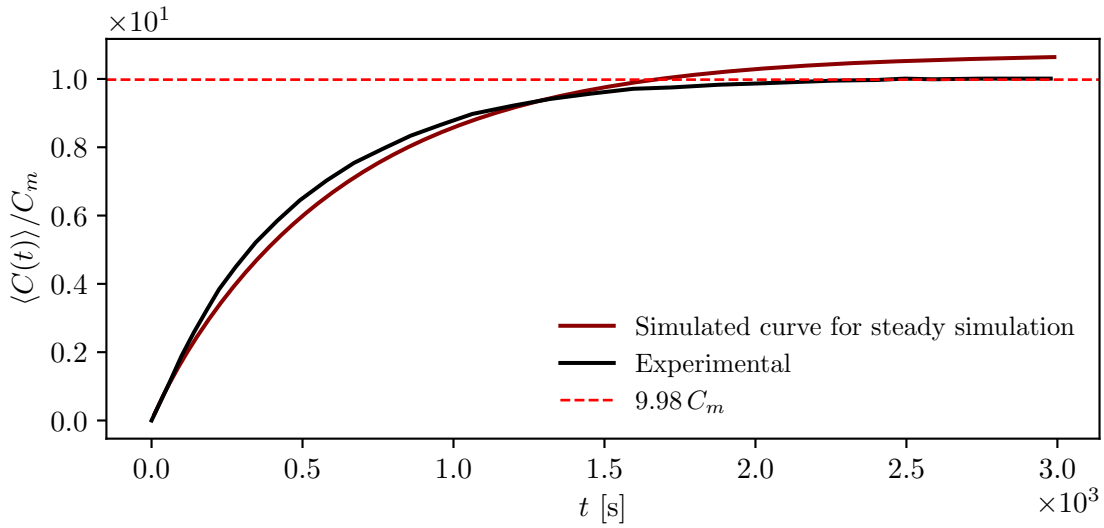

Figure 7.14: Time evolution of the normalized average concentration in the block for configuration **C1** under steady flow conditions. The numerical result (red curve) is obtained using the limiter scheme and isotropic diffusion. The black curve shows the experimental reference, and the dashed red line indicates the expected plateau value $9.98\,C_m$.

To mitigate the limitations of steady-state simulations in capturing transient flow structures, one possible approach is to adjust the diffusion tensor through calibration. In particular, increasing the transverse diffusion coefficient D_T can enhance lateral spreading of the pollutant, thereby reducing the over-concentration observed along the primary transport direction. This calibration acts as a numerical compensation for the absence of transient recirculation zones, which are naturally captured in unsteady simulations. However, it constitutes an artificial correction rather than a physically grounded representation, and should therefore be considered as a limitation of the steady approximation.

7.3.3 Synthesis and Discussion

This section addressed two key questions regarding the calibration of anisotropic diffusion models. First, it examined whether the optimal diffusion coefficients D_L and D_T, initially identified in the unsteady configuration **C1** using a first-order upwind scheme, remain valid when applied across different numerical discretizations and flow regimes. Second, it assessed the relevance of using time-averaged hydrodynamic fields instead of fully unsteady flows, particularly for configuration **C1**.

Regarding the first objective, the results demonstrate that the previously identified optimal region in the (D_L, D_T) parameter space remains consistent when employing a higher-order flux-limited advection scheme. Furthermore, the same anisotropic regime leads to accurate results

in configuration **C0** under steady-state flow conditions. These findings confirm the robustness and transferability of the anisotropic calibration procedure across both numerical schemes and hydrodynamic regimes. In all tested cases, optimal performance is observed for moderate anisotropy ratios, typically within the range $2.5 \leq D_L/D_T \leq 3.5$. Notably, the most accurate calibrations, obtained using the flux-limited scheme, consistently yield an optimal ratio of $D_L/D_T = 3.5$ for both configurations **C0** and **C1**.

Concerning the second objective, the use of time-averaged hydrodynamics appears to be a valid approximation for configuration **C0**, whose dynamics are inherently steady. In contrast, configuration **C1**, which features temporal variability, cannot be accurately reproduced with steady hydrodynamic. The absence of transient structures results in artificial pollutant accumulation and overestimated concentrations, highlighting the role of time-dependent flow patterns in driving dispersion and lateral mixing. While increasing the transverse diffusion coefficient D_T can partially offset the lack of recirculation by enhancing cross-flow spreading, such tuning effectively introduces artificial diffusion to compensate for missing physical processes. This strategy may reduce certain errors but lacks a strong physical foundation. Therefore, for realistic representation of pollutant dynamics in configuration **C1**, the use of fully unsteady hydrodynamic fields is not only preferable but essential.

7.4 Hydrodynamic Validation

This section aims to validate the hydrodynamic inputs used in the pollutant transport simulations, distinguishing between two types of representations: steady (time-averaged) and unsteady. Given the high computational cost associated with reading and processing large hydrodynamic datasets from the Wolf 2D model, simplified strategies were adopted to reduce simulation time. These strategies must be justified to ensure they do not compromise the accuracy of the results.

7.4.1 Time-averaged Hydrodynamic

In all pollutant transport simulations performed under steady-flow conditions, a short-duration hydrodynamic simulation was systematically used to generate a time-averaged velocity field, which was then applied over a much longer transport period. This approach significantly reduces computational cost by avoiding the need to process long-duration hydrodynamic outputs. However, it implicitly assumes that the flow stabilizes rapidly and that a short time window is sufficient to capture the essential structures of the steady-state regime. The purpose of this section is to validate this assumption by comparing the results of two transport simulations, both lasting 100 [s], driven respectively by a 10 [s] and a 100 [s] time-averaged velocity field. This comparison allows us to assess whether the short averaging window provides a reliable representation of the hydrodynamics for longer transport simulations.

These simulations are performed using an isotropic diffusion configuration, with constant and equal diffusion coefficients in both directions. This setup provides a neutral reference case, ensuring that the results are not influenced by directional bias in the diffusion tensor.

As shown in Table 7.2, the resulting pollutant distributions and outlet discharges are nearly identical. This confirms that the hydrodynamic field stabilizes rapidly and that averaging over a short 10 [s] simulation is sufficient to represent steady-state flow for longer transport simulations. This approach offers a reduction in computational cost without compromising accuracy.

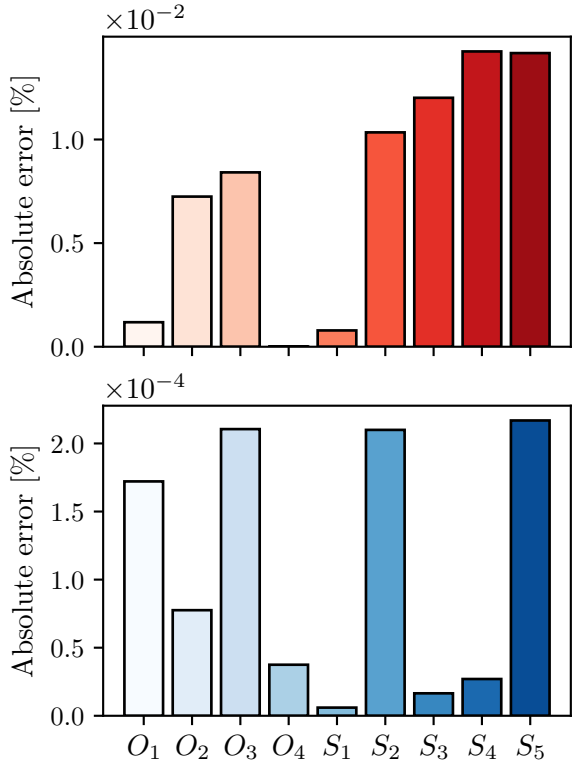

Figure 7.15: Absolute error between 10 [s] and 100 [s] averaged simulations, for both pollutant mass (red plot) and water discharges (blue plot).

Pollutant [%]	**10 [s]**	**100 [s]**
$Q_{out,1}$	37.99	37.99
$Q_{out,2}$	41.48	41.49
$Q_{out,3}$	20.52	20.51
$Q_{out,4}$	0.01	0.01
$Q_{S,1}$	100.24	100.24
$Q_{S,2}$	92.55	92.56
$Q_{S,3}$	54.62	54.63
$Q_{S,4}$	7.62	7.61
$Q_{S,5}$	7.57	7.55
Water [%]		
$Q_{out,1}$	29.42	29.42
$Q_{out,2}$	24.33	24.33
$Q_{out,3}$	23.96	23.96
$Q_{out,4}$	22.29	22.29
$Q_{S,1}$	69.23	69.23
$Q_{S,2}$	62.18	62.18
$Q_{S,3}$	32.76	32.76
$Q_{S,4}$	7.05	7.05
$Q_{S,5}$	15.53	15.53

Table 7.2: Comparison of pollutant and water discharges [%] at each outlet and section using 10 [s] and 100 [s] averaged hydrodynamics.

The comparison of pollutant and water discharges between the two hydrodynamic inputs is further illustrated in Figure 7.15, which presents the absolute error between the 10 [s] and 100 [s] averaged cases at each outlet and internal section. The observed differences are systematically below 2.5×10^{-4} [%] for water discharges and remain under 1.3×10^{-2} [%] for pollutant mass discharges. Therefore, the 10 [s] time-averaged hydrodynamic field can be considered as a valid approximation of the full 100 [s] simulation, offering a reduction in computational time while preserving the accuracy of the resulting pollutant transport predictions.

Overall, this analysis validates the strategy of using a short 10 [s] time-averaged hydrodynamic simulation to drive longer pollutant transport simulations in steady-state configurations. Despite the reduced duration, the averaged velocity field captures all essential flow structure. This result justifies the approach adopted throughout this work. The ability to simulate long-term transport using minimal hydrodynamic input represents an advantage in the context of large-scale scenario testing and parameter calibration.

7.4.2 Unsteady Hydrodynamic

In all pollutant transport simulations performed under unsteady flow conditions, the hydrodynamic forcing was reconstructed by repeating a periodic sequence of 77 frames extracted from a 40.2 [s] Wolf 2D simulation, as presented in Section 5.6.2. This strategy was adopted to reduce computational costs. However, this approach relies on the assumption that the extracted sequence captures the essential temporal dynamics of the flow and remains representative when extended over longer durations. The objective of this section is to validate this as-

sumption by comparing the reconstructed velocity signal, obtained by repeating the 77-frames segment, with a longer 100 [s] reference signal. This analysis allows us to assess the robustness of the periodic approximation and justify its systematic use in the unsteady transport simulations.

To this end, the same peak-based period identification and frame selection methodology is applied to a longer velocity signal of 100 [s], recorded at the same sampling frequency (10 [Hz]) at the observation point defined for configuration **C1**. The reconstructed velocity signal is obtained by repeating the 77-frames segment initially selected in Section 5.6.2, and compared to the full 100 [s] reference signal.

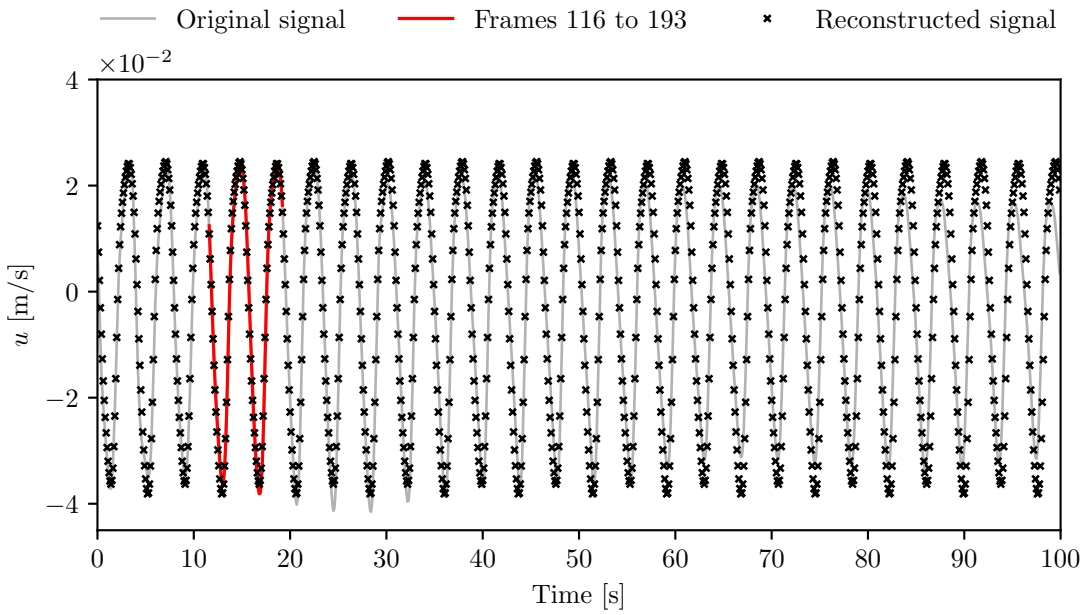

Figure 7.16: Comparison between the original velocity signal (grey line) and the reconstructed signal obtained by repeating the 77-frame sequence extracted from the 40.2 [s] simulation (black crosses). The reconstruction over 100 [s] yields a relative RMSE of 6.91 [%], confirming the validity of the periodic approximation.

Figure 7.16 shows the comparison between the original velocity signal and its reconstruction using the repeated-frame approach. The reconstructed signal successfully captures the global periodic behaviour of the original flow. The relative root-mean-square error (RMSE) between the two signals is 6.91 [%], which confirms that the 77-frame sequence extracted from the 40.2 [s] dataset remains representative when extended over a longer simulation window. Although the error remains below 10 [%], and thus acceptable for practical purposes, it must still be taken into account when interpreting the results of the simulations based on this reconstruction. In particular, small-scale temporal fluctuations that are not captured by the repeated-frame method may slightly influence pollutant transport and mixing dynamics in sensitive configurations.

In addition, repeating the period detection algorithm on the full 100 [s] signal yields the same dominant period of $T_{\text{best}} = 7.70\,[\text{s}]$, confirming the temporal consistency of the hydro-

dynamic oscillations. Although the exact frame sequence minimizing the reconstruction error differs slightly, owing to variations in signal shape over time, the persistence of the dominant frequency validates the use of a fixed frame count for time extrapolation.

Ideally, this validation procedure should be applied to the full 3000 [s] hydrodynamic simulation to ensure that the selected periodic segment remains representative over the entire duration. Such an analysis would allow for a more accurate quantification of long-term deviations and offer a stronger justification of the frame-repetition strategy. However, a major bottleneck lies in the reading and processing of the Wolf 2D hydrodynamic outputs. In the current setup, each hydrodynamic frame takes approximately 1 minute and 30 seconds to load, due to the size and structure of the simulation data. Extending this procedure to the full 3000 [s] simulation at a temporal resolution of 0.1 [s] would involve over 30 000 frames, resulting in long preprocessing times.

A possible alternative would be to re-run the Wolf 2D simulation with a reduced output frequency, thereby limiting the number of exported frames. However, this would inevitably degrade the temporal resolution of the reconstructed velocity field and reduce the accuracy of pollutant transport simulations, particularly in configurations where transient flow features play a role. Given these constraints, the 100 [s] test used here offers a good compromise: it captures several oscillation cycles while keeping data processing and simulation time manageable. While it does not cover the entire simulation period, it is sufficient to validate the use of repeated velocity frames within the current modelling approach.

These results confirm that the periodic approximation based on the selected 77 frames remains valid for extended time windows, at least over the tested 100 [s] duration. This supports the use of a frame-repetition strategy in the advection-diffusion simulations, as it provides a reliable yet computationally efficient way to represent unsteady hydrodynamic forcing without requiring the full resolution of long-duration flow simulations.

Chapter 8

Conclusions and Perspectives

8.1 Conclusions

This thesis has explored the modelling of pollutant transport in flooded urban environments through the development and validation of a two-dimensional advection-diffusion solver. The numerical framework was implemented in Python, with a modular structure allowing for anisotropic diffusion, multiple advection schemes, and both steady and unsteady hydrodynamic forcing.

The first part of this study focused on evaluating the impact of numerical discretization on the accuracy and stability of pollutant transport simulations. Several advection schemes were implemented and tested on synthetic benchmark cases, including the first-order upwind scheme and a second-order limited scheme based on Total Variation Diminishing (TVD) flux limiters. The results showed that the first-order upwind scheme provides a robust and stable solution with low computational cost, but introduces significant numerical diffusion that tends to smear sharp concentration fronts. In contrast, the second-order limited scheme, incorporating limiters such as Minmod, substantially improves the accuracy of the concentration profiles by reducing numerical diffusion, but requires more computational resources due to its increased complexity. This trade-off between computational efficiency and numerical accuracy highlights the importance of selecting an appropriate discretization strategy depending on the objectives and constraints of the simulation.

The impact of anisotropic diffusion was then analysed in detail. By varying the longitudinal and transverse components of the diffusion tensor, it was shown that introducing anisotropy significantly improves the representation of pollutant dispersion in elongated and directionally constrained urban geometries. A parametric study revealed that an optimal ratio between longitudinal and transverse diffusivities enhances agreement with experimental observations, reflecting the directional bias of transport mechanisms in such environments.

A third focus was placed on hydrodynamic variability. The comparison between steady (time-averaged) and unsteady flow conditions revealed that configuration **C0**, characterized by quasi-steady dynamics, can be reasonably approximated using a time-averaged velocity field. In contrast, configuration **C1** exhibited strong temporal fluctuations, making unsteady hydrodynamics essential for accurate pollutant transport modelling. Simplified frame-repetition strategies were proposed and validated to represent unsteady forcing at reduced computational cost.

Finally, simulation results were compared to experimental data collected on the M.U.R.I. platform developed by INRAE. The numerical model successfully reproduced several key patterns observed in the laboratory, including preferential pathways and pollutant accumulation near stagnation zones. However, discrepancies remained in certain cases, suggesting that further refinement of the diffusion calibration and hydrodynamic representation is needed.

Overall, the modelling approach presented in this work provides a flexible and efficient tool to simulate pollutant transport under realistic flood conditions. This framework lays the groundwork for future studies aiming to improve urban water quality predictions under extreme weather scenarios.

8.2 Perspectives

While the present work offers a solid foundation for modelling pollutant transport in flooded urban environments, several directions remain open for future exploration and improvement.

A first direction concerns the optimization of the numerical solver. Despite its robustness and modularity, the current implementation suffers from high computational costs, particularly in configurations involving time-resolved hydrodynamics or flux-limited advection schemes. These limitations have constrained the number of simulations that could be carried out, especially in the context of large parametric sweeps. Improving code performance, through more efficient memory management, would reduce computation times and enable broader sensitivity analyses across a wider range of model parameters.

Secondly, the analysis conducted in this study focused primarily on a single urban block and injection point. However, experimental data are available for several other configurations, involving different street layouts and injection locations. Extending the simulations to these additional scenarios would make it possible to assess the generalizability of the conclusions, particularly regarding the role of anisotropic diffusion. Such validation across multiple flow patterns and transport paths would strengthen the confidence in the identified diffusion parameters and help determine whether the same anisotropic ratios remain valid beyond the current case study.

In addition, while an initial calibration of the longitudinal and transverse diffusion coefficients was carried out, this approach remained limited to a predefined and discretized set of values due to computational constraints. Consequently, the resolution of the parameter space may not have been sufficient to fully capture the optimal anisotropic ratio. To overcome this limitation, more advanced optimization techniques could be considered. Gradient-based methods offer a systematic way to converge toward local minima of the error metric, while heuristic approaches such as genetic algorithms allow for global exploration of the parameter space without requiring gradient information. Integrating such optimization algorithms into the calibration framework could enhance the accuracy and efficiency of the identification process for the diffusion tensor parameters.

Beyond the explicit calibration of longitudinal and transverse diffusivities, alternative approaches exist for representing the diffusion tensor in a more general and potentially scalable manner. As reviewed in Mignot et al. [2023], several studies have proposed to express anisotropic diffusion through dimensionless relationships, notably using the Schmidt number or empirical formulations such as the one introduced by Elder. These approaches define

the diffusion coefficients as functions of local flow variables (*e.g.*, velocity, depth), offering the advantage of adapting the tensor to varying hydrodynamic conditions without the need for manual calibration in each configuration. Such parameterizations may enhance the transferability of the model to different spatial scales or flow regimes, and could provide a more unified theoretical framework. Implementing and testing these tensor representations in the present simulation framework would constitute a promising direction to improve both physical consistency and predictive capabilities across a wider range of scenarios.

Another important perspective lies in the dimensionality of the model. The present work relies on a depth-averaged two-dimensional formulation, which neglects vertical variability in both velocity and concentration. While such simplification offers computational advantages, it may fail to capture essential transport mechanisms. Extending the model to a fully three-dimensional framework would allow for a more complete representation of physical processes, particularly in complex urban topographies where vertical gradients are non-negligible. In parallel, validating the numerical predictions against real-world datasets, beyond laboratory-scale experiments, would be interesting to assess the model predictive capacity under field conditions. This would require access to measurements of flow and pollutant concentrations in real flood scenarios.

Finally, the present work relied exclusively on an explicit Euler time integration scheme due to its simplicity and ease of implementation. Nonetheless, more advanced time discretization methods such as Runge-Kutta schemes offer potential advantages in terms of stability and accuracy, particularly when dealing with stiff problems or variable flow regimes. Unfortunately, these schemes could not be tested within the timeframe of this study due to their higher computational demands. Investigating the impact of alternative time integration methods represents a valuable next step to further enhance the robustness and efficiency of the solver.

Overall, these perspectives point toward a broader and deeper exploration of pollutant transport modelling in complex hydrodynamic settings. By addressing the current computational limitations and expanding the range of tested configurations and numerical methods, future studies can consolidate the reliability of the proposed approach and extend its applicability to real-world risk management scenarios.

Nomenclature

Acronyms

CFL	Courant–Friedrichs–Lewy Condition
Co	Courant Number
FEM	Finite Element Method
FVM	Finite Volume Method
INRAE	Institut National de Recherche pour l'Agriculture, l'Alimentation et l'Environnement
M.U.R.I.	Maquette Urbaine Réaliste à l'échelle Inondation
NSE	Nash–Sutcliffe Efficiency coefficient
Pe	Péclet Number
RMSE	Root Mean Square Error
SWE	Shallow Water Equations
TVD	Total Variation Diminishing

Physical quantities

h	Water depth	m
C	Depth-averaged pollutant concentration	$\mathrm{kg\,m^{-3}}$
$\mathbf{U}$	Velocity vector (U, V)	$\mathrm{m\,s^{-1}}$
U, V	Depth-averaged velocities in x and y	$\mathrm{m\,s^{-1}}$
$\mathbf{D}$	Diffusion tensor	$\mathrm{m^2\,s^{-1}}$
D_{xx}, D_{yy}	Main diagonal components of $\mathbf{D}$	$\mathrm{m^2\,s^{-1}}$
D_{xy}, D_{yx}	Cross-diffusion components	$\mathrm{m^2\,s^{-1}}$
D_L	Longitudinal diffusion coefficient	$\mathrm{m^2\,s^{-1}}$
D_T	Transverse diffusion coefficient	$\mathrm{m^2\,s^{-1}}$
$\Delta x, \Delta y$	Grid resolution in y and x	m
Δt	Time step	s

T	Total simulation time	s
$Q_{\text{injection}}$	Injection flow rate	$\mathrm{L\,h^{-1}}$
$C_{\text{injection}}$	Pollutant injection concentration	$\mathrm{g\,L^{-1}}$
C_m	Ideal mixed concentration	$\mathrm{kg\,m^{-3}}$
$\langle C_s \rangle$	Spatially averaged concentration in the urban block at the end of the simulation	$\mathrm{kg\,m^{-3}}$
$\langle C(t) \rangle$	Time-averaged concentration	$\mathrm{kg\,m^{-3}}$
$C_{\text{mix, outlet}}$	Mean outlet concentration	$\mathrm{kg\,m^{-3}}$
i, j	Spatial indices (grid cells in y, x)	
n	Time step index	
θ	Flow direction	rad
S	Source term in advection-diffusion	$\mathrm{kg\,m^{-3}\,s^{-1}}$
$\mathbf{A}$	Sparse matrix of the linear system	
$\mathbf{b}$	Source vector	
C^n	Pollutant concentration at time step n	
$F_{i,j}, G_{i,j}$	Numerical fluxes in x and y directions	
q_x, q_y	Discharges in x and y directions	$\mathrm{m^2\,s^{-1}}$
$u_{\max}$	Maximum flow velocity	$\mathrm{m\,s^{-1}}$

List of Figures

List of Tables

Bibliography

Alavian, V. (1986). *Dispersion Tensor in Rotating Flows*. Journal of Hydraulic Engineering, 112(8): 771-777.

Brajkovic, J., Fettweis, X., Noël, B., Ghilain, N., Archambeau, P., Pirotton, M., & Doutreloup, S. (2025). *Increased intensity and frequency of extreme precipitation events in Belgium as simulated by the regional climate model MAR*. Journal of Hydrology: Regional Studies, 59, 102399.

Camnasio, E., Erpicum, S., Archambeau, P., Pirotton, M., Dewals, B. (2014). *Prediction of mean and turbulent kinetic energy in rectangular shallow reservoirs*. Engineering Applications of Computational Fluid Mechanics.

CFD Direct. (2025). *3.11 Limited advection schemes – CFD General Principles*. `https://doc.cfd.direct/notes/cfd-general-principles/upwind-scheme`.

Cheng, N. S. (1984). *Modeling of Anisotropic Diffusion in Open Channel Flows*. Journal of Hydraulic Research.

Courant, R., Friedrichs, K., Lewy, H. (1928). *Über die partiellen Differenzengleichungen der mathematischen Physik*. Mathematische Annalen.

Dekenne, A., Dendoncker, N., Dewals, B., et al. (2022). *Rapport d'analyse sur les inondations de juillet 2021 en Wallonie*. SPW Mobilité et Infrastructures. `https://www.wallonie.be/fr/actualites/inondations-rapport-2022`

Dewals, B. J., Erpicum, S., Archambeau, P., Detrembleur, S., Pirotton, M. (2006). *Numerical tools for dam break risk assessment: validation and application to a large complex of dams*. University of Liège.

Dewals, B. et al. (2023). *Can the 2D shallow water equations model flow intrusion into buildings during urban floods?*. Journal of Hydrology.

Elder, J. W. (1958). *The dispersion of marked fluid in turbulent shear flow*. Cavendish Laboratory, University of Cambridge. Journal of Fluid Mechanics, vol. 5, p.544-560.

Erpicum, S., Meile, T., Dewals, B. J., Pirotton, M., Schleiss, A. J. (2009). *2D numerical flow modeling in a macro-rough channel*. International Journal for Numerical Methods in Fluids.

Fagour, C. (2024). *A laboratory experiment on the pollutant transport in a flooded streand network*. Journal of Hydrology.

Fagour, C. (2025). *Pollutions causées par les inondations urbaines : Modélisation expérimentale du transport de polluants issus de déversements locaux*. Thèse de doctorat, INSA Lyon.

Fang, S., Ji, Y., Zhang, M. (2022). *Numerical Modeling the Flood and Pollutant Transport Processes in Residential Areas with Different Land Use Types*. Advances in Meteorology.

Ferziger, J. H., Perić, M. (2002). *Computational Methods for Fluid Dynamics*. 3rd edition, Springer.

Fischer, H. B. (1973). *Longitudinal dispersion and turbulent mixing in open-channel flow*. University of California, Berkeley.

Fischer, H. B. et al. (1979). *Mixing in Inland and Coastal Waters*. Academic Press.

Fontaine, G. (2023). *Comment simuler une dispersion de pollution lors d'une inondation urbaine avec un code numérique opérationnel 2D*. Rapport de stage PFE, INRAE.

Hirsch, C. (2007). *Numerical Computation of Internal and External Flows, Volume 1*. 2nd edition, Elsevier.

IPCC (2021). *Climate Change 2021: The Physical Science Basis*. Cambridge University Press. https://www.ipcc.ch/report/ar6/wg1

Institut Royal Météorologique de Belgique (IRM). (2022). *Évolution du nombre de jours de fortes précipitations à Uccle entre 1892 et 2022*. https://climat.be/en-belgique/climat-et-emissions/changements-observes

Kalinski, M. (2018). *Divergence (Gauss–Ostrogradsky) theorem*. ResearchGate. https://www.researchgate.net/publication/327971432

Kim, B., Seo, I. W., Kwon, S., Baek, D. (2023). *Estimating Nand Retention Time of Solute in Storage Zones of a Stream*. Water Resources Research.

Lam, S. K., Pitrou, A., Seibert, S. (2015). *Numba: A LLVM-based Python JIT Compiler*. ACM.

Lee, M. E., Kim, G. (2012). *Influence of Secondary Currents on Solute Dispersion in Curved Open Channels*. Journal of Applied Mathematics.

Lee, J., Kim, S. (2012). *Cross-Dispersion Effects in Shallow Water Mixing*. Journal of Hydraulic Engineering.

Lee, M. E., & Seo, I. W. (2007). *Analysis of pollutant transport in the Han River with tidal current using a 2D finite element model*. Journal of Hydro-Environment Research.

Le Coz, J., Jodeau, M., Hauet, A., Marchand, B., Le Boursicaud, R. (2014). *Image-based velocity and discharge measurements in field and laboratory studies using optical flow methods*. River Flow. https://hal.inrae.fr/hal-02600735.

LeVeque, R. J. (2002). *Finite Volume Methods for Hyperbolic Problems*. Cambridge University Press.

Liu, X. (2019). *A robust numerical model for shallow water governing solute transport with wet/dry interfaces*. Journal of Hydrodynamics.

Université de Liège. (2021). *Cours de Mathématiques Appliquées*. Département d'Ingénierie Mathématique.

Mejía-Morales, M. A. et al. (2020). *Turbulence modeling in shallow water equations*. Water Resources Research.

Mejía-Morales, M. A., Mignot, E., Paquier, A., Proust, S. (2023). *Effect of Storage Capacity of a City Block on Urban Flood Flows*. Water Resources Research.

Mignot, E., Riviere, N., Dewals, B. (2023). *Formulations and Diffusivity Coefficients of 2D Depth-Averaged Advection-Diffusion Models: A Literature Review*. Water Resources Research.

Morales-Hernández, M., Murillo, J., García-Navarro, P. (2019). *Diffusion–dispersion numerical discretization for solute transport in 2D transient shallow flows*. Environmental Fluid Mechanics.

Nakayama, Y. (2018). *Introduction to Fluid Mechanics*. Second Edition, Elsevier.

Newsweek (2024). *Flash Floods Leave Scores Dead in Spain as Rescue Efforts Intensify*. https://www.newsweek.com/flash-floods-spain-valencia-dead-rescue-efforts-intensify-1977094

Paszke, A., Gross, S., Massa, F., et al. (2019). *PyTorch: An Imperative Style, High-Performance Deep Learning Library*. NeurIPS, 32.

Pathirana, A., Gersonius, B., Zevenbergen, C. (2011). *Modeling of contaminant transport during an urban pluvial flood event*. 12th International Conference on Urban Drainage. Porto Alegre, Brazil.

Permetrics Project. *Nash–Sutcliffe Efficiency — Permetrics v2.0.0 documentation*. https://permetrics.readthedocs.io/en/v2.0.0/pages/regression/NSE.html

Python Software Foundation. (2022). *Python 3.10 Documentation*. https://docs.python.org/3.10/

Riflet, G. (2023). *1D Numerical Methods With Finite Volumes*. MARETEC IST.

Shin, J., Seo, I. W., Baek, D. (2020). *Longitudinal and transverse dispersion coefficients of 2D contaminant transport model for mixing analysis in open channels*. Journal of Hydrology.

Stevens, J. R., et al. (2010). *Pollutant mobilisation by urban flood events: a literature review*. Urban Water Journal, **7**(3), 145-160.

Strang, G. (1993). *Introduction to Linear Algebra*. 3rd ed., Wellesley–Cambridge Press.

Strikwerda, J. C. (2004). *Finite Difference Schemes and Partial Differential Equations*. 2nd edition, SIAM.

van Es, B., Koren, B., & de Blank, H. J. (2022). *Finite-Difference Schemes for Anisotropic Diffusion*. CWI Technical Report. https://ir.cwi.nl/pub/31709

Velickovic, M., Zech, Y., Soares-Frazão, S. (2017). *Steady-flow experiments in urban areas and anisotropic porosity model*. Journal of Hydraulic Research.

Welch, P. D. (1967). *The use of Fast Fourier Transform for the estimation of power spectra*. IEEE Trans. on Audio and Electroacoustics.

Wolf, University of Liège. (2024). *WOLF2D: Python-based hydrodynamic modeling tool*. https://wolf.hece.uliege.be